STUDYING CHIRALITY, CONFORMATIONAL FLEXIBILITY, AND INTERMOLECULAR INTERACTIONS WITH CHIROPTICAL SPECTROSCOPY

By

Andrew Ricardo Puente

Dissertation

Submitted to the Faculty of the

Graduate School of Vanderbilt University

in partial fulfillment of the requirements

for the degree of

DOCTOR OF PHILOSOPHY

in

Chemistry

May 10, 2024

Nashville, Tennessee

Approved:

Prasad L. Polavarapu, Ph.D.

Lauren E. Buchanan, Ph.D.

Michael P. Stone, Ph.D.

Kálmán Varga, Ph.D.

For my friends, family, and all of my students.

ACKNOWLEDGMENTS

I would like to express my thanks to my advisor, Prof. Prasad Polavarapu, who has fully supported me throughout my Ph.D. He is always full of ideas, and eager to listen to mine. I can always count on his advice when I am stuck on a project and do not know how to proceed. I especially appreciate his gentle reminders of the bigger picture, as I too often tend to lose the forest for the trees. I am grateful for the tremendous resources left behind by past members of the Polavarapu Lab, especially Jordan Johnson for his great advice and insight as well as Cody Covington for his many, many, many scripts that have automated the vast amount of calculations and analyses throughout my Ph.D. work.

Many thanks to my committee: Prof. Lauren Buchanan, Prof. Michael Stone, and Prof. Kálmán Varga. I have thoroughly enjoyed my Quantum Chemistry and Spectroscopy classes with Profs. Buchanan and Stone. I am grateful for the immense expertise provided by each member of my committee and their guidance throughout my Ph.D. I am also appreciative of the Stone Lab for letting me use their ECD spectrometer, and want to express my thanks to Dr. Rochana Tomar for patiently teaching me how to use this incredible instrument.

I also want to thank the many friends I have made in the Chemistry Department. Ruben Torres, Sebastian Flores, Laurel Bellochio, and Oleg Kovtun in the Rosenthal lab have accompanied me on many journeys for coffee and lunch in the Med Café. In my cohort, Ruben, Lauren Wenger, Lexie Koziel, and Grace Buckey have been close friends who were part of my bubble during the pandemic. Dr. Ross Koby has also been a great ally in tackling computational chemistry problems.

Last, but certainly not least, I would also like to thank the many computers in my office for running numerous calculations over the years. Several comrades have fallen over the years (R.I.P. pchem nodes 3, 4, 6, 8, and 9) and I will always remember them. I am also additionally grateful for Cody Covington for his advice on making this computational chemistry cluster possible.

This work was also conducted in part using the resources of the Advanced Computing Center for Research and Education (ACCRE) at Vanderbilt University, Nashville, TN.

TABLE OF CONTENTS

Page

LIST OF TABLES

LIST OF FIGURES

CHAPTER 1

Introduction

1.1 Chirality

Chirality—or, the existence of non-superimposable mirror-images—is a fundamental property of nature. Everything from small molecules, biomolecules, to the shoes on your feet can possess this property. In chemistry, mirror-image molecules that are non-superimposable are called enantiomers. Enantiomers possess identical chemical and physical properties, except when in a chiral environment. Since our bodies possess proteins, nucleic acids, and carbohydrates, all of which can be chiral, it is of the upmost interest of medicinal chemists to fully characterize the chirality of drugs. In fact, the FDA requires that the full three-dimensional structure, or Absolute Configuration (AC) is known exactly before any drug can be brought to market.

AC determination is not a simple task. Common methods such as Nuclear Magnetic Resonance (NMR) spectroscopy are capabale of probing the three-dimensional structure but cannot differentiate between pairs of enantiomers, since NMR is an achiral spectroscopy, without the use of chiral solvating or derivatizing agents.[1,2] The gold-standard in AC determination is X-ray crystallography which requires obtaining well-diffracting single crystals of the chiral compound, which is easier said than done. This is especially true of natural products which tend to be complex, oily molecules with high conformational mobility.

1.2 Optical Rotatory Dispersion

Optical Rotation (OR) is the ability of a molecule to rotate plane-polarized light clockwise or anticlockwise as it passes through a medium. Plane-polarized light consists of equal parts left- and right-circularly polarized light. In chiral media, these left- and right-circularly polarized components each have slightly different refractive indices, ε_L and ε_R, causing the circularly polarized components to fall out of sync, thus causing the plane of

polarization to rotate without causing the overall polarization state to change. Enantiomers exhibit opposite signs of OR and are either dextrorotatory (rotates plane of polarization clockwise) or levorotatory (rotates the plane of polarization counterclockwise). The convention in organic chemistry is to label enantiomers based on the sign of OR at the Sodium D-line, which is roughly 589 nm, as either (+) or (–).

OR is one of the earliest chiroptical spectroscopic techniques, and one of the easiest to measure. However, OR carries very little stereochemical information relative to other chiroptical techniques, with only one OR value per wavelength. Additionally, OR is a difficult property to compute due to (1) near cancellation of diagonal elements in the electric-dipole–magnetic-dipole polarizability tensor, and (2) near cancellation of Boltzmann-weighted contributions from conformers in the molecular ensemble. In certain solvents, the magnitude of OR or even the sign of OR can change based on solvent polarity, an effect that is difficult to computationally model accurately.[3] As a result, OR calculations tend to be off by an order of magnitude, or worse, and sometimes fail to reproduce the sign of OR. These downsides lend OR to be useful as a supplemental technique, rather than as one that can assign the AC of chiral molecules on its own. However, OR remains the *de facto* label for stereoisomerism due to the ease at which experimental data can be obtained for pure enantiomers or mixtures with enantiomeric excess (ee).

Certain compounds do not rotate plane-polarized light, despite being chiral, as the electronic properties of the molecule lead to a non-measurable OR. Sometimes these molecules are classified as ”cryptochiral” (which is a misnomer as the compounds are without a doubt chiral) or more properly, crypto-optically active. I will discuss one such compound in the next chapter.

1.3 Electronic Circular Dichroism

Circular dichroism (CD) is defined as the differential absorption of left- and right-circularly polarized light.

When multiple types of chirality are present in a molecule, ECD is typically more sensitive to higher-order chiralities. Different types of chirality can be assigned a dimensionality based on the defining stereogenic unit or axis. The most common form of chirality, point chirality about an asymmetric carbon or other tetrahedral center, is a zero-dimensional chirality. Axial and helical chiralities are one-dimensional, and planar chirality is two-dimensional. Three-dimensional chiralities or topological chiralities are chiral due to the overall three-dimensional spatial orientation, instead of a definable stereogenic unit. As an example, the ECD spectrum of cephalochromin, which possesses both axial and point chiralities, is dominated by its axial chirality.[4] This can be beneficial in assigning the AC when a higher-order chirality is unknown, but can be disadvantageous when the lower-order chiralities are unknown.

In practice, an ECD spectrum usually has two to three strong chiroptical signals. This limited information can make AC assignments by ECD quite difficult as calculations must reproduce these spectral features with great confidence.

1.4 Vibrational Circular Dichroism

Vibrational transitions can also exhibit differential absorption of left- and right-circularly polarized light in a phenomenon known as VCD. Since each vibrational transition can give differential absorption, the VCD spectrum is rich with chiroptical signals. Unlike ECD, there are no empirical rules that can be used to interpret VCD spectra. Thus, *ab initio* investigations must be carried out in detail to reliably interpret VCD spectra, especially for AC determination.

While experimental measurements of VCD are reliably obtained down to 800 cm^{-1},[5] this requires the use of IR-transparent solvents such as DMSO-d_6, D_2O, CS_2, $CDCl_3$, etc.[6] Ideally, non-polar solvents or polar solvents that weakly hydrogen-bond would be used in VCD measurements as calculations can reliably reproduce spectral features with only an implicit solvation model. However, chiral alcohols and carboxylic acids can form aggre-

gates in solution, further complicating the conformational analysis.[7–9]

1.5 Vibrational Raman Optical Activity

Just as with VCD, Raman-active vibrational modes can be probed by Vibrational Raman Optical Activity (VROA) spectroscopy. The expected Raman Optical Activity (ROA) decreases proportionally with λ^4, and so VROA is roughly 10,000 times weaker than the corresponding Raman activity. This effect limits ROA to electronic and vibrational transitions, as rotational ROA would be too weak to reliably measure. Like VCD, VROA is rich in spectral features and requires *ab initio* calculations in order to interpret VROA spectra.

There are several VROA polarization schemes depending on (a) the angle between the incident laser and the detector and (b) whether the incident light is unpolarized or polarized. VROA has some inherent experimental challenges, as the number of inelastically Raman-scattered photons is already quite low. Additionally, the differential scattering of left- and right-circularly photons is an even weaker effect ($\sim 10^{-3}$–10^{-4}) than Raman itself, leading to long collection times.[10] This makes VROA especially susceptible to experimental artifacts and instrumental noise.[10] A common wavelength used in VROA measurements is 532 nm, however for biological applications this laser wavelength is not ideal owing to interference from absorption of the incident light. Thus, longer wavelengths must be used which further lower the VROA effect.

VROA has the distinct advantage of being able to study molecules in H_2O, as this solvent is not very Raman-active, lending itself as a useful technique to study biomolecules in their natural state. VROA is state-of-the-art for studying saccharide conformational mobility and ring puckering due to its sensitivity to chirality and conformational flexibility.[11,12] This allows probing of the glycosidic linkage in the fingerprint region[13,14] and in the C–H region.[15]

1.6 Quantum Chemistry

For the chiroptical properties I discuss herein, it is important to obtain Boltzmann-averaged properties that can be compared to experiment. In principle, this requires obtaining a complete representation of the molecule ensemble and the chiroptical properties of each conformer. This is typically accomplished via an initial systematic conformational search at the molecular mechanics level, and then successive optimizations at the Density Functional Theory (DFT) level. In practice, sampling conformational space can quickly become expensive in the case of very flexible molecules, and exceptionally difficult when solute–solvent clusters or molecular aggregates must be considered.

At the DFT level, there is a zoo of DFT functionals that can be chosen. In this work I will focus primarily on organic molecules (containing H,C,N,O) which have several popular functionals. B3LYP and B3PW91 have been shown to perform very well for the computation of vibrational modes of organic molecules. For time-dependent DFT (TD-DFT), which are necessary for calculations of ECD bands, the CAM-B3LYP and ωB97X-D functionals have been shown to perform well. For molecules containing C–F bonds, the M06-2X functional performs well for the prediction of the intense C–F stretching vibration and associated VCD bands.[16]

One of the drawbacks of DFT methods is that they neglect the treatment of long-range London dispersion interactions. To resolve this, Grimme has proposed several methods for the correction of both short-range (which is partially treated in DFT) and long-range dispersion (which is neglected). The inclusion of empirical dispersion can have drastic effects on the conformational ensemble, and are necessary for reproducing a wide range of properties such as π–π stacking interactions and the bent structure of heavy group 2 metallocenes.[17] In this context, I will focus on the D3[18] and D3(BJ)[19] empirical dispersion frameworks. The inclusion of empirical dispersion corrections have been shown to be necessary for the simulation of ECD in some cases,[20] but their inclusion has had mixed results for simulated VCD, often making agreement with experiment worse.[7,21–23] Systematic examinations of

the effect dispersion corrections have on simulated VROA have not been reported. Several DFT functionals already have empirical dispersion corrections baked into the molecular model, such as the popular ωB97X-D functional which has Grimme's D2 dipersion corrections.

1.7 Research Motivation

As I have discussed above, chiroptical spectroscopies are an excellent way to probe the three-dimensional structure of chiral molecules. In the case of exotic chiralities, especially those concerning isotopic substitution, they are effective AC determination methods. In this work, I will demonstrate two such cases whereby I probe such chiralities with VCD. In Chapter 2, I will demonstrate the applicability of AC determination for an isotopically chiral ethyl tosylate. Because this compound is only chiral due to deuterium substitution, conventional X-ray crystallographic methods would be unable to determine the AC. In Chapter 3, I will determine the AC of a mechanically planar chiral compound via VCD and ECD spectroscopy. While the applicability of VCD has been previously demonstrated for model [2]rotaxane compounds with mechanical chirality, this demonstrates the first AC determination of a mechanically chiral compound.

The sensitivity of VCD and VROA to subtle conformational changes makes them excellent tools in delving into the conformational ensemble and locating low-energy conformers of chiral molecules. Computing the chiroptical properties of rigid molecules is easy, but conformationally flexible molecules pose several additional challenges. Flexible molecules can have a substantial number of conformers, leading to high computational costs associated with even low-level DFT investigations into the conformational ensemble. Conformational searches can result in tens of thousands of conformers and typical strategies can miss low-energy conformers. This severely limits the applicability of VCD and VROA as key spectral features may fail to be reproduced by calculations if the appropriate conformers are missing. I will discuss three such cases whereby I attempt to wrangle flexible molecules. In

Chapter 3, I will discuss a molecule with mechanical chirality where the relative orientation of an axle and macrocycle introduces a high-dimensional chirality into the system. Systematic searches are unable to avoid the problem of maintaining this stereochemical property, as a search will return a ensemble containing conformers with mechanical chirality (which is desired) and unbound conformers that do not possess mechanical chirality (which is not desired). In Chapter 4, I will discuss two linear diarylheptanoids that are dehydrogenated derivatives of curcumin. Their conformational flexibility leads to frustratingly weak ECD and VCD spectra, pushing the limits of correlation between experiment and simulation. In Chapter 5, I will discuss a natural product composed of a large, but rigid, diterpene unit and a highly mobile saccharide unit. Thankfully, sterics lock the saccharide ring into one low-energy chair conformation which leads to only a few low-energy conformers. However, locating these conformations was no easy task due to both the number of conformers in the initial ensemble and the large size of the molecule. Thus, strategies must be applied to tweeze out these desired conformations and reliably model this compound.

In addition to conformational flexibility, VCD and VROA are particularly sensitive to the intermolecular interactions formed between chiral molecules and the solvent environment or, in the case of alcohols and carboxylic acids, the formation of homochiral dimers. In hydrogen-bonding solvents, the attractive interactions between solute and solvent tend to be long-lived and thus influence the solute's spectroscopic properties.[24] In Chapter 6 I will explore the modeling of solvation effects in dimethyl sulfoxide (DMSO) solvent. I will approach this problem through the microsolvation approach, whereby solvent molecules are explicitly considered at sites where hydrogen-bonding is the strongest. This has the advantage of being computationally tractable in the treatment of solvation effects at the DFT level, but does not solve the issue of sampling solute–solvent conformational space. To tackle this issue, I utilize enhanced sampling molecular dynamics methods in order to locate low-energy solute–solvent clusters. In Chapter 7 I will also explore the formation of dimers for very flexible ladderanoic acids via a similar approach.

As a last hurrah, in Chapter 8 I will computationally explore the potential of a new (but theoretically old) chiroptical spectroscopy known as Rayleigh Optical Activity, the Rayleigh scattering counterpart to ROA. Since most of the light in ROA measurements is elastically scattered as Rayleigh photons, Rayleigh Optical Activity is a weak effect of a strong effect, rather than a weak effect of an already weak effect as with ROA spectroscopy. Rayleigh Optical Activity has been previously (computationally) shown to be relatively insensitive to the level of theory used to compute this chiroptical property. While the experimental difficulties associated with accurately and reliably measuring small differences in intense Rayleigh scattering are well outside the scope of this thesis, I will explore its relative sensitivity to other effects such as conformational flexibility and intermolecular interactions, which can limit other chiroptical approaches such as OR, ECD, VCD, and VROA.

CHAPTER 2

The AC of a Cypto-optically Active Ethyl Tosylate

The work in this chapter can be found in the *Organic Letters* article "Chemical Synthesis of [2H]-Ethyl Tosylate and Exploration of Its Crypto-optically Active Character Combining Complementary Spectroscopic Tools".[25] I contributed to the VCD analysis of the crypto-optically active compound by performing quantum chemical calculations to determine the absolute configuration.

From an application point of view, crypto-optically active entities show a strong potential as probes for enzymatic or chemical mechanism studies.[26–28] The smallest of these, the chiral methyl group, $C^1H^2H^3H$, has been widely described and used to advance knowledge of living processes. Notably, it has been very helpful for the understanding of methyl transferase enzyme mechanisms.[29,30] Nevertheless, the use of this chiral methyl group suffers from the following drawbacks: (i) the presence of a radioactive tritium atom causes difficulties in terms of synthesis, handling, storage, analysis, and waste management; (ii) the challenging measurement of enantiomeric excess (ee) in the case of isotopic chirality. So far, only fastidious syntheses of a well-controlled diastereoisomer (without epimerization of the chiral center) or enzymatic resolution, both associated with ^{3}H NMR analysis, have been disclosed to determine ee.[29,31] To circumvent these limitations, the design of specific deuterium-labeled probes may simplify the generation of stereogenic centers thanks to the nonradioactive nature of these analytes and their analysis with the possibility to use advanced techniques such as ^{2}H NMR in chiral liquid crystals (CLCs) to evaluate their enantiopurity ratios.[32–35]

In this work, we propose to replace the tritium atom of the chiral methyl group with a methyl moiety to obtain the nonradioactive chiral ethyl group. After the achievement of the first chemical synthesis of such crypto-optically active probes with a high deuterium

atom incorporation,[36] to completely describe each enantiomer, modern analytical techniques were used (Figure 2.1). It is important to note that some alkyl transferase enzymes tolerate various alkyl groups as ethyl, allyl, or propargyl during the transfer process,[37,38] and so chiral ethyl probes could be helpful for studies of this class of enzymes. As a matter of fact, the radioactive chiral ethyl group has already been used for the understanding enzymatic mechanisms.[39–42]

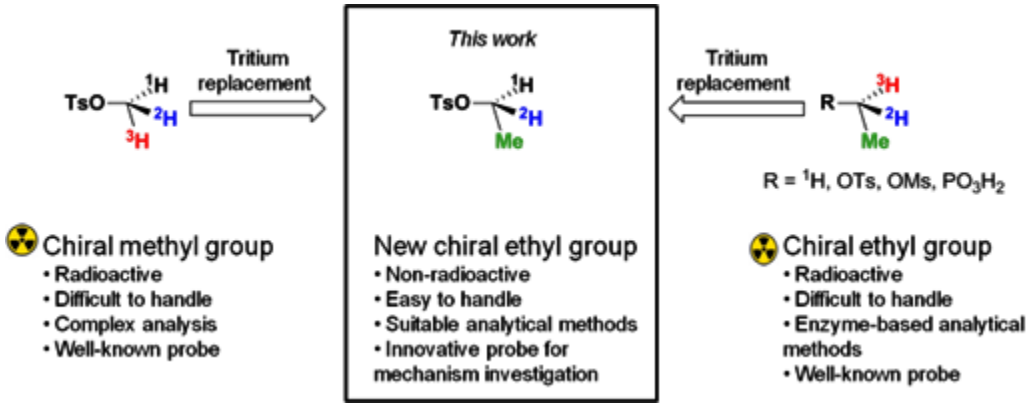

Figure 2.1: Goal of the work in this chapter

Our synthetic approach to the chiral ethyl group was inspired by the one described by Hammerschmidt et al. for the synthesis of chiral methyl tosylate[43] (Figure 2.2). First, the chloromethyldimethylphenylsilane **1** was converted to the corresponding alcohol **2** in good yield. Then, carbamate **3** was obtained by the condensation of bis((*S*)-1-phenylethyl)amine **4** with triphosgene followed by the addition of alcohol **2**. Carbamate **3** was then deuterated in the α-position of the silicon atom via two consecutive lithiation/deuteration sequences, allowing a ^{2}H incorporation over 99%. Then, the dideuterated carbamate **5** was alkylated using iodomethane through an optimized lithiation process. The use of t-BuLi at –50 °C led to a mixture of diastereoisomers **6** (Figure 2.2) with high conversion. Then the two diastereoisomers were separated using chiral HPLC. Treatment of monodeuterated **6** with DIBAL-H cleaved the carbamate moiety to give the corresponding chiral alcohol (not isolated due to its high volatility). A consecutive Brook rearrangement followed by the tosylation of the ethanol intermediate gave chiral ethyl tosylates **8**.

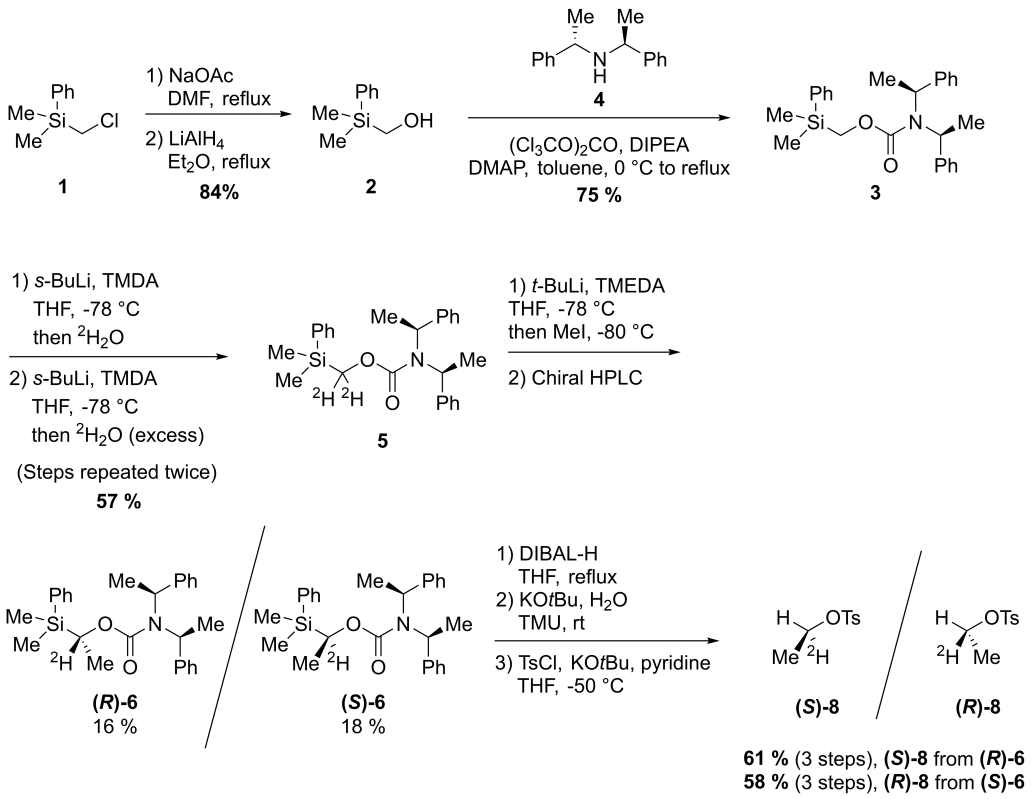

Figure 2.2: Synthesis of dueterated crypto-optically active probes (*R*)- and (*S*)-**8**

As the determination of the absolute configuration (AC) is essential for the use of such chiral molecules as probes,[44,45] a combination of several modern analytical methods for the characterization of isotopic chirality has been described. First, in 2007, X-ray crystallography and vibrational circular dichroism (VCD) were used to determine the AC of (*R*)-4-ethyl-4-methyloctane.[46,47] Then, quantum chemical (QC) computations were coupled with Raman optical activity[48] or VCD[49–51] experiments to provide essential information on various crypto-optically active compounds.

During our whole synthetic pathway, no information regarding the AC could be obtained by optical rotation, so VCD analysis was performed.[6,52–57] Figure 2.3 reveals mirror image signals for enantiomers. The most relevant signatures were observed between 1000 and 1050 cm^{-1} and between 1250 and 1350 cm^{-1}. To assign signals to products, QC calculations were performed (Figure 2.3), and then calculated and experimental IR and VCD

spectra were compared (Figure 2.3). The M06-2X-based frequencies were scaled down by a factor of 0.9725, giving the maximum similarity with the experimental VCD and IR spectra. Interestingly, although [^{2}H]-ethyl tosylate **8** is called crypto-optically active, it actually displays VCD activity.

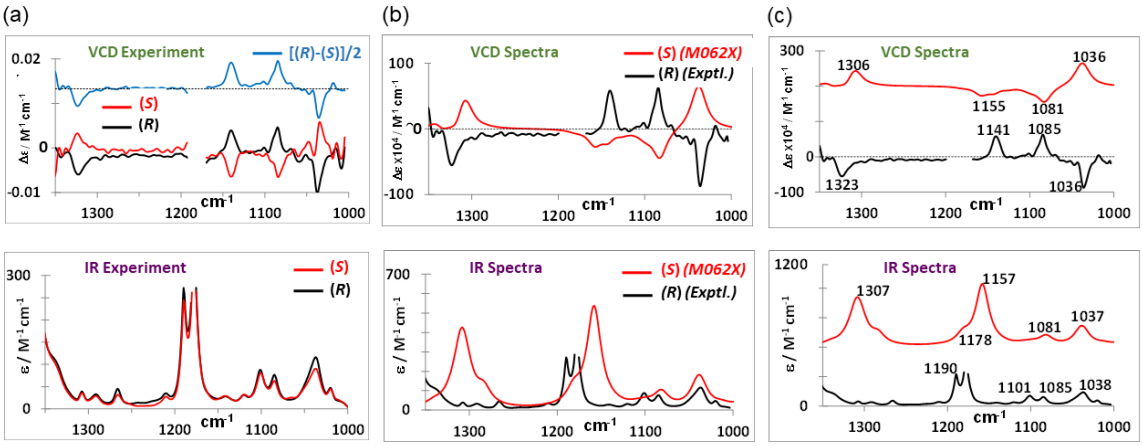

Figure 2.3: VCD and IR spectra of crypto-chiral probes (*R*)- and (*S*)-**8**

A comparison using the B3LYP functional indicates that M06-2X gives better agreement to the experiment overall and so only VCD spectra simulated with M06-2X are presented in Figure 2.3. The VCD band signs predicted that the *S*-stereoisomer appears clearly opposite to those seen for (*R*)-**8**. Therefore, both levels of calculation enabled confirmation of the AC of (*R*)- and (*S*)-**8** enantiomers in relation to the signs of the VCD signals (Figure 2.3). It is interesting to note that the corresponding *S*-(–) and *R*-(+) AC of [1-^{2}H$_1$]ethanol were determined by three methods (enzymatic,[58] chemical correlation from sugars,[59] and VCD[60]).

Finally, the isotopic enantiomers of **8** were studied with the help of ^{2}H-^{1}H 2D NMR recorded at 92.1 MHz and 297 K in the poly(γ-benzyl-l-glutamate) (PBLG)-based chiral mesophase (20.7% mPBLG/mtot). In such lyotropic CLCs, each monodeuterated enantiomer generates a single ^{2}H quadrupolar doublet (^{2}H-QD) when the spectral enantiodiscrimination occurs;[32–35,61] two ^{2}H-QD are therefore theoretically expected if the *R*/*S* ^{2}H signals are spectrally resolved.

This occurrence has been observed on the ^{2}H-^{1}H 2D NMR spectrum recorded at the natural abundance deuterium (NAD) level of commercial ethyl tosylate when DMF is used as organic cosolvent (Figure 2.4a). In this case, each monodeuterated enantioisotopomer ((*S*)-C*DH- and (*R*)-C*HD-) associated with the pro-(*S*) and pro-(*R*) hydrogenated enantiotopic position are detected. Note that using chlorofom, a weakly polar cosolvent, no spectral enantiodiscrimination occurs.[33,61]

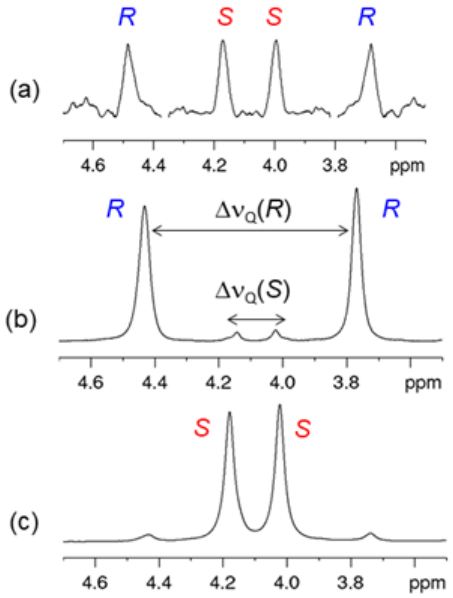

Figure 2.4: Anisotropic NAD NMR projections of (*R*)- and (*S*)-**8**

The enantiopurity of the two isotopically labeled compounds **8** (Figure 2.4b,c) has been determined at the same T (297 K) and using identical PBLG mass ratio (20.9%), thus leading to a magnitude of ^{2}H splittings identical to those observed on the anisotropic NAD NMR spectra. The large difference in intensity between each ^{2}H-QD of (*S*)-**8** and (*R*)-**8** reveals the presence of a significant enantioenrichment. Deconvolution of the signals indicates that the chiral ethyl tosylate was prepared with an ee greater than 90% for both isomers.

In conclusion, the first chemical synthesis of a nonradioactive chiral ethyl group was developed. Although the anisotropic ^{2}H NMR allowed enantiopurity evaluation, the VCD

analysis/QC calculation combination permitted the AC of each synthesized enantiomer of the chiral ethyl tosylate to be assigned. Due to their easier synthetic access and handling compared to that with their radioactive counterparts, such small crypto-optically active probes possess a great potential of applications to decipher alkyl transferase enzyme reaction mechanisms.

CHAPTER 3

The AC of a Mechanically Planar Chiral [1]Rotaxane

The work from this chapter can be found in the *Chirality* article "Absolute configuration of a [1]rotaxane determined from vibrational and electronic circular dichroism spectra."[62] I was responsible for computational modeling of this exotic compound in order to elucidate its AC. Our collaborators in France painstakingly pushed the limits of synthetic chemistry to both open up this unexplored class of mechanically chiral [1]rotaxanes and make these compounds in quantities that could be used for VCD measurements. ECD and VCD measurements were performed by the Crassous group at the University of Rennes in France.

3.1 Introduction

While many interlocked molecules, such as rotaxanes and catenanes, have been described in the literature over the last 30 years,[63–70] only little attention has been paid to the stereoselective synthesis of mechanically chiral rotaxanes to date.[71] In 2014, Goldup and co-workers reported the first method enabling the access to mechanically planar chiral (MPC)[72] [2]rotaxanes without using chiral separation techniques.[73] Soon after, they accomplished the diastereoselective synthesis of MPC [2]rotaxanes through the active template Cu-mediated alkyne–azide cycloaddition (AT-CuAAC)[74,75] reaction.[76] Recently, Leigh and co-workers developed a single-step enantioselective strategy leading to MPC [2]rotaxane enantiomers in 50% *ee*.[77] The emergence of novel stereoselective approaches has also highlighted the lack of techniques allowing the assignment of AC of such rotaxanes, in most cases determined using single crystal X-ray diffraction. However, obtaining suitable crystals remains highly challenging, pointing out the need to design alternative methods for assigning the absolute mechanical configuration of these interlocked chiral molecules. Within this framework, Goldup and Buma demonstrated that vibrational circular dichroism (VCD) spectroscopy has the potential to determine the absolute stereochemistry of such archi-

tectures.[78] Indeed, they showed that computed VCD spectra were in accordance with the experimental spectra of known AC, thereby providing a very useful means to resolve the AC of MPC [2]rotaxanes.

Very recently, I reported on the first diastereoselective synthesis of [1]rotaxanes using the AT-CuAAC reaction.[79] This method enabled the preparation of mirror-image MPC [1]rotaxanes with a high stereoselectivity. In this approach, the mechanically planar chirality of the obtained [1]rotaxane **1** was guided by the absolute configuration of the covalent stereogenic center attached at the base of the macrocycle. However, as I failed to produce a single-crystal, I were unable to attribute the absolute stereochemistry of (*S*)-**1**, either as $(S,\ R_{mp})$ or $(S,\ S_{mp})$ (see Figure 3.1).

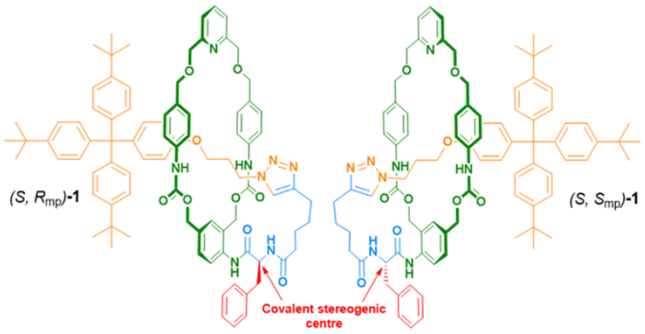

Figure 3.1: Structures of the two possible diastereomers of [1]rotaxane (*S*)-**1**.

In this chapter, the absolute configuration (AC) of **1** is determined using vibrational circular dichroism (VCD) and electronic circular dichroism (ECD) spectra. The experimental VCD and ECD spectra for (*S*)-**1** and (*R*)-**1** and their comparison to corresponding predicted spectra for the $(S,\ R_{mp})$ and $(S,\ S_{mp})$ diastereomers. The predicted spectra were obtained using density functional theory (DFT). This comparison analysis allowed us to establish the hitherto unknown AC of **1**.

3.2 Methods

The synthesis and ECD measurements of **1** were reported previously.[79] VCD and VA spectra were recorded on a JASCO FSV-6000 spectrometer with a 200 μm pathlength cell

for enantiomers of **1** dissolved in CD_2Cl_2. Two sets of measurements were performed, one with 3000 scans and another with 9000 scans. For the 3000 scan measurements, the concentrations of (*S*)-**1** and (*R*)-**1** were respectively 46.5 mg/mL and mg/mL. The corresponding concentrations for the 9000 scan measurements were 45.0 mg/mL and 38.0 mg/mL.

Initial conformational searches were performed with Conflex program[80] using interlocked starting geometries for the diastereomers, (*S, R_{mp}*)- and (*R, R_{mp}*)-**1**, in a 10 kcal/mol energy window. This search produced many structures without a mechanical stereogenic unit, so a second search was performed using the lowest energy interlocked conformation from the first search. This second search provided many low-energy conformations for both diastereomers, with interlocked conformations being identified as the lowest energy structures. There were 2650 conformers for (*S, R_{mp}*)-**1** in in 10 kcal/mol window. For (*R, R_{mp}*)-**1**, since there were only 321 conformers in 10 kcal/mol window, I examined 870 conformers in 20 kcal/mol window. Subsequent hand-filtering of the (*R, R_{mp}*)-**1** structures, for eliminating the non-interlocked structures, resulted in 430 interlocked structures and these structures were used for quantum chemical (QC) calculations. All 2650 (*S, R_{mp}*)-**1** structures were used for QC calculations, without any hand-filtering. This process was repeated using the (*R, S_{mp}*)- and (*S, S_{mp}*)-**1** structures, but no additional unique conformations were found. I also visually inspected each interlocked conformer prior to QC calculations to verify that the mechanical stereogenic unit had not inverted during the conformational search.

The numerous conformations and the large size of the [1]rotaxane diastereomers rendered QC calculations time consuming and computer intensive. Following the work of Koenis et al.,[78] I performed an initial geometry optimization using a density functional tight-binding (DFTB) method with the 3ob-3-1 parameter set[81] to identify lower energy structures prior to moving onto more time-consuming DFT optimization and frequency calculations. The DFTB-optimized structures in the lowest 2 kcal/mol energy window were selected for further processing. After hand-filtering to eliminate non-interlocked struc-

tures, this resulted in 456 interlocked conformations for (S, R_{mp})- and 92 for (R, R_{mp})-**1**, which were carried over for DFT optimization using the B3LYP functional and 6-31G* basis set.[82] VCD and ECD calculations were then performed on the 76 (S, R_{mp})- and 33 (R, R_{mp})-**1** optimized conformations in the lowest 2 kcal/mol energy window. The lowest energy conformers of (S, R_{mp}) are ∼3 kcal/mol lower in energy than those of (R, R_{mp}). The lowest energy conformer (#269 in the list of conformers generated by Conflex) of the (S, R_{mp}) diastereomer is displayed in Figure 3.2.

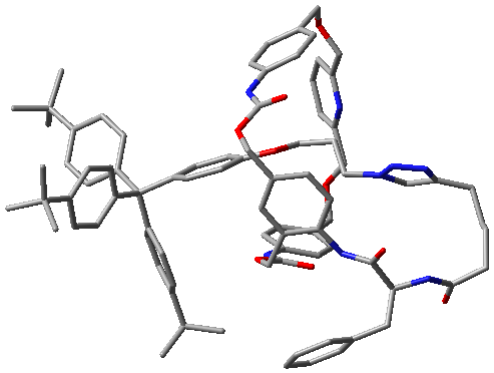

Figure 3.2: Lowest energy conformer of (S, R_{mp})-**1**. Hydrogen atoms are omitted for clarity

3.3 Methods

All QC calculations were performed using Gaussian 16.[83]. Vibrational animations and electron density maps were generated using GaussView program. The VCD and ECD spectra were simulated using CDSpecTech[84] and contributing conformers were weighted by their Gibbs energies for all spectra. The VCD and ECD spectra for (R, R_{mp})-**1** were each multiplied by –1 to generate those for (S, S_{mp})-**1**.

3.4 Results and Discussion

3.4.1 VCD

Two separate experimental VCD measurements were performed on (*S*)- and (*R*)-**1**, first with 3000 scans and then another with 9000 scans. Since experimental VCD signals were weak, a weighted average of these two measurements was taken, with each measurement

weighted by $\sqrt{N}$, where N is the number of scans used for the measurement. The resulting VCD spectra (Figure 3.3a) have a sharp mirror-image band at $\sim$1540 cm^{-1} and small bands at $\sim$1246, 1207, 1200 and 1041 cm^{-1}.

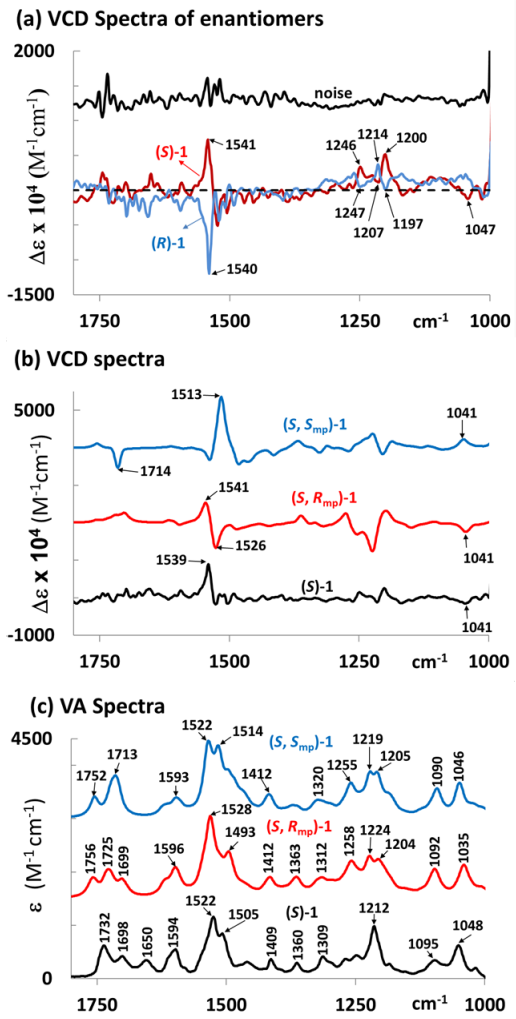

Figure 3.3: VCD and VA spectra of (*S*)-**1** and the simulated spectra of (*S, R*$_{mp}$)- and (*S, S*$_{mp}$)-**1**

The VCD spectrum for (*S*)-**1**, obtained as one-half the difference between enantiomer spectra is compared to those predicted for (*S, R*$_{mp}$) and (*S, S*$_{mp}$) diastereomers in Figure 3.3b. The experimental VCD spectrum of (*S*)-**1** has positive VCD band at 1539 cm^{-1} and there is a hint of adjacent negative VCD at $\sim$1520 cm^{-1}, but it is barely above the noise level. The predicted VCD spectrum for (*S, R*$_{mp}$) shows a positive band at 1541 cm^{-1} and negative band at 1526 cm^{-1}, both of roughly equal magnitudes. Visualization of the vi-

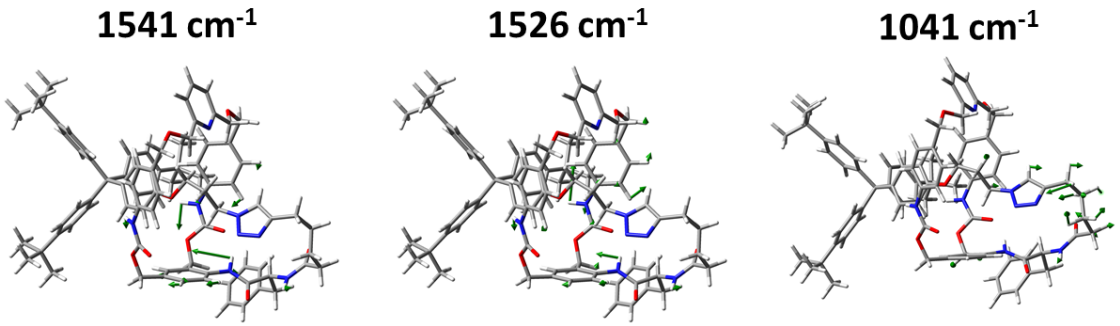

Figure 3.4: Depiction of vibrations of (S, R_{mp})-**1** as discussed in the text

brations responsible for this bisignate feature reveals a combination of Amide II and C–C stretching of neighboring benzene ring. All three such amide-benzene groups are participating to produce this vibration along the macrocycle. The predicted VCD spectrum for (S, S_{mp}) shows a triplet of neighboring bands, with large positive at 1513 cm^{-1} and two weak negative bands on each side. Visualization of the vibrations responsible for 1513 cm^{-1} band reveals it to also be a concerted Amide II and benzene ring C–C stretching vibration but localized to the benzene ring closest to the stereocenter. It is somewhat difficult to draw a definitive conclusion on the AC of **1** based solely on this region of the experimental VCD spectrum. In addition, the commonly used similarity analyses[84,85] between experimental and theoretical VCD spectra are unreliable when there are only a small number of spectral features for comparison so they are not included.

However, there are two experimental VCD bands that have favorable comparisons with those in the predicted spectrum for (S, R_{mp}), but not in that for (S, S_{mp}).

1. No significant VCD is apparent in the experimental spectrum in the amide I region ($\sim$1700 cm^{-1}). The asymmetric stretch of both amides near the stereocenter has a scaled frequency of 1702 cm^{-1} for (S, R_{mp}). The associated rotational strength is weak, so much so that it is barely visible in the simulated VCD spectrum for (S, R_{mp}). This prediction is in line with the experimental observation. In contrast to this experimental observation, the VCD spectrum of (S, S_{mp})-**1** has a sharp negative

VCD band at 1714 cm^{-1}. Visualization of vibrations of (*S, S_{mp}*)-**1** indicates that 1714 cm^{-1} band arises from the amide group that connects the stereocenter to the macrocycle.

2. The negative experimental VCD band at 1041 cm^{-1} is reproduced in the predicted spectrum for (*S, R_{mp}*)-**1**, while the corresponding band for (*S, S_{mp}*)-**1** has opposite sign. Visualization of vibrations reveals that 1041 cm^{-1} band is a result of CH rocking along the lasso portion of the rotaxane, specifically between the alkyl chain connecting the stereocenter and the triazole heterocycle.

Based on these two observations, the experimental VCD spectrum of (*S*)-**1** can be preferentially associated with the (*S, R_{mp}*) diastereomer. To ensure that this conclusion will not be altered at higher level calculations, I have undertaken VCD calculations using BP86 functional[86] and TZVP basis set[87] for the lowest energy conformers of (*S, R_{mp}*)- and (*S, S_{mp}*)-**1**. The nature of vibrations associated with scaled frequencies of 1546, 1521, and 1041 cm^{-1} are depicted in Figure 3.4.

3.4.2 ECD

I have previously reported the experimental ECD spectra of (*S*)- and (*R*)-**1** along with their synthesis.[79] The experimental spectra contain three clear mirror-image bands for enantiomers, in the 220 to 300 nm region, with (*S*)-**1** showing negative–positive–negative sequence of ECD bands. The simulated ECD spectra of (*S, R_{mp}*)- and (*S, S_{mp}*)-**1** appear as near mirror-image spectra, despite their diastereomeric relationship. This may indicate that the ECD contribution of the mechanically planar stereogenic unit is much greater than that of the stereocenter, a phenomenon that has been reported for axial chirality.[4] The simulated ECD spectrum of (*S, R_{mp}*)-**1** better matches the experimental ECD spectrum, than (*S, S_{mp}*)-**1**, with negative–positive–negative sequence of bands observed for (*S*)-**1** being reproduced in the simulated spectrum (Figure 3.5).

The simulated spectrum of (*S, S_{mp}*)-**1** is a result of two distinct classes of conformers,

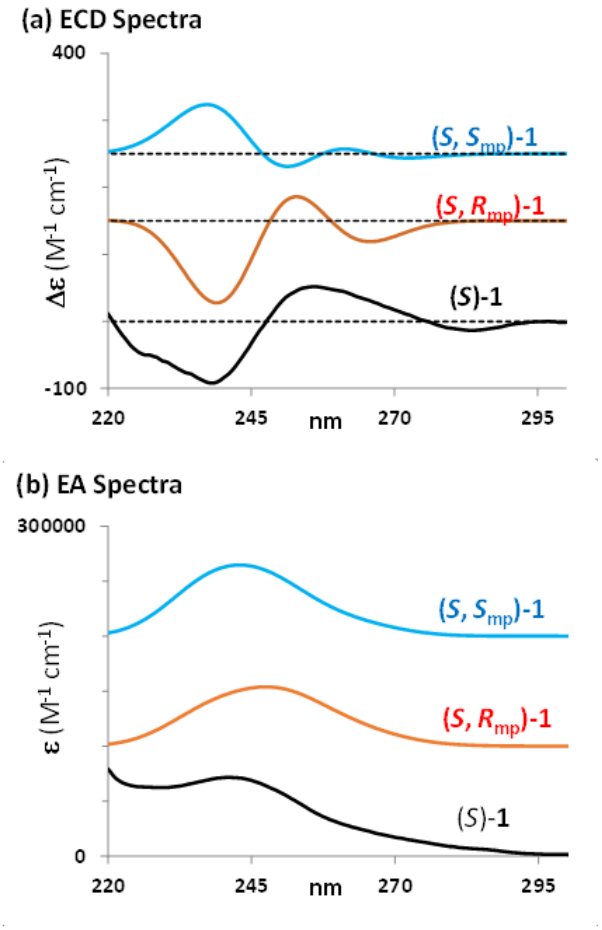

Figure 3.5: ECD and EA spectra of (S, R_{mp})- and (S, S_{mp})-**1**

one set with two ECD bands and another set with three (Figure 3.6). To discuss MO contributions to the simulated ECD spectrum of (S, R_{mp}), I focus our analysis on two lowest energy structures of (S, R_{mp})-**1**, conformers **C269** and **C463**, which serve as representatives of these two classes and are also the two lowest energy structures of (S, R_{mp})-**1**, with roughly equal populations ($\sim$5% by Gibbs energy).

The ECD bands of interest for conformers C269 and C463 are a result of excited states that involve many molecular orbitals (MOs), which obscured the nature of their origin. To further investigate these transitions, I generated the Natural Transition Orbitals (NTOs)[88] of the excited states that contributed the most overall to the ECD spectrum for **C269** and **C463**. This analysis reveals that conformer **C269** has an intense π–π* ECD band centered

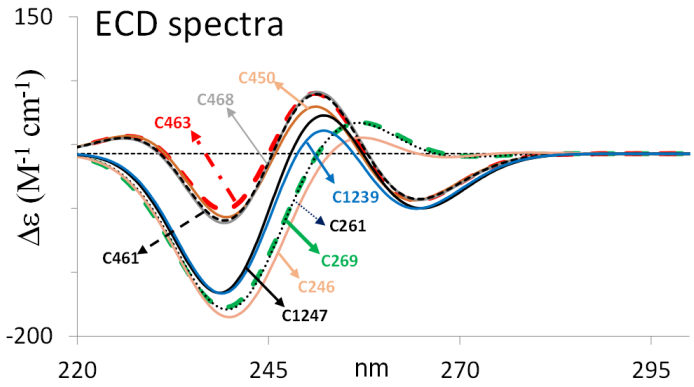

Figure 3.6: ECD spectra of the lowest energy conformers of (S, R_{mp})-**1**

at ∼240 nm. This band is a result of a transition from a π MO along the macrocycle to a π^* MO on the stopping group, but this also includes some contribution from the lower portion of the macrocycle (Figure 3.7) There is another π-π^* ECD band centered at ∼260 nm that is a result of MO contributions from the macrocycle near where the mechanical stereogenic unit originates (Figure 3.8).

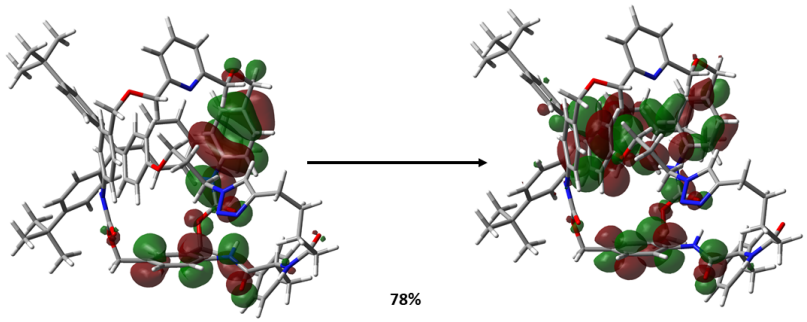

Figure 3.7: NTOs for the 240 nm ECD band of C269 of (S, R_{mp})-**1**

Conformer C469 has three ECD bands of roughly equal intensity at 240, 250, and 265 nm. There is a π–π^* band centered at 240 nm that, much like the 240 nm C269 band, involves a transition from a π MO from the macrocycle to a π^* MO on the stopper. NTO analysis reveals an additional contributing π-π^* transition localized on the left-hand side of the macrocycle (Figure 3.9b). The second ECD band is another π-π^* centered at 250 nm. NTO analysis decomposes the transition into three pairs of MOs, each with roughly equal

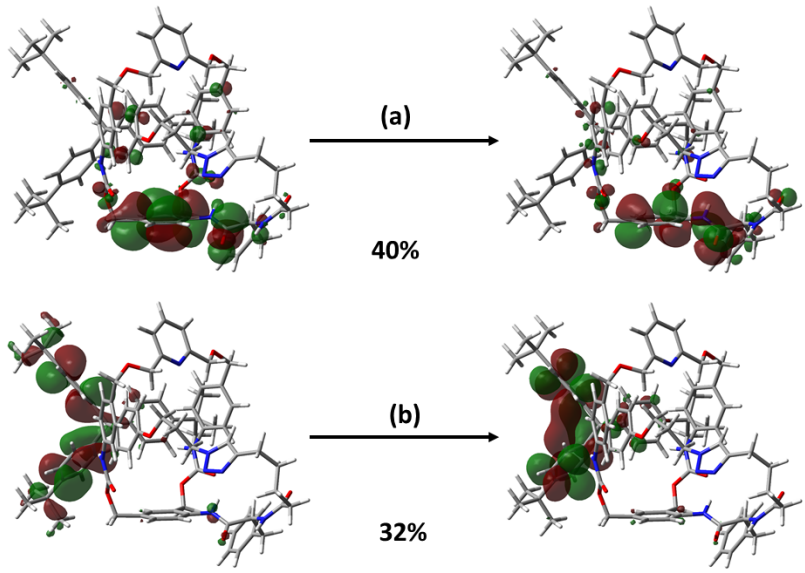

Figure 3.8: NTOs for the 260 nm ECD band of C269 of (S, R_{mp})-**1**

occupancy $\sim$30%) (see Figure 3.10). Electron density pictures for 265 nm ECD band are displayed in Figure 3.11.

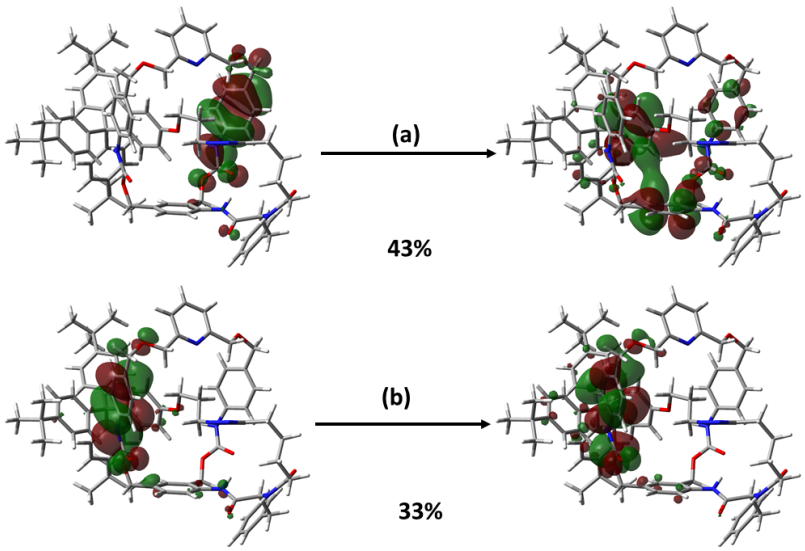

Figure 3.9: NTOs for the 240 nm ECD band of C463 of (S, R_{mp})-**1**

The simulated ECD bands for (S, R_{mp})-**1** show great agreement at the B3LYP/6-31G* level, a level of theory that has been shown to have large errors for charge-transfer interactions in the calculation of Rydberg states.[89–91] To test the validity of our results at

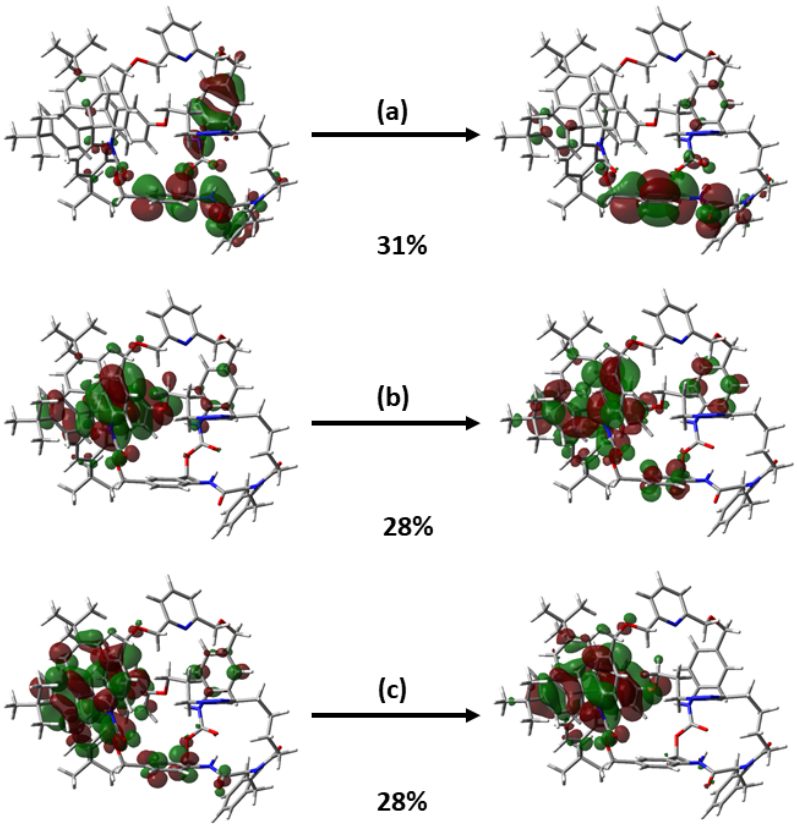

Figure 3.10: NTOs for the 250 nm ECD band of C463 of (S, R_{mp})-**1**

the B3LYP/6-31G* level, I carried out additional single-point TD-DFT calculations on the lowest energy structures of (S, R_{mp}) and (S, S_{mp})-**1** at the CAM-B3LYP/6-31G* level using the previously calculated B3LY/6-31G* optimized geometries. CAM-B3LYP has been shown to predict excited-states with better accuracy than B3LYP thanks to the addition of a long-range correction.[92] The corresponding simulated spectra are presented in Figure 3.12. The computed transition wavelengths require a much larger scale factor (1.075) to be consistent with experiment than the B3LYP transition wavelengths (1.01). However, the calculations reproduce the trend from the B3LYP/6-31G* level, giving near mirror-image signs for ECD bands between (S, R_{mp}) and (S, S_{mp}). In addition, the negative-positive-negative ECD triplet at 240, 255, and 265 nm for (S, R_{mp}) is simulated with matching signs observed in the experimental spectrum of (S)-**1**.

The success of current ECD calculations may be caused by coupling between aromatic

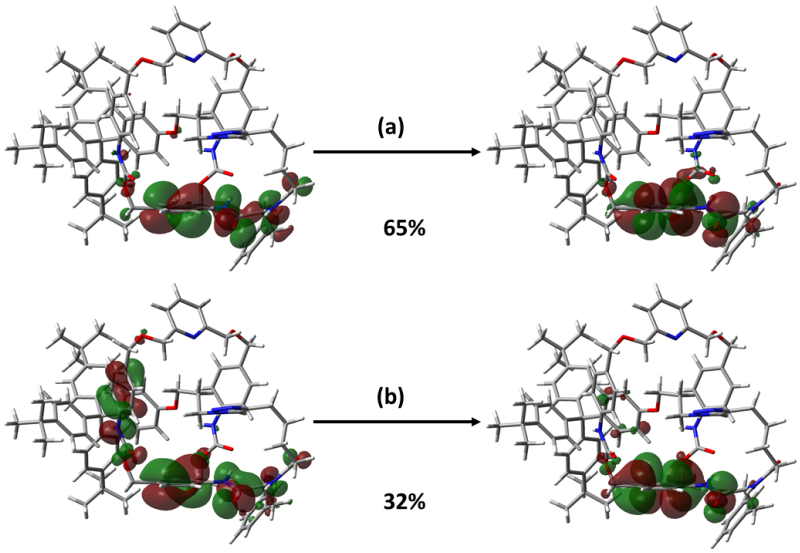

Figure 3.11: NTOs for the 265 nm ECD band of C463 of (S, R_{mp})-**1**

rings in the macrocycle and the stopping group. This coupling is evidenced by the high degree of participation from them in ECD transitions, as noted in our earlier NTO analysis. The relative positions of the aromatic rings in macrocycle and stopping group are dictated by their mechanical planar chirality, hence the near mirror-image ECD signal between epimers.

3.5 Conclusions

Based on the comparison of experimental VCD spectrum of (*S*)-**1** with those predicted for (S, R_{mp}) and (S, S_{mp}) diastereomers there is some evidence for associating (*S*)-**1** with (S, R_{mp})-configuration. This AC was confirmed by the comparison of experimental ECD spectrum of (*S*)-**1** with those predicted for (S, R_{mp}) and (S, S_{mp}) diastereomers. Thus, the current VCD and ECD spectroscopic investigation leads to definitive assignment of AC associated with mechanically planar stereogenic unit in [1]rotaxanes.

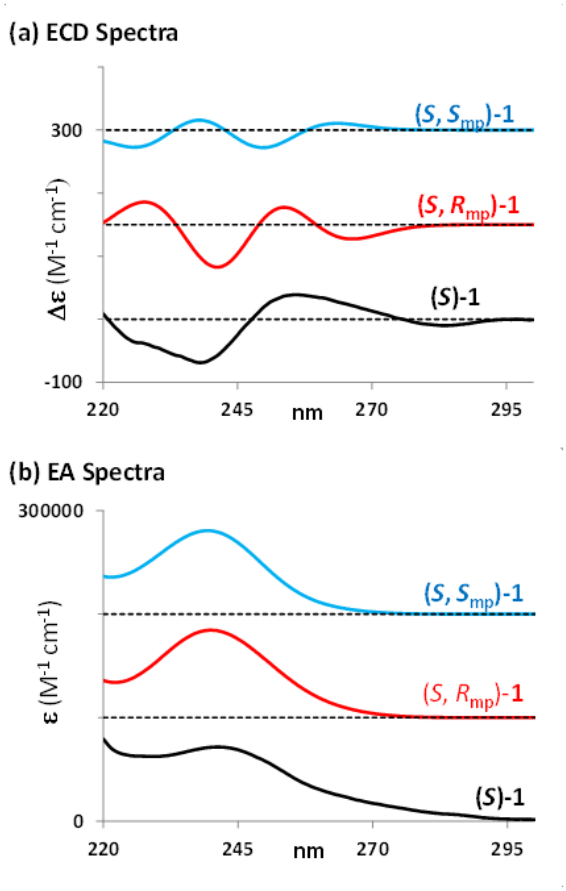

Figure 3.12: ECD and EA spectra for (S, S_{mp})- and (S, R_{mp})-**1** as compared to the experimental spectra

CHAPTER 4

Chiroptical Studies of Hexahydrocurcumin and Octahydrocurcumin

The work in this chapter can be found in the *Chirality* article "Chiroptical spectroscopic studies for the absolute configuration determination of hexahydrocurcumin and octahydrocurcumin".[93] I was responsible for computational modeling of these flexible compounds in order to determine the applicability of common AC determination approaches for these biologically relevant molecules. Our collaborators at the Sami-Sabinsa Corporation painstakingly synthesized and isolated enantiopure samples of both stereoisomers of hexa- and octahydrocurcumin in quantities that could be used for ORD, ECD, and VCD measurement. I performed ORD, ECD, and initial VCD measurements of these compounds. Final VCD measurements presented herein were performed at Biotools by Jordan Nafie, Ph.D.

4.1 Introduction

Turmeric, used for over a thousand years as an Ayurvedic preparation in traditional medicine, is found in the rhizomes of *Curcuma longa* and related plants. The active ingredients in turmeric are three naturally occurring polyphenols belonging to a small class of linear diarylheptanoids known as curcuminoids. These compounds (see Figure 4.1) are curcumin and its demethylated derivatives, demethoxycurcumin and bisdemethoxycurcumin, all of which are plant metabolites of turmeric. It has been shown that these curcuminoids account for the major health and therapeutic effects associated with *C. longa*. Curcumin is one of the intensely investigated phytonutrients from several health promotional angles,[94,95] and has received much scientific interest for its therapeutic potential against oxidative stress,[96] as an anti-inflammatory,[97,98] its anti-cancer properties,[99–101] and enabling stem cell therapy.[102] Despite its extensively reported pharmaceutical and pharmacological activities, it has also been recognized that curcumin is not highly bioavailable and unstable in alkaline conditions. This seeming paradox has given rise to several speculations whether

the degradants[103] or metabolites[104] of curcumin are responsible for the physiological response. Among these, the reductive metabolites of curcumin have captured the imagination of scientists for their therapeutic potential.[104] The reductive metabolites, *inter alia*, include (see Figure 4.1) dihydrocurcumin, tetrahydrocurcumin, hexahydrocurcumin (HHC), and octahydrocurcumin (OHC) which are obtained through progressive reduction of the two C–C double bonds and two keto functional groups in curcumin.

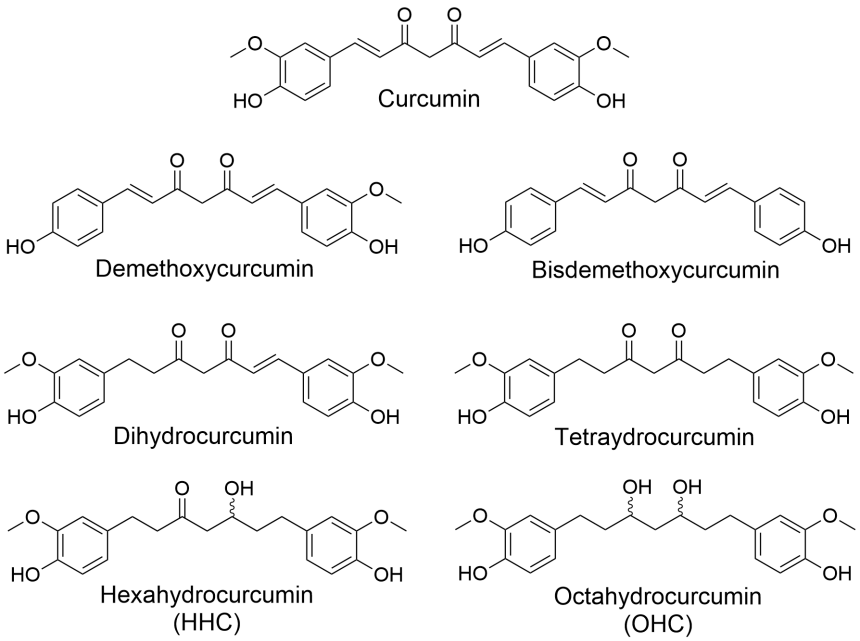

Figure 4.1: Structures of the curcuminoids discussed in this chapter. Only their keto forms are shown here.

Recently, it was reported that a strain of Enterococcus avium isolated from human intestine produced nearly enantiopure (–)-HHC from tetrahydrocurcumin.[105] It was also demonstrated that this same bacterium strain further metabolizes the chiral HHC to OHC.[106] While the significance and mechanism of production for optically active HHC and OHC by this bacterium remains undetermined, it is well-known that gut microbiota play an important role in human metabolism of curcumin[107,108] and in clinical trials curcumin's low bioavailability is suggested to be due to its rapid metabolism.[109] Curcumin is primarily reduced by Phase I enzymes in a stepwise manner to dihydrocurcumin, tetrahydrocurcumin, HHC and OHC.[99,108] While di- and tetrahydrocurcumin are achiral, HHC and OHC pos-

sess one and two stereocenters respectively. Both HHC and OHC have been shown to possess bioactivities and pharmacological profiles on par and even superior to curcumin and have been the interest of extensive biomedical research.[110,111]

While numerous reports have identified HHC or OHC as metabolites in animal models, it remains unclear whether these compounds are formed enantioselectively in the human metabolism of curcumin. Evidence thus far has shown that (*R*)-HHC can be formed from the reduction of tetrahydrocurcumin by an intestinal resident bacteria isolated from human feces.[105] In nature, HHC has been isolated in both the (*R*)- and (*S*)- forms in edible plant materials. For example, (*S*)-HHC occurs in ginger[112] whereas (*R*)-HHC occurs in *Alpinia officinarum*.[113] It is also reported that racemic HHC occurs[114] in edible *C. xanthorrhiza*. Thus, racemic as well as enantiomeric forms of HHC seem to occur in the plant kingdom. A recent review describes the various useful medicinal properties of HHC in detail.[115]

OHC and HHC were first isolated as natural products from ginger.[112–114,116] The absolute configuration (AC) of naturally-occurring HHC in *Alpinia officinarum* was determined to be (–)-(5*R*) via empirical correlations using similar linear diarylheptanoids and their common Cotton effect at 300 nm.[113] Empirical correlations are often used to assign the AC of natural products, but the possibility for empirical correlations leading to incorrect AC assignments should be kept in mind.

Uehara et al. reported the isolation of (–)-(3*S*,5*S*)-OHC from *C. xanthorrhiza* and the AC assignment was based on exciton chirality method for the p-dimethylaminobenzoate derivative of methylated octahydrocurcumin.[114] The dibenzoate method uses the signs of the Cotton effect associated with benzoate chromophores to determine the clockwise or counter-clockwise orientation of the benzoate chromophores, and thus the AC of the original molecule.[114,117] Exciton chirality rules such as this can lead to confident AC assignments but can be tenuous should the underlying rule be improperly applied.[117] The same enantiomer was also isolated from *Zingiber officinale*[118] whereas its mirror image form, (+)-(3*R*,5*R*)-OHC, was isolated from the rhizomes of a Chinese medicinal plant, *Tacca*

chantrieri.[119]

To further probe the chirality of these curcumin derivatives, I set out to independently determine the ACs of the enantiomers of HHC and OHC using experimental and predicted Vibrational Circular Dichroism (VCD), Electronic Circular Dichroism (ECD) and Optical Rotatory Dispersion (ORD) spectroscopies. As each of these complementary chiroptical spectroscopies possesses inherent advantages and disadvantages for inferring the AC, a consensus AC assignment may be obtained for the enantiomers of HHC and OHC, by combining these three methods.

4.2 Methods

4.2.1 Synthesis of hexahydrocurcumin and octahydrocurcumin

HHC and OHC were synthesized by reported procedures in the literature, and the physical and spectral properties matched the reported values.[119] The enantiomers of HHC were separated preparatively by supercritical fluid chromatography (SFC). The first and second eluted peaks had specific optical rotations (SORs) of –10.7 and +13.1, respectively, at 589 nm in $CHCl_3$ solvent (c = 0.5). These SOR values are consistent with those found in the works of Niwa et al. and Itokawa et al.[105,113] (*S*)-Hexahydrocurcumin was also isolated in-house from ginger with a measured value of $[\alpha]_D$ = +10.9 (c = 1.01, $CHCl_3$). This served as an additional reference material.

4.2.2 Octahydrocurcumin

To HHC (5 g), taken in 40 ml ethanol and 10 ml THF, sodium borohydride (1.25 eq) was added portion wise with stirring at room temperature for 4–5 hrs. Complete conversion was observed by TLC. After evaporating off the solvent, the reaction mixture was quenched in diluted HCl followed by extraction with ethyl acetate. The ethyl acetate extract was then washed with water and brine sequentially, followed by drying over sodium sulphate. The solvent was evaporated to yield crude OHC (4.5 g). Slurrying with hexane yielded pure OHC (4.0 g).

OHC was easily separated into meso and racemic forms by their differential solubilities. Solubility experiments were tried with dichloromethane, dichloromethane-methanol mixture, and chloroform, which led to the observation that repeated chloroform washes of a mixture of meso- and racemic-OHC preferentially solubilized the meso form, highly enriching the less soluble racemic form (>98%). This enrichment was monitored and quantified by ^{1}H-NMR (see Figures S2-S5) using characteristic signals at 4.3 ppm for racemic- and 4.5 ppm for meso-OHC. This highly enriched racemic-OHC sample was the input for preparative SFC for the separation of enantiomers. The first and second eluted peaks had SORs of +10.3 and –8.63, respectively, at 589 nm in ethanol solvent (c = 0.5). The mirror image ORD data for the enantiomers of OHC, and abovementined NMR data, clearly indicated the absence of meso impurity in OHC enantiomer samples.

4.2.3 Crystal structure

The pure sample of racemic octahydrocurcumin was separated into optical antipodes using SFC. The first eluted peak material was crystallized, and x-ray quality crystals were obtained. A clear colorless plate-like specimen, with approximate dimensions 0.086 x 0.191 x 0.364 mm, was used for the x-ray crystallographic analysis. The x-ray intensity data were measured at Princeton University, Princeton, NJ on a Bruker D8 Venture Photon 3 system equipped with a IμS microfocus source (Cu Kα, λ = 1.54178 $\AA$). A total of 4743 frames were collected. The total exposure time was 2.25 h. Using Olex 2,[120] the structure was solved at Vanderbilt University with the ShelXT[121] structure solution program using intrinsic phasing and refined with the ShelXL[122] refinement package using least squares minimization. Disorder in one of the two methoxyphenol groups was modeled over two positions without additional restraints.

4.2.4 ORD and circular dichroism measurements

SOR measurements at 589 nm were done at Robertson Microlit Laboratories, Ledgewood, NJ using an Anton Parr MCP 200 polarimeter in chloroform solvent for HHC and ethanol

solvent for OHC. ORD measurements were done at Vanderbilt University using an Autopol IV polarimeter at six different wavelengths, 633. 589, 546, 436, 405, and 365 nm. These ORD measurements were done in chloroform solvent for HHC and methanol for OHC, which gave mirror-image curves for the enantiomers. The electronic absorption (EA) and ECD measurements were performed on a JASCO-1500 spectrometer in chloroform solvent for HHC and methanol for OHC. VCD and vibrational absorption (VA) measurements were performed, for both enantiomers, on ChiralIR single photoelastic modulator (PEM) instrument at BioTools, Inc., in $CDCl_3$ for HHC and in methanol-d_4 for OHC.

4.2.5 Calculations

I performed an initial Conflex[80] conformation search on (*R*)-HHC and *SS*-OHC in a 20 kcal/mol energy window. I then optimized these conformations using the semi-empirical PM6 method[123] in Gaussian 16[83] prior to DFT optimization. I then took the unique conformers in the lowest 5 kcal/mol energy window and performed an additional optimization at the B3LYP[86,124]/6-31G*[125] level. For HHC, the unique conformers in the lowest 5 kcal/mol energy window were then optimized at the B3LYP/6-311++G(2d,2p)[123,126,127] level and a subsequent optimization was performed including a Polarizable Continuum Model (PCM)[128,129] to represent the solvent. The conformers whose Gibbs energies were within lowest 2 kcal/mol energy window were used for ECD, ORD, and VCD calculations. The two –OH functional groups in OHC were changed to –OD for VCD calculations using PCM to represent the methanol-d_4 solvent. A smaller cutoff of 2 kcal/mol was used to filter unique, low-energy conformations of OHC at the B3LYP/6-31G* level. The number of unique conformers obtained from each step in this workflow for HHC and OHC are listed in Table 4.1.

For HHC, the structures optimized at the B3LYP/6-31G* level in the lowest 5 kcal/mol energy window were additionally optimized at the ωB97X-D42/def2-TZVP level and then again at the ωB97X-D/def2-TZVP[130] level with PCM prior to VCD calculations. ECD and

Level of Theory	HHC	OHC
Conflex	12,563	13,883
PM6	2,307	2,002
B3LYP/6-31G(d)	222	43
B3LYP/6-311++(2d,2p)	186	38
B3LYP/6-311++(2d,2p)/PCM	40	38
B3LYP/def2-TZVP/PCM	33	–

Table 4.1: Number of unique, low-energy conformers for HHC and OHC in our computational workflow

ORD calculations of ωB97X-D/def2-TZVP/PCM optimized structures were performed only if they were in the lowest 2 kcal/mol Gibbs energy window based on frequency calculations.

For OHC, additional ECD calculations were performed using the CAM-B3LYP[131] functional using the structures optimized at the B3LYP/6-311++G(2d,2p)/PCM level. The calculated VCD and ECD intensities for *SS*-OHC were multiplied by –1 to give the corresponding values for (*R, R*)-OHC. The ECD and VCD spectra were simulated using CD-SpecTech.[84] The spectral similarity overlap analyses were undertaken using the Sim functions, as described previously.[132]

4.3 Results and Discussion

4.3.1 VCD

The experimental and calculated VDF, VCD, and VA spectra for HHC in $CDCl_3$ are presented in Figure 4.2. The original spectra were measured up to 1800 cm^{-1}, but due to the lack of measured VCD activity, the 1800–1500 cm^{-1} region is not shown in Figure 4.2. The maximum SimVCD value is +0.548 and the maximum SimVDF value is +0.588. These values are larger than the recommended reliability threshold of 0.4[132,133] leading to a confident assignment of (–)-(*R*)-HHC.

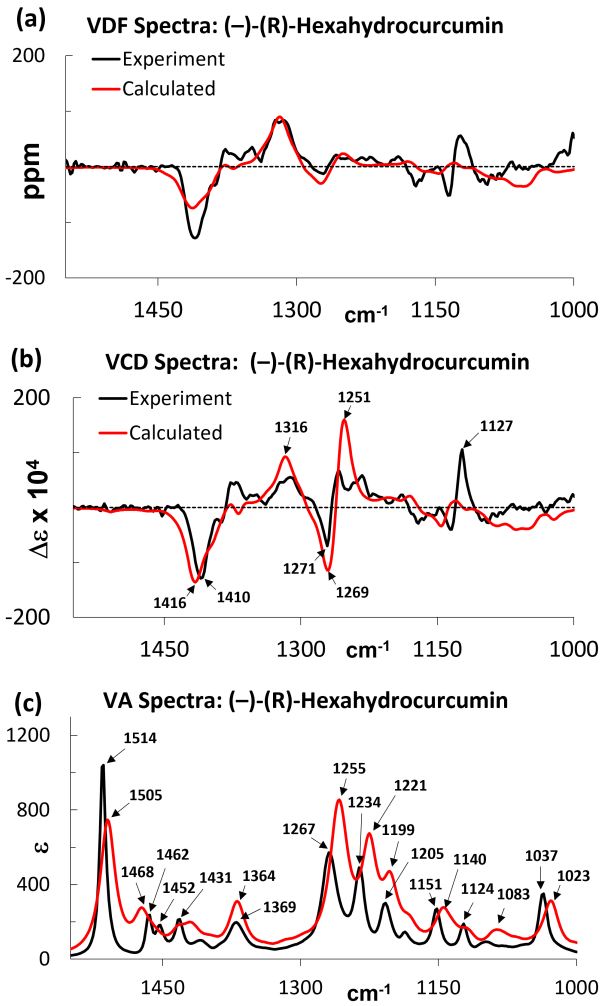

Figure 4.2: Comparison of (A) VDF, (B) VCD, and (C) VA spectra for (–)-HHC in $CDCl_3$ and (*R*)-HHC

The dominant feature in the predicted VCD spectrum is the bisignate feature, negative at 1269 and positive at 1251 cm^{-1}. To further investigate these VCD bands, I visualized the vibrations of the lowest energy conformer (see Figure 4.3) with 14.8% population by Gibbs energy. The 1269–1251 cm^{-1} bisignate VCD bands are predominately a result of ring breathing motion along with methylene vibrations along the alkyl chain.

The experimental and calculated VDF, VCD, and VA spectra for OHC in methanol-d_4 are presented in Figure 4.4. The VCD and VA spectra were measured up to 1800 cm^{-1}, but due to the lack of measured VCD activity, the 1800–1550 cm^{-1} region is not displayed

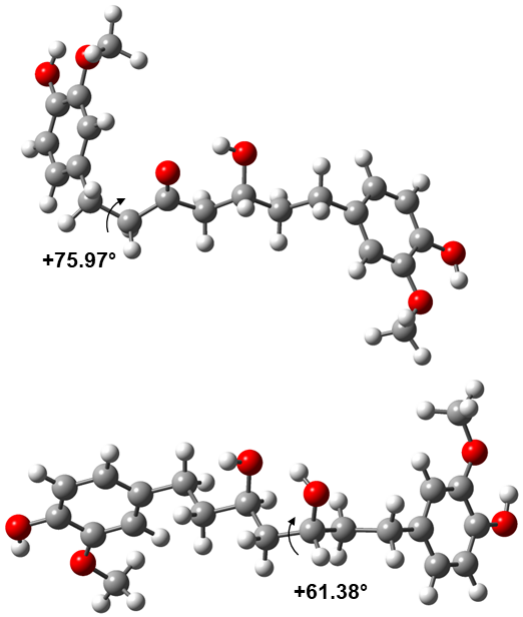

Figure 4.3: Lowest Gibbs energy structures of (*R*)-HHC and (bottom) (*R, R*)-OHC

in Figure 4.4. The simulated OHC spectra are predominately due to a single conformation with ∼53% population. Previously, I recommended that for a confident AC assignment, both SimVCD and SimVDF magnitudes should be 0.4 or greater.[132,133] The spectral similarity in the 1550 to 1260 cm^{-1} region (Figure 4.4) points to an assignment of (+)-(*R, R*)-OHC, because maximum SimVCD (0.564) and SimVDF (0.650) values are both larger than minimum recommended values. However, the similarity overlap in the 1550 to 1200 cm^{-1} region yields smaller SimVCD (0.41) and SimVDF (0.58) values, than those in the 1550 to 1260 cm^{-1} region for the following reasons. While the experimental VCD spectrum shows only one bisignate VCD feature, positive at 1278 and negative at 1269 cm^{-1}, the predicted spectrum shows two bisignate VCD features: one with positive at 1284 and negative at 1263 cm^{-1} and the second with positive at 1256 and negative at 1248 cm^{-1}. Since the predicted VCD features in the 1260–1240 cm^{-1} region show a larger mismatch with those in the experimental spectrum, the maximum SimVCD value in the 1550 to 1200 cm^{-1} region comes out to be lower than that in the 1550 to 1260 cm^{-1} region. Yet, the magnitudes of SimVCD (0.41) and SimVDF (0.58) also meet the criterion mentioned above when the

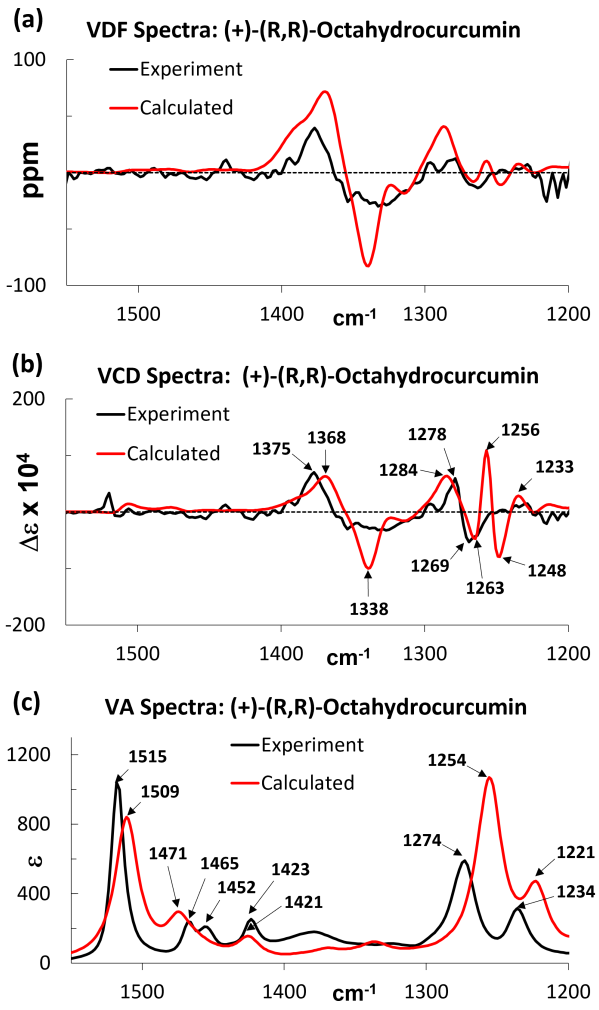

Figure 4.4: VDF, VCD, and VA spectra for (+)-OHC in MeOD and (R,R)-OHC

entire 1550 to 1200 cm^{-1} region is included in the Sim analysis. Nevertheless, since the magnitude 0.41 is close to the 0.40 threshold, it will be comforting to obtain additional evidence for the AC assignment of OHC (vide infra).

The current scaling factor used in Figure 4.4 yields the maximum possible SimVCD, however this scale factor results in a shift of the predicted intense VA 1254 cm^{-1} band by $\sim$20 cm^{-1} from the experimental 1274 cm^{-1} VA band. The simulated VA band is associated with the (+,–)-bisignate at 1256 and 1248 cm^{-1}. On the other hand, the (+,–)-bisignate VCD feature at 1284 and 1263 cm^{-1}, is associated with absorption at the high frequency shoulder of 1254 cm^{-1} VA band. When vibrational modes are visualized for the lowest

energy conformer (Figure 4.3), the 1256–1248 cm^{-1} bisignate VCD is predominantly associated with a combination of ring breathing motions of both phenyl rings in addition to methylene vibrations along the alkyl chain.

4.3.2 ECD

The ECD spectrum for HHC has been previously reported in the literature. Our spectra, presented in Figure 4.5, are consistent with these previous results, with the ECD of HHC being especially weak. The measured ECD spectrum of OHC (Figure 4.6) is of a similar magnitude. This is likely due to the high conformational flexibility of these linear diarylheptanoids in addition to the ECD chromophores being located a large distance from the stereocenters of interest. The experimental EA spectra of HHC and OHC both exhibit large absorptions below 250 nm, resulting in significant noise that prevented investigation of potential ECD bands even at low concentrations. The experimental ECD spectrum for (–)-HHC only contains one asymmetric ECD band with a maximum at ∼290 nm, which has been previously reported by Itokawa et al.[113] ECD calculations using the structures optimized at the B3LYP/6-311++G(2d,2p) level resulted in ambiguity in the potential AC, as any one of the three simulated positive–negative–positive ECD bands at 320, 299, and 269 nm may be correlated with positive experimental ECD band. Repeating these ECD calculations with the long-range corrected CAM-B3LYP did not resolve this ambiguity. This motivated additional optimization and ECD calculations using the ωB97X-D functional, which is noted for its performance for excited state calculations and nonbonded interactions.[130] The predicted ECD band at 320 nm for (–)-HHC using the ωB97X-D functional well reproduces the experimental ECD band at ∼290 nm (Figure 4.5) and points to an assignment of (–)-(*R*)-HHC.

I visualized the molecular orbitals involved in this transition by applying the natural transition orbital (NTO) method[88] to the lowest energy (*R*)-HHC conformer (22% population) optimized using the ωB97X-D functional. The NTOs corresponding to this transition

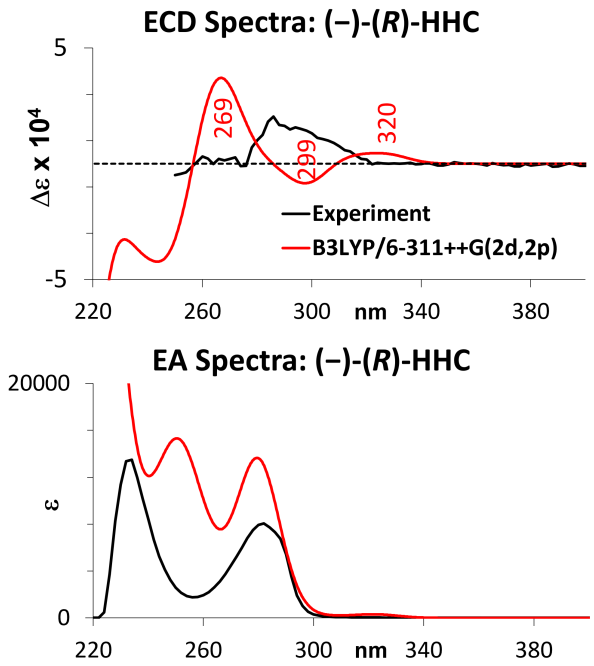

Figure 4.5: Experimental and simulated ECD and EA spectra of (–)-HHC and (*R*)-HHC

are presented in Figure 4.7, which show this band to be predominantly an aromatic π–π* transition with some antibonding contribution from the nearby carbonyl group.

The experimental and simulated ECD and EA spectra for (+)-(*R, R*)-OHC are presented in Figure 4.6. There is one weak experimental ECD band centered at 280 nm in the spectrum for OHC; this band is seen in the ECD spectra of both enantiomers with mirror image intensities. The simulated ECD spectra of (*R, R*)-OHC at the CAM-B3LYP/6-311++G(2d,2p)/PCM(MeOH) level successfully reproduced this ECD band along with the associated EA band at the same wavelength, pointing to the AC assignment (+)-(*R, R*)-OHC.

Visualization of transitions corresponding to this ECD band using the NTO method (Figure 4.8) on the lowest energy conformer (53.2% population by Gibbs energy) suggests that this band is predominately a π–π* transition on one of the phenyl rings.

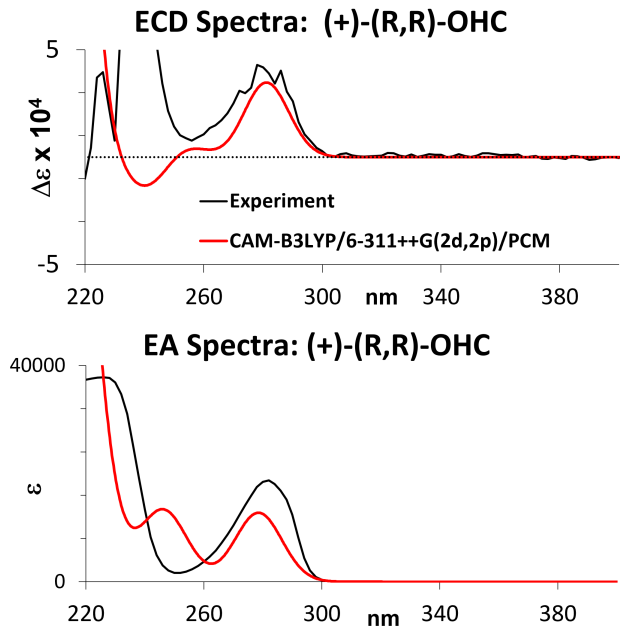

Figure 4.6: Experimental and simulated ECD and EA spectra of (+)-OHC in MeOH and of (*R, R*)-OHC

4.3.3 ORD

ORD calculations (see Figure 4.9) with the B3LYP functional for (*R*)-HHC predicted negative SOR values, as also seen in the experiment for (–)-HHC, at all wavelengths measured. The B3LYP calculation of ORD for (*R, R*)-OHC gave predicted SOR values with positive sign as are the measured SOR values for (+)-OHC. The predicted ORD signs support the assignment of (–)-(R)-HHC and (+)-(*R, R*)-OHC. The magnitudes of predicted and experimental values for (+)-(*R, R*)-OHC differ significantly. Such significant differences between predicted and experimental ORD magnitudes were noted previously for other natural products.[134–136]

4.3.4 X-Ray crystal structure of OHC

The absolute stereochemistry of OHC was determined based on the absolute structure parameter and by analysis using likelihood methods.[137] Based on the Flack parameter 0.16(8) and the Hooft parameter, 0.14(5), the (*R, R*) absolute configuration is confidently assigned

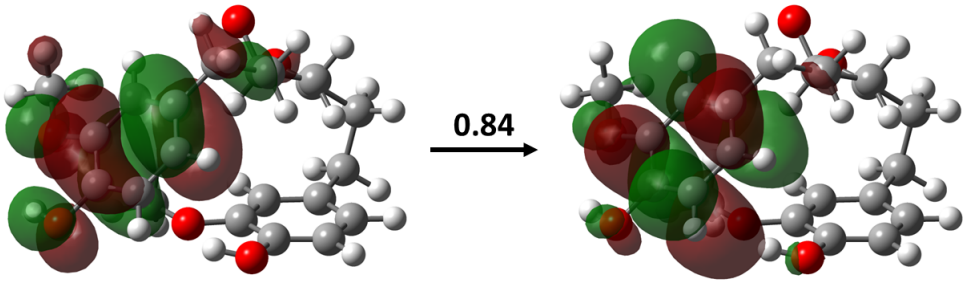

Figure 4.7: HOMO and LUMO, contributing 84%, for the 290 nm ECD band of (*R*)-HHC using the lowest-energy conformer

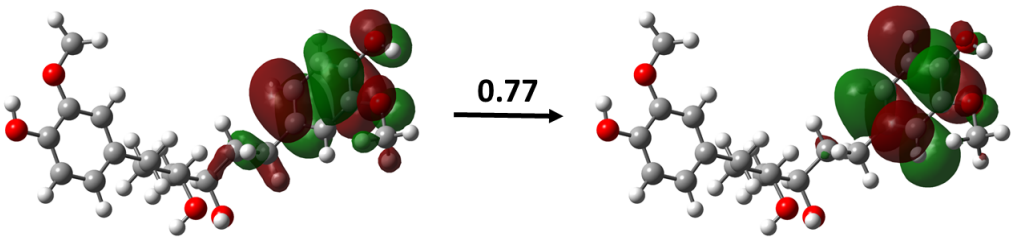

Figure 4.8: HOMO and LUMO, contributing 77%, for the 280 nm ECD band of (3*R*,5*R*)-OHC using the lowest-energy conformer

to the first eluted peak material with positive optical rotation. The structure of (*R, R*)-OHC derived from x-ray data is displayed in Figure 12.

4.4 Conclusion

VCD spectral analysis for HHC, at B3LYP/6-311++G(2d,2p) level, led to a confident conclusion for the AC assignment as (–)-(*R*)-HHC. This conclusion is independently supported by the ORD analysis at B3LYP/6-311++G(2d,2p) level and ECD analysis at ωB97X-D/def2-TZVP level. VCD spectral analysis for OHC, at B3LYP/6-311++G(2d,2p) level, suggested the AC assignment to be (+)-(*R, R*)-OHC. ECD analysis at CAM-B3LYP/6-311++G(2d,2p) level and ORD analysis at B3LYP/6-311++G(2d,2p) functional confirmed the assignment of (+)-(*R, R*)-OHC. More importantly the x-ray diffraction data for the single crystal of (+)-OHC unambiguously assigned its AC as (+)-(*R, R*). These assignments are consistent with the tenuous AC assignments previously made by correlative and exciton chirality methods.

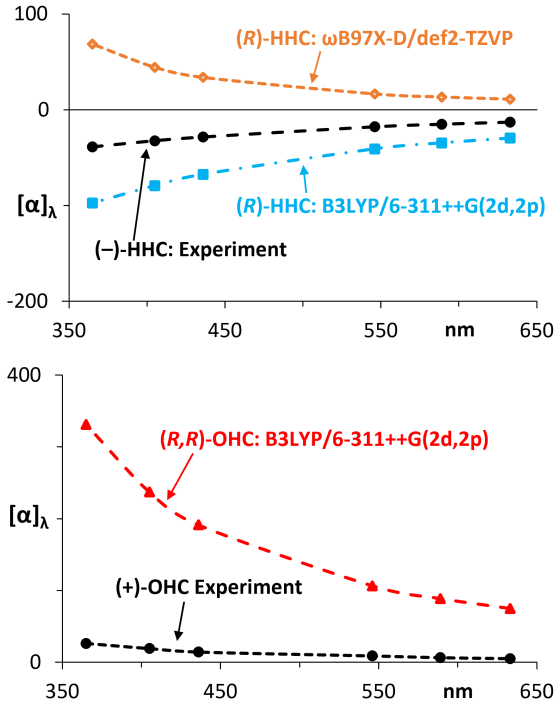

Figure 4.9: Experimental and theoretical ORD curves for (–)-HHC and (*R*)-HHC (top) and (+)-OHC and (3*R*,5*R*)-OHC (bottom)

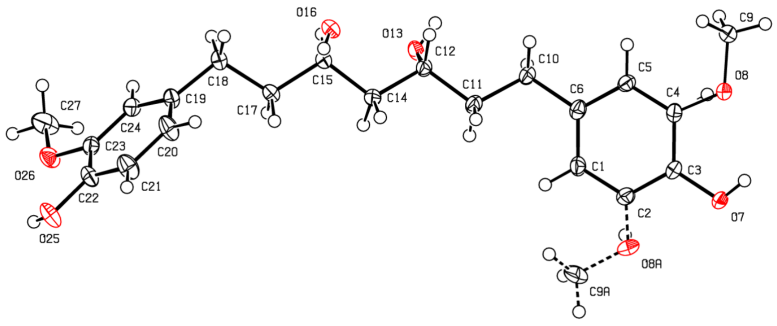

Figure 4.10: X-ray crystal diffraction data of (+)-OHC indicates (*R*, *R*)-configuration. Thermal ellipsoids are drawn with 50% probability. CCDC deposition # 2211281

CHAPTER 5

Peyssonnoside A: The Importance of f-Polarization Functions for VCD

The work from this chapter can be found in the *Symmetry* article "Revisiting the Absolute Configuration of Peyssonnoside A Using Vibrational Circular Dichroism Spectroscopy."[138] Our collaborators at the Georgia Institute of Technology isolated this natural product and performed detailed NMR measurements to elucidate as much stereochemical information as possible. Previous DFT and VCD investigations were performed by Dr. Bhuwan Khatri Chhetri who was able to assign the AC by correlations between DFT and NMR data but VCD correlations proved unreliable at the time.[139] I decided to computationally revisit this interesting compound in order to determine why VCD, a technique sensitive to stereochemistry and chirality, did not work for this compound.

5.1 Introduction

Peyssonnoside A is an unusual diterpene glycoside that is highly substituted and features a sterically encumbered cyclopropane ring within the diterpene unit.[139] The relative configuration of the diterpene unit was determined by ROESY and HSQC-ROESY NMR data, leading to two possible diastereomers for Peyssonnoside A, **1** and **2** (Figure 5.1). Evidence for the AC assignment of Peyssonnoside A was obtained by quantitative ROESY[140] data using the glycoside unit as an internal probe[141] of the stereochemistry of the attached diterpene unit.[139] Optical Rotatory Dispersion (ORD) and DFT predicted DP4+ probabilities[142] at the B3LYP/6-311++G(2d,2p) level also pointed to the AC assignment of **1**. However, VCD predictions, at the same level used for ORD and DP4+, had a poor correlation to the corresponding experimental spectra.[139] Since that report, two total syntheses of Peyssonnoside A have been reported in the literature, making it clear that this unusual molecule has captured the attention of synthetic chemists.[143,144] These studies further confirm the AC assignment made by ORD and DP4+ correlations, but since erroneous stereochemical

assignments are usually not caught until their total synthesis,[145] investigations into chiroptical methods and their reliability are worthwhile. As a recent precautionary tale, the AC of neolignan Nectamazin A was recently reassigned using VCD spectroscopy,[146] whereas the original AC assignment was made using ORD and ECD correlations.[147]

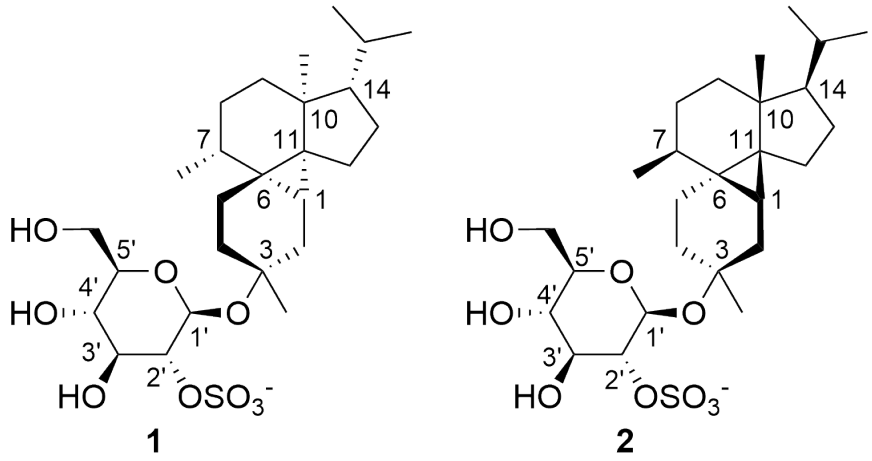

Figure 5.1: Structures of the potential diastereomers of Peyssonnoside A

One unique feature of Peyssonnoside A is the sulfonated saccharide unit. Recent work from the Merten group suggests that the S=O symmetric and antisymmetric stretches display a significant basis set dependence, resulting in red-shifted S=O stretches in the vibrational absorption (VA) and VCD spectra if f-polarization functions are not included on the sulfur atom.[148] Since previous VCD analysis[139] did not include f-polarization functions, I now investigate their influence on predicted VCD spectra of Peyssonnoside A using the B3PW91 functional.[86,149]

5.2 Methods

5.2.1 Calculations

The diastereomers **1** and **1** were both built in ChemDraw. Conformational analysis was performed in Pcmodel 10.0 (GMMX search algorithm)[150] at the molecular mechanics (MM) level with a 30 kcal/mol initial search limit with a final screening limit of 10 kcal/mol. This yielded 5573 conformers for **1** and 3939 conformers for **2**. Subsequent DFT calcu-

lations were performed in Gaussian 16.[83] The single-point energies of these conformers were computed at the B3PW91/6-31G(2d,p)[125,151] level using the SG1 integration grid. All single-point, optimization, and frequency calculations included a Polarizable Continuum Model (PCM)[128,129] representing the DMSO-d_6 solvent used for VCD measurements. The geometries within the lowest 5.0 kcal/mol limit based on the computed single-point energies were then optimized at the same level using the default UltraFine integration grid, which was used thereafter. VCD and ORD calculations were performed on optimized structures in the lowest 2.0 kcal/mol window based on electronic energies at the B3PW91/6-31G(2d,p)/PCM level. The optimized geometries within the lowest 3.0 kcal/mol based on Gibbs energies at the B3PW91/6-31G(2d,p)/PCM level were further optimized at the B3PW91/6-311G(3df,2pd)[123,126,127]/PCM level, and VCD calculations were performed thereafter for conformers in the lowest 2.0 kcal/mol based on electronic energies. A 3.0 kcal/mol limit was chosen due to the lower computed energy difference between conformers at the B3PW91/6-311G(3df,2pd)/PCM level relative to the B3PW91/6-31G(2d,p)/PCM level. In addition to our new calculations on diastereomers **1** and **2**, I also analyze the VCD spectra that were reported previously at B3LYP/6-311++G(2d,2p) level.[139]

All spectral simulations and similarity analyses[132,152] were undertaken using the in-house developed CDSpecTech program.[84] The numerical measures of quantitative similarities for VA, VCD and vibrational dissymmetry factor (VDF) spectra were assessed respectively from SimVA, SimVCD and SimVDF functions.[132,152] The SimVA and SimVDF values reported here are at the same scale factor that gives maximum SimVCD. Similarity analysis was performed between calculated and experimental spectra using the experimental 1100 to 1490 cm^{-1} region.

Additional optimizations and VCD spectral predictions are also undertaken on fragments of the lowest energy conformers for **1** at the B3PW91/6-311G(3df,2pd) level whereby the separate diterpene and saccharide units were cleaved at the glycosidic linkage and capped with an $-OC^3H_3$ group. ^3H isotope was used in place of ^1H to avoid interfering

vibrations from –C–^{1}H vibrations of the capping group. VCD calculations were performed on the unique diterpene and saccharide optimized geometries.

All molecular visualizations were made with CYLview.[153]

5.2.2 Experimental

Optical rotations of Peyssonnoside A were measured in DMSO at a concentration of 12 mg/ml in 1 cm pathlength cuvette using A Jasco J-815 instrument.[139] VCD measurements were carried out using a commercial Chiral IR instrument using a fixed pathlength (100 μm) SL3 cell at a concentration of 80 mg/mL using DMSO-d_6 as solvent.[139]

5.3 Results and Discussion

Given the size of the ensembles of **1** and **2**, as well as the large number of atoms, I initially elected to rank the MM geometries based on DFT single-point energies at the B3PW91/6-31G(2d,p)/PCM level and optimize only those within a 2.5 kcal/mol limit. This is the recommendation of Ruud and coworkers for cyclic oligopeptides[22] and seems to work well for locating the low-energy conformers of very flexible molecules.[154] The 6-31G(2d,p) basis set was used as a reasonable compromise between the 6-31G(d) basis and those that include multiple diffuse and polarization functions, which appeared to be very computationally expensive for this large molecule, while still having polarization functions included in its definition. Additionally, the Merten group has shown that good VCD agreement can be obtained with this basis set for dipeptides, which are very flexible molecules with several conformers.[155] I explored the use of the semi-empirical PM6[156] method for pre-optimization prior to DFT single-point ranking, but single-point energies after PM6 optimization were several kcal/mol higher than the single-point energies of the MM geometries, so I avoided the use of the PM6 method.

Optimizations of **1** and **2** at the B3PW91/6-31G(2d,p) level gave a total of 11 conformers for **1** and 10 conformers for **2** within a 2.0 kcal/mol window, which is a small number of conformers similar to the low number of low-energy conformations obtained previously

(five for each diastereomer).[139] It is likely that the diterpene unit at the anomeric carbon prevents the otherwise flexible sugar moiety from puckering, thereby limiting the ring to one favorable chair position. Additionally, the C-3 alcohol group is pointing towards one of the oxygens in the C-2 sulfate group, locking both into place and further limiting the number of obtained conformers due to this favorable intermolecular interaction. This oxygen also has a shorter S=O bond length, likely due to the stabilizing hydrogen bonding interaction from the C-3 hydroxyl group.

5.3.1 VCD

The simulated VCD spectra of **1** and **2** at the B3LYP/6-311++G(2d,2p)/PCM level were previously found to have a poor correlation to the corresponding experimental VCD spectrum and therefore AC could not be determined in that study.[139] These previously predicted spectra of **1** and **2** are compared with corresponding experimental spectra in Figure 5.2 and quantitative similarities are reported in Table 5.1. The choice of frequency scale factor for predicted spectra at B3LYP/6-311++G(2d,2p)/PCM level is not trivial, as the quantitative Sim values are very low. If the S=O vibrations, which are clearly mispredicted, are ignored then a scale factor of 0.967 appears to be appropriate based on correlation with the weak VA bands at 1460 and 1370 cm^{-1}. For diastereomers **1** and **2** at this level of theory, quantitative analysis of the maximum SimVCD gives two distinct scale factors: 1.035 for **1** and 0.981 for **2**. Owing to the conflicting observations, I presented the simulated spectra in Figure 5.2 with one frequency scale factor of 1.000. The quantitative similarities between predicted and experimental spectra are quite low for both diastereomers (see Table 5.1) and this was the reason for not being able to assign the AC of Peyssonnoside A from VCD spectra previously. This negative conclusion motivated us to explore different levels of theory for VCD predictions.

Simulated spectra of **1** and **2** at the B3PW91/6-31G(2d,p) level and comparison with experimental spectra are presented in Figure 5.3. The predominant difference in the two

Table 5.1: Quantitative similarities for Peyssonnoside A at the chosen levels of theory

B3LYP/6-311++G(2d, 2p)				
Compared Spectra	σ	**SimVA**	**MaxSimVCD**	**SimVDF**
1 and Exp.	1.035	0.62	+0.30	+0.27
2 and Exp.	0.981	0.40	+0.14	+0.23
B3PW91/6-31G(2d,2p)/PCM				
1 and Exp.	0.980	0.54	+0.47	+0.42
2 and Exp.	0.989	0.70	+0.24	–0.01
B3PW91/6-311G(3df,2pd)/PCM				
1 and Exp.	0.981	0.94	+0.76	+0.67
2 and Exp.	0.980	0.94	+0.27	+0.06

predicted spectra is that the positive experimental VCD bands at 1344, 1321, and 1298 cm^{-1} are all predicted to be negative for **2** and the band shape of the positive experimental 1177 cm^{-1} band is better reproduced by **1**. Quantitative similarities between predicted and experimental spectra, which are presented in Table **1**, show the maximum SimVCD and corresponding SimVDF for **1** to be greater than 0.4, but are less than 0.25 for **2**, pointing towards AC assignment of Peyssonnoside A as that of **1**. However, the SimVA of 0.54 for diastereomer **1** at the scale factor of 0.980 used in Figure 5.3, is not a high enough value, unlike those normally found for VA spectra. Visualization of the vibrations in the simulated spectra shows that the simulated VA bands at 1253 and 1178 cm^{-1}, as well as the corresponding VCD bands, have significant contributions from S=O symmetric and antisymmetric stretches, and these bands did not line up with experimental bands due to their red-shifted positions. These mispredicted S=O stretches have little impact on the VDF spectra, due to the high associated VA intensities.

Noting the poor agreement between the experimental and simulated VA spectra of **1** and **2** at the previous levels of theory, I hoped that f-polarization functions might improve the predictions. However, the size of **1** and **2** makes the use of a larger basis set very expensive, even with relatively few conformers. Despite this, I further optimized the low-energy conformers of B3PW91/6-31G(2d,p) level (11 for **1** and 10 for **2**) at the B3PW91/6-

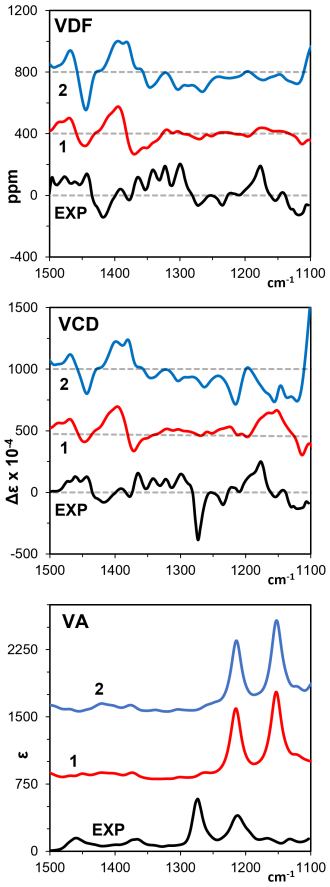

Figure 5.2: VDF, VCD, and VA of **1** and **2** using the B3LYP functional with the 6-311++G(2d,2p) basis set

311G(3df,2dp)/PCM level. The relative energies of the conformers dropped significantly, so I expanded the energy window of conformers to be optimized at the higher level of theory to be those within 3.0 kcal/mol from the B3PW91/6-31(2d,p)/PCM level. Additionally, I also optimized conformers whose single-point energies at the B3PW91/6-31(2d,p) level were within a 5.0 kcal/mol limit, so as to ensure that no conformers were missed. Ultimately, this process gave two additional conformations within 2.0 kcal/mol for both diastereomers **1** and **2**, for a total of 13 conformers for **1** and 12 for **2** at the B3PW91/6-311(3df,2pd) level.

A comparison of spectra simulated at the B3PW91/6-311G(3df,2pd) level to the experimental spectra of Peyssonnoside A is presented in Figure 5.4 The simulated VDF and VCD

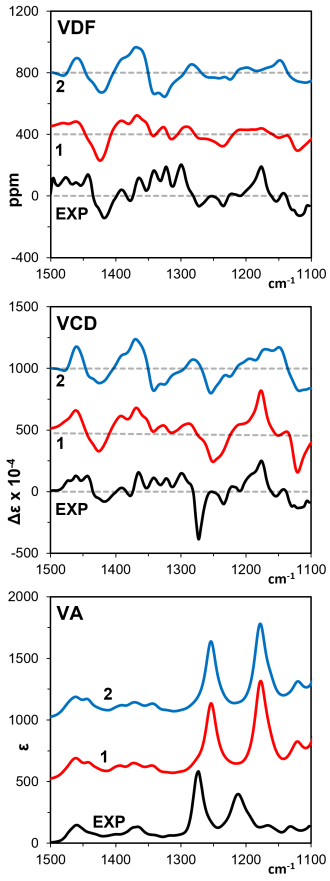

Figure 5.3: VDF, VCD, and VA of **1** and **2** using the B3PW91 functional with the 6-31G(2d,p) basis set

spectra have been multiplied by 2 for better comparison with the experimental spectra. The B3PW91/6-311G(3df,2pd) predicted S=O VA and VCD bands at 1275 and 1207 cm^{-1} are now in line with corresponding experimental bands. The addition of f-polarization functions gives a substantial improvement in the quantitative similarity of simulated spectra of **1** with the corresponding experimental spectra (see Table 5.1). The similarity values of SimVA (0.94), SimVCD (0.76) and SimVCD (0.67) for **1** are among the highest similarity values seen in the literature, giving high confidence for **1** as the AC of Peyssonnoside A.

Given that much of the VCD appears to arise from the sulfonated saccharide instead of the rigid diterpene unit, I set out to investigate the VCD activities of the respective fragments. Normally, VCD contributions from individual parts of a molecule do not necessar-

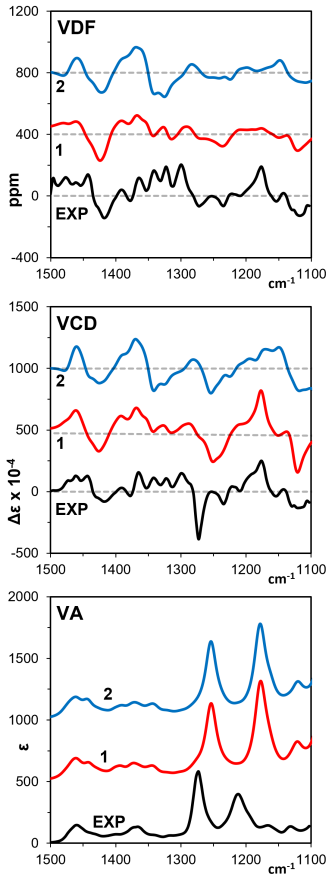

Figure 5.4: VDF, VCD, and VA of **1** and **2** using the B3PW91 functional with the 6-311G(3df,2pd) basis set

ily add up to the VCD spectrum of the entire molecule. However, because of the different bond types in the diterpene and sugar units, I decided to check if VCD calculations of the individual fragments may be a good approximation of the overall VCD spectrum.

One sugar and one diterpene fragment for each of the thirteen conformations of diastereomer **1** were used as the starting point. After optimization of these geometries at the B3PW91/6-311G(3df,2pd) level, there were seven unique sugar fragments and two unique diterpene fragments. VCD calculations were performed on these optimized geometries. The VCD spectra of **1** and its optimized fragments are presented in Figure 5.6.

VCD contributions from the diterpene fragment are much weaker than those of the sulfonated sugar. However, from visual inspection, there are six bands that can be identified

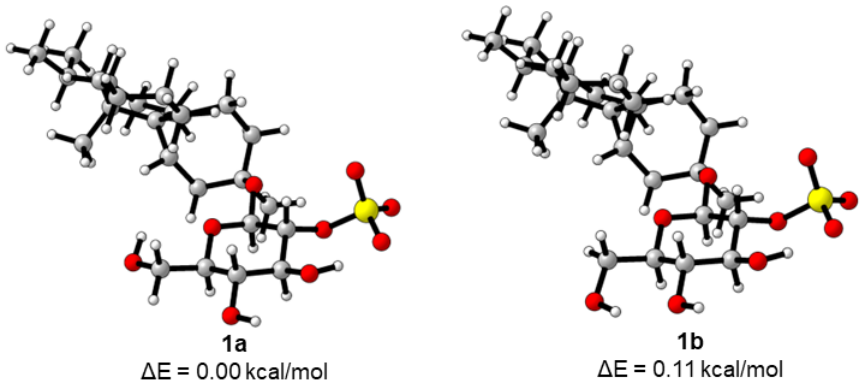

Figure 5.5: The two lowest energy conformers of **1**

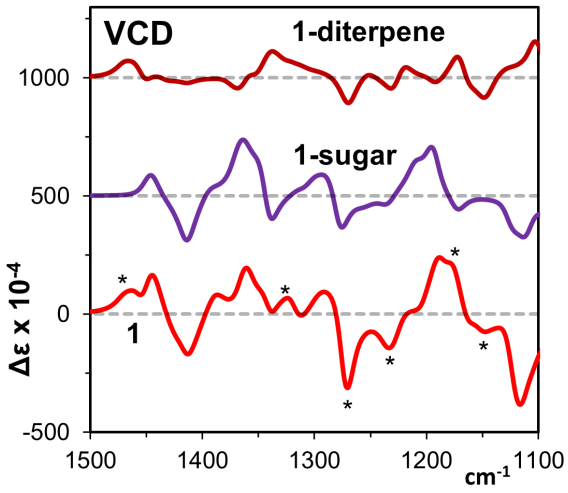

Figure 5.6: VCD of **1** and its sugar and diterpene fragments

to originate from the diterpene fragment, and these bands are marked with an asterisk (*) in Figure 5. These bands are (1) a shoulder at 1464 cm^{-1}, (2) a weak (+)-band at 1325 cm^{-1}, (3) the S=O antisymmetric (1270 cm^{-1}) band, (4). the S=O symmetric (1234 cm^{-1}) band, (5) a shoulder (+)-band at 1178 cm^{-1}, and (6) a weak (–)-band at 1148 cm^{-1}. These bands in **1** each have a corresponding band in the experimental VCD spectrum, and these bands are either of smaller magnitude or opposite signs in the predicted spectrum of 2, indicating that these bands are sensitive to the stereochemistry of the rigid diterpene fragment. Overall, the sum of VCD spectra of diterpene and sugar fragments appears to be a reasonably good approximation to the VCD spectrum of the whole molecule.

5.3.2 ORD

The good agreement between experimental and predicted ORD curves were one of the key pieces of evidence for the AC assignment of Peyssonnoside A,[139] so it is important that the ORD of **1** and **2** also be computed at the same level that gives satisfactory VCD agreement as additional evidence of the AC of Peyssonnoside A. Predicted ORD curves for both **1** and **2** at B3PW91/6-31G(2d,p) and B3PW91/6-311G(3df,2pd) levels are displayed in Figure 5.5. At both levels, the Boltzmann conformer averaged predicted ORD curves of **1** are all negative and are all positive for the conformers of **2**. Despite being diastereomers, the ORD curves for **1** and **2** are almost mirror images. These mirror-image curves suggest that ORD is more sensitive to the stereochemistry of the diterpene fragment, as opposed to the saccharide fragment. The current ORD data support the AC assignment of **1**, as reported previously.[139]

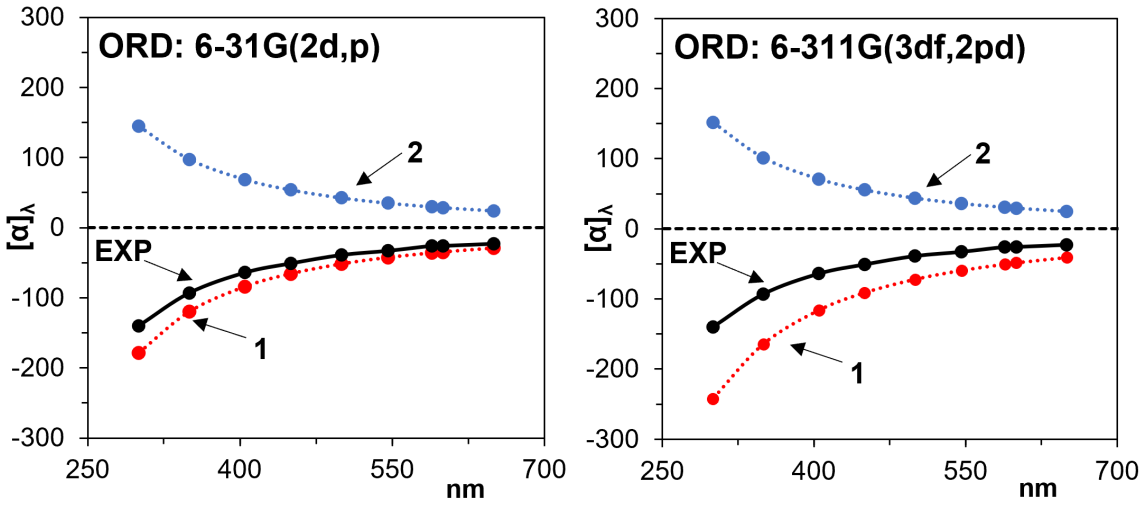

Figure 5.7: ORD of **1** and **2**

5.4 Conclusion

Previously reported VCD analysis at the B3LYP/6-311++G(2d,2p) level was unable to establish the AC of Peyssonnoside A. On the contrary, the current VCD analysis at B3PW91/6-311G(3df,2pd) level has provided a convincing AC assignment. This stark contrast between

the two calculations is attributed to the inclusion of f-functions in the basis set.

Overall, the large size of Peyssonnoside A makes an accurate computation of VCD frequencies to be challenging. Despite its unusual structure, the dominant VCD activity for **1** and **2** arises from the monosaccharide unit instead of the rigid diterpene unit. Calculations at a higher level of theory, including f-polarization functions increase the similarity between **1** and the experimental spectra. However, similarities at a more cost-effective, double-ζ basis set also point towards an AC assignment of **1**, despite low VA similarities arising from characteristic red-shifting of S=O stretching vibrations. Contrary to VCD, ORD is sensitive to the stereogenic centers of diterpene fragments. Therefore, the ORD and VCD spectroscopies are sensitive to separate stereogenic fragments of Peyssonnoside A, highlighting the importance of the use of multiple chiroptical spectroscopies in the stereochemical analysis of complex natural product molecules.

CHAPTER 6

Influence of Microsolvation on VCD in DMSO Solvent

The work in this chapter can be found in the *Spectrochimica Acta Part A: Biomolecular and Molecular Spectroscopy* article "Influence of microsolvation on vibrational circular dichroism spectra in dimethyl sulfoxide solvent: A Bottom-Up approach using Quantum cluster growth".[157] This work was made possible by both novel computational methods produced by the Grimme lab in Germany and the many VCD spectroscopists who performed and reported studies in DMSO, a frustrating solvent for such measurements.

6.1 Introduction

One common issue in molecular structure determination is self-aggregation, or the formation of dimers and other supramolecular complexes, which is very common with molecules possessing carboxylic acids, alcohols, or other groups capable of forming favorable intermolecular hydrogen bonds. There are several methods in the literature for avoiding this issue experimentally, such as synthesizing acetylated or sodium salt derivatives,[136,158] which require additional workup and characterization before chiroptical measurements. More recently, the Merten group reported that the addition of 7-azaindole is enough to prevent the aggregation of carboxylic acids.[159]

Common implicit solvation models,[128] such as the Conductor-like Screening model (COSMO),[160], the Polarizable Continuum Model (PCM),[129] or Truhlar's universal SMD model[161] can account for essential long-range interactions the solute forms with the surrounding solvent. For many non-hydrogen bonding solvents, such as chloroform or carbon disulfide, an implicit solvation model, such as PCM, is a cost-effective treatment of solvent effects and can provide sufficiently accurate energies and conformations for the confident interpretation of VCD spectra. These approaches are popular for their computational tractability but do not take into consideration explicit intermolecular interactions.

For solvents that form strong hydrogen bonding interactions with the solute (such as water, acetonitrile, dimethyl sulfoxide (DMSO), or methanol), traditional approaches with implicit solvent models usually do not adequately describe the intermolecular hydrogen bonding effects between solute and solvent. Additionally, certain hydrogen-bonding solvents can form bifurcated hydrogen bonds (DMSO for example) and form hydrogen-bonding networks (water for example), which further complicate conformational analysis because multiple solvent molecules and their orientations must be considered in the molecular model. For a more accurate treatment for hydrogen-bonding solvents, it is necessary to include solvent molecules in the QC model, otherwise termed an "explicit solvent" approach. Explicit solvation, whereby short-range intermolecular interactions are incorporated into the model, requires the use of solvent-solute clusters. These clusters can be obtained in several ways, most commonly by performing molecular dynamics (MD) simulations in a solvent bath and analyzing the MD snapshots, using radial distribution functions (RDFs), to empirically determine how many solvent molecules are necessary for further analysis. Commonly, these snapshots will be pruned down to desired solvent-solute clusters for QC calculations. It is also possible to extract further information from MD simulations, such as probable solvent positions, orientations, and other interaction parameters using Grid Inhomogeneous Solvation Theory (GIST) or similar methodologies.[162] I refer to the MD approaches as "top-down", which have the advantage that the number of interacting solvent molecules arises naturally from simulations but require the full initial consideration of the solvent bath.

Explicit solvent modeling is complicated for several reasons, namely (a) the generation and sampling of low-energy solute-solvent interactions is not trivial, (b) the number of solvent molecules necessary for good agreement between VCD experiment and calculations is unknown a priori,[163] and (c) QM modeling of solvent molecules increases the computational cost and leads to difficulties in SCF convergence.

One could use ab initio MD (AIMD) approaches[164,165] to compute the VCD and VROA

spectra in solution, but AIMD calculations can be computationally demanding. One could also treat the solute and neighboring solvent molecules at the QM level and the remainder of the solvent molecules at a molecular mechanics (MM) level, termed QM/MM, which is usually accomplished through an ONIOM model.[166] In these QM/MM simulations, it is also possible to represent the solvent molecules at the MM level as fluctuating charges (FQ), termed the QM/FQ/MM approach by Cappelli and coworkers.[167]

Most of the above-mentioned top-down approaches were applied for calculating VCD and VROA spectra in water solvent. Somewhere between the implicit solvent and full AIMD approaches lies microsolvation, termed by Luber and Rieher for VROA calculations of 1,6-anhydro-β-D-glucopyranose in water,[168] where three water molecules were included to form solute-solvent clusters, and these microsolvated clusters were embedded in water solvent using COSMO. More details on microsolvation can be found in a review by Xu and coworkers.[24]

Only a limited number of applications of the abovementioned top-down and microsolvation approaches have appeared for other hydrogen bonding solvents. The combination of AIMD and NVP, referred to as first principles molecular dynamics (FPMD), was applied by Zehnacker and coworkers[169] for predicting the VCD spectra of 1-indanol in DMSO solvent. Explicit solvation calculations using QM/MM with a full solvent box were reported for pantolactone in DMSO by Longhi and coworkers.[170] Some microsolvation investigations used manually generated solute-solvent clusters to model essential intermolecular interactions in DMSO and acetonitrile, typically using gas-phase equilibrium geometries as input, especially early on when more advanced approaches were not computationally tractable for routine chiroptical studies.[7,8,171–173] A systematic and automated evaluation of the conformational landscape for solvent-solute clusters with these solvents remains a challenge.

In some situations, even static calculations with coordinated solvent molecules may not provide good agreement with experimental VCD spectra, and additional sampling using

linear transit calculations suggested by Nicu and coworkers,[174] may provide better agreement. It should also be noted that even in hydrogen-bonding solvents such as methanol and acetonitrile, explicit solvation calculations are not always necessary to obtain good agreement, despite strong solute-solvent interactions.[132,163] This is evidenced especially for larger molecules with few hydrogen-bonding groups, where the number of VCD-active bands that are uninfluenced by solvent-solute interactions far outnumber the heavily affected bands, and thus the latter appear more muted in the overall spectrum.[163]

This article investigates an automated bottom-up approach for microsolvation in VCD spectra in dimethyl sulfoxide solvent and explores its applicability and limitations. For this purpose, I evaluate the applicability of the recently developed Quantum Cluster Growth (QCG)[175] utility in the conformer–rotamer ensemble sampling tool (CREST)[176] program of xTB[177] as a resource for investigating explicit solvent effect in simulated VCD spectra. Although the CREST program itself has been used in the past for generating various possible conformers for VCD calculations,[22,178] I am not aware of studies using QCG for VCD studies in DMSO solvent. While this manuscript was under preparation, an application of QCG for the VCD spectra of β-D-glucopyranose in water[179] was reported by Xu and coworkers. The QCG utility can automatically generate solute-solvent clusters and conformational ensembles of the microsolvated clusters through metadynamics (MTD) simulations.[180] Several other programs can generate microsolvated clusters, such as ABCluster[181] and AutoSolvate,[182] but I were impressed with the initial performance and ease of use of the QCG utility and have chosen to focus our efforts on its application. I focus our efforts on molecules (Figure 1) whose experimental VCD spectra have been reported before and some of them have been previously studied via modeling in explicit DMSO, allowing us to compare the current approach to previous studies. The microsolvated clusters generated in this work are also embedded in DMSO solvent using implicit solvation, as was done for water solvent by others.[24,168,183]

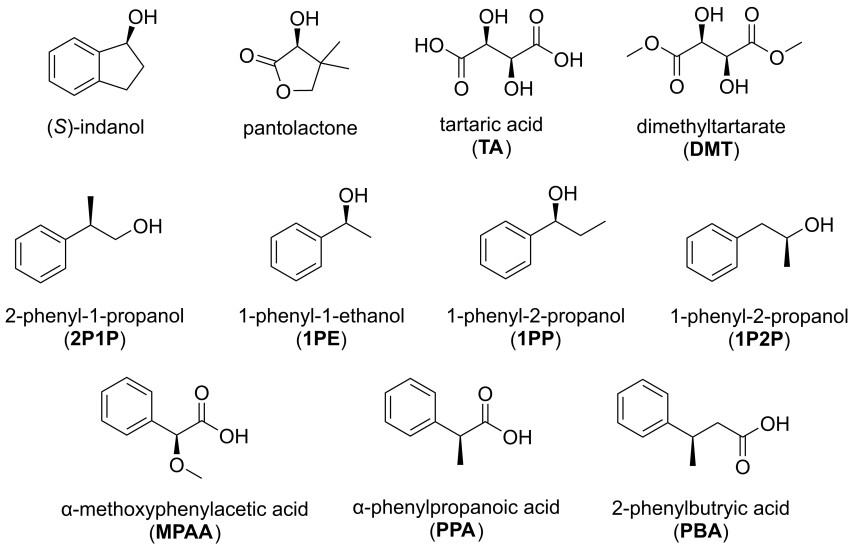

Figure 6.1: Structures of the molecules in this DMSO microsolvation study.

6.2 Methods

I performed all solute–DMSO conformational searches with the QCG utility implemented in the CREST program. To ensure that as many conformations were sampled as possible, I performed as many as ten independent runs with a longer-than-usual metadynamics length of 100 ps. For tartaric acid (TA) and dimethyl tartrate (DMT), additions of solvent molecules were performed incrementally (vide infra). QCG runs for other solute molecules (Figure 6.1) were specified to use one solvent molecule. The resulting ensembles were combined and screened for the lowest energy clusters in a 6 kcal/mol window using the GFN2-xTB method.[184] The analytical linearized Poisson–Boltzmann (ALPB) implicit solvent model[185] was utilized in both the QCG runs and subsequent conformational screening. The generated clusters were screened using a script that checks for hydrogen bonding between the DMSO solvent and solute molecule. These clusters were also manually inspected during calculations to ensure that only hydrogen-bonded clusters were used for VCD analysis.

Initial benchmarking was performed on the QCG generated ensembles of 1-indanol (IND)–DMSO clusters optimized with several functionals, namely B3LYP, B3PW91, M06-

2X, and ωB97X-D functional using the 6-311++G(2d,2p) basis set and with PCM in Gaussian 16[83] for representing the DMSO solvent. The geometries were then filtered by Root mean square deviation (RMSD) and VCD calculations were performed on the unique geometries. Additional linear transit (LT) calculations were performed on the ωB97X-D optimized geometries to sample C–O–H bending motion and O–H rotatory motion about the C–O axis, as described by Xia et al.[174] Due to many low-energy conformations, only 7 steps of 1° were taken in both directions of the bending motion, and six steps of 5° for rotatory motion, and produced geometries with electronic energies $\sim$0.7 kcal/mol higher than the parent geometries. Vibrations and VCD activities were predicted as with the low-energy conformers, except that the imaginary mode resulting from the PES scan was projected out, and the spectra were simulated using the low-energy conformers and the resulting LT scan geometries.

Experimental VCD spectra for L– and D–tartaric acid were measured in DMSO-d_0 on a commercial Chiral IR instrument using a sample cell with a fixed 100 μm path length. QCG ensemble generation was performed incrementally from one to five solvent molecules for tartaric acid (TA). Full DFT treatment of the TA:DMSO complexes were only truly tractable for complexes with one to four DMSO molecules and optimizations were performed at the ωB97X-D/6-31G** and subsequently ωB97X-D/6-311++G(2d,2p) levels with PCM representing the DMSO solvent.

Microsolvation calculations for pantolactone (PAN), 1-phenyl ethanol (1PE), 1-phenyl-2-propanol (1P2P), 1-phenyl propanol (1PP), and 2-phenyl-1-propanol (2P1P), were carried out as with indanol, except calculations were performed at the ωB97X-D/6-31G** and subsequently ωB97X-D/6-311++G(2d,2p) levels with PCM representing the DMSO solvent due to the size of the generated ensembles. All VCD calculations were performed using DMSO-d_6 (except for TA where DMSO-d_0 was used) to match the experimental spectra and the populations of the individual solute-solvent complexes were derived from respective Gibbs energies at 298 K.

Experimental spectra in DMSO-d_6 for PAN,[170] DMT,[171] 1PE, 1PP, 1P2P, 2P1P,[9] and IND[169] were digitized from the literature using WebPlotDigitizer.[186] Interpolation was used to preserve the quality of the spectra. The quantitative measures for agreement between experimental and predicted VA, VCD, and vibrational dissymmetry factor (VDF) spectra are obtained using the similarity indices SimVA, SimVCD, and SimVDF, as previously described.[132] The range for SimVA values is from 0 to 1, while that for SimVCD and SimVDF is from –1 to +1, with negative values indicating similarity for the VCD spectra of opposite enantiomer. A minimum magnitude of 0.40 for SimVCD and SimVDF is recommended to reliably assign the AC.

6.3 Results and Discussion

The reported experimental VA spectra are usually presented as solvent-subtracted. The experimental VCD spectra are presented either as solvent-subtracted or opposite enantiomer-subtracted, to obtain a flat zero-VCD line. For this reason, the DMSO solvent contribution will not normally be visible in the experimental vibrational absorption (VA) and VCD spectra. The induced chirality in the solvent may show up in the experimental VCD spectra, but the limited spectral region studied in DMSO solvents generally does not reveal such effects. I should add that previous work by the Merten group suggests that the S=O stretching frequency in organic molecules containing S=O is characteristically sensitive to the inclusion of higher-order polarization functions in the basis set method.[148] In an attempt to avoid dealing with this issue for DMSO, I tried setting the masses of the DMSO atoms to an arbitrarily large number of 100 amu to isolate VCD and VA response from solute and remove any possible interferences from mispredicted S=O stretching frequencies between methods that may affect the solute bands via vibrational coupling. This type of heavy mass substitution has been performed before in microsolvation studies of methyl lactate, whereby the strong coupling between the vibrational modes of water and methyl lactate was avoided by setting the masses of the atoms in the water molecule to 400 amu.[187] Comparison to VCD

calculations using DMSO-d_6 and DMSO-100 (all solvent atom masses set to 100 amu) did not show any significant deviations in the simulated VCD spectra within the narrow DMSO-d_6 window of 1100 to 1800 cm^{-1} when considering appropriate frequency scaling factors. The artificial nature of Gibbs energies obtained in DMSO-100 calculations did not allow us to do Gibbs energy weighting for spectral simulations, so herein I present only the spectra modeled with DMSO-d_6.

For visualization of geometries, I denote interaction lines to indicate hydrogen bonding between DMSO and -OH or -COOH groups as well as weak secondary hydrogen bonding between the methyl groups in DMSO and C=O or -OH groups. This secondary hydrogen bonding is very weak (¡ 4 kcal/mol)[188] and it is not clear from experimental evidence if this interaction is long-lived enough to be significant in the "clusters-in-a-liquid" or similar approaches. Other weak hydrogen bonds such as C-H...π interactions are left unlabeled. Nevertheless, I find this description helpful in describing bifurcation, or the association of DMSO to two separate sites in the solute, which has been previously noted in the literature for DMSO.[7] The typical $CH_3 \ldots$ O=C interaction is in the range of 2.4–2.6 $\AA$, with a few as long as 3.1 $\AA$ due to steric hindrance. The typical lengths of -OH$\ldots$O=S interactions are $\sim$1.7 $\AA$, and -COOH$\ldots$O=S interactions are $\approx$1.55 $\AA$.

6.3.1 Pantolactone

The simulated and digitized experimental VA and VCD spectra for pantolactone are presented in Figure 2, where the predicted spectra are simulated with PAN:1DMSO geometries optimized at the ωB97XD/6-311++G(2d,2p)/PCM(DMSO) level. The agreement between the simulated and experimental spectra is very good, with SimVA being 0.85, the SimVCD as +0.69, and SimVDF as +0.66, which are well above the +0.40 threshold often used for AC determination.41 The previously reported explicit solvation calculations on PAN in DMSO by Longhi and coworkers used QM/MM with full solvent box and QM/MM with a 4 $\AA$ solvent shell with six to eight DMSO molecules.34 No quantitative similarity

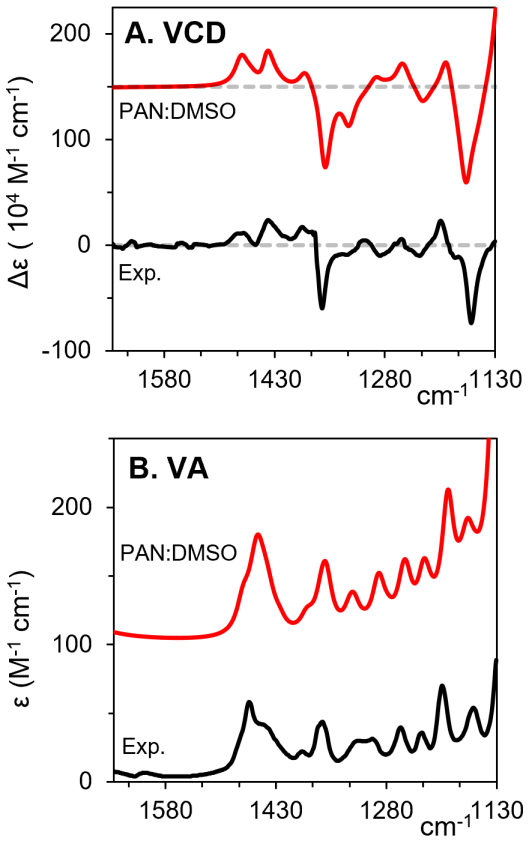

Figure 6.2: VCD and VA spectra of (*R*)-pantolactone in DMSO.

analysis was performed, but qualitatively the QCG generated microsolvated clusters in the current work better reproduce the spectra with only the added cost of one DMSO molecule in the ensemble generation. The lowest energy geometries of 14 microsolvated clusters of PAN:1DMSO, along with their Gibbs energy-derived populations, are presented in Figure 3. Note that DMSO can be seen to be located, both above the plane of the pantolactone ring and away from it.

6.3.2 Tartaric Acid

The simulated and experimental VCD and VA spectra for ((*S*,*S*))-TA in DMSO-d_0 are presented in Fig. 6.4. I used a uniform scale factor of 0.970 to scale the predicted frequencies for all simulated spectra of TA. Due to the small solvent window available in undeuterated DMSO and the relatively few bands present, I avoid emphasizing quantitative analyses to

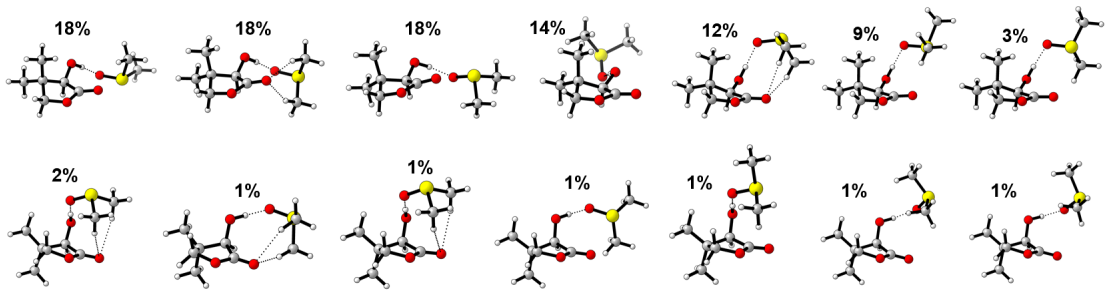

Figure 6.3: Lowest energy structures of (*R*)-pantolactone with one explicit DMSO molecule.

describe the agreement between experimental and simulated spectra.

Three different types of cluster ensembles are identified, depending on the number of DMSO molecules used for microsolvation. The lowest energy conformer of TA:1DMSO clusters has hydrogen bonding between one COOH group and DMSO, instead of either of the chiral –OH groups, indicating the necessity of including more DMSO molecules in the sampling for solvation of the chiral alcohol groups. Filtering for TA:1DMSO clusters where DMSO coordinates to either or both chiral alcohol groups is possible but is not presented herein to avoid biasing against the low-energy COOH…DMSO conformations.

QCG calculations with four DMSO molecules yielded many clusters similar to those in the TA:3DMSO ensemble with an extra, uncoordinated DMSO. This could be due to the combination of the RMSD biasing potential and wall potentials used in the metadynamics generation of cluster geometries. QCG-generated TA:4DMSO geometries that were fully coordinated or semi-coordinated were roughly equal in energy, with 144 semi-coordinated clusters and 266 fully coordinated clusters after manual filtering. Calculations using the TA:4DMSO ensemble do not appear to improve VCD predictions (see Fig. 6.4) and thus only the geometries and their Gibbs energy-derived populations for the 20 lowest energy TA:3DMSO structures are presented in Fig. 6.5.

There are three predominant features in the experimental VCD spectrum, a (+)-band at 1203 cm^{-1}, a (–)-band at 1138 cm^{-1}, and a (+)-band at 1088 cm^{-1}, all three of which

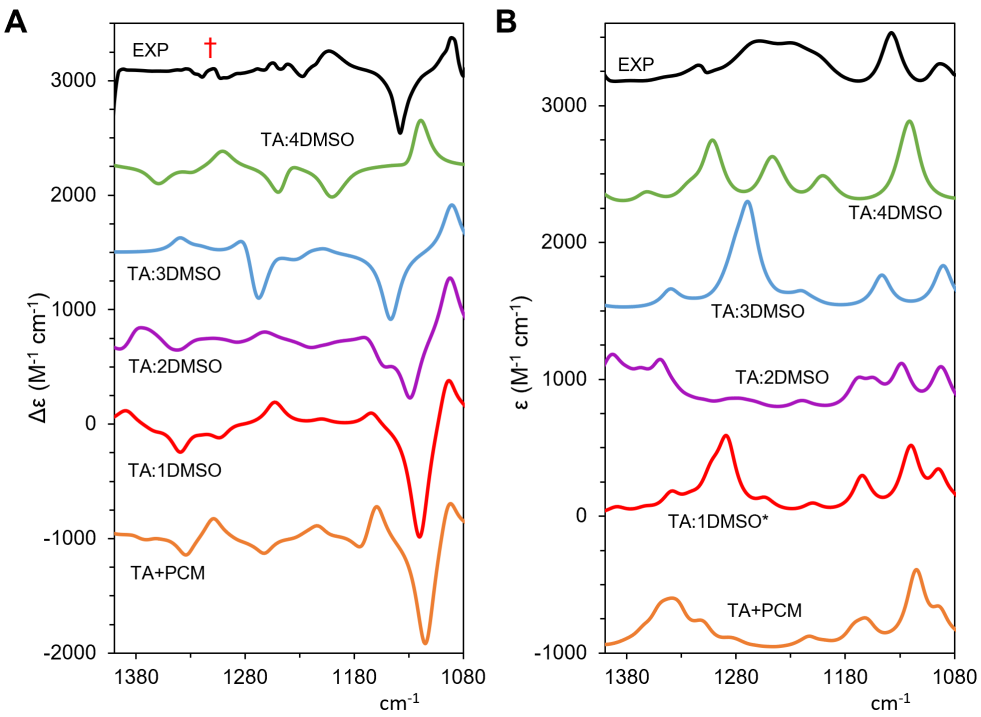

Figure 6.4: VCD and VA spectra of (S,S)-Tartaric Acid with 0–4 explicit DMSO molecules.

have been reported previously for tartaric acid in both DMSO-d_0 and -d_6.[189] The experimental bands at 1138 and 1088 cm^{-1} are reproduced for low energy conformer of each of the three cluster ensembles, and correspond to symmetric and antisymmetric O–C–C–O vibrations, respectively, at the chiral centers. The experimental (+)-band at 1088 cm^{-1} was predicted at relatively the same frequency whilst the experimental (–)-band at 1138 cm^{-1} was predicted with blueshifts as more explicit DMSO molecules are present. The corresponding predicted (–)-band is closest to the experiment for the lowest energy conformer of TA:2DMSO and TA:3DMSO cluster ensembles, although appearing 10 cm^{-1} above and below, respectively, the experimental frequency of 1138 cm^{-1}. Visual inspection of the O–C–C–O stretching modes suggests that the frequency shift of the symmetric stretch (corresponding to (–)-VCD band) may in part be due to vibrational contributions from –COOH moieties that do not have a bound DMSO molecule, as the 1DMSO and 2DMSO clusters have strong contributions from uncoordinated –COOH groups. The low-

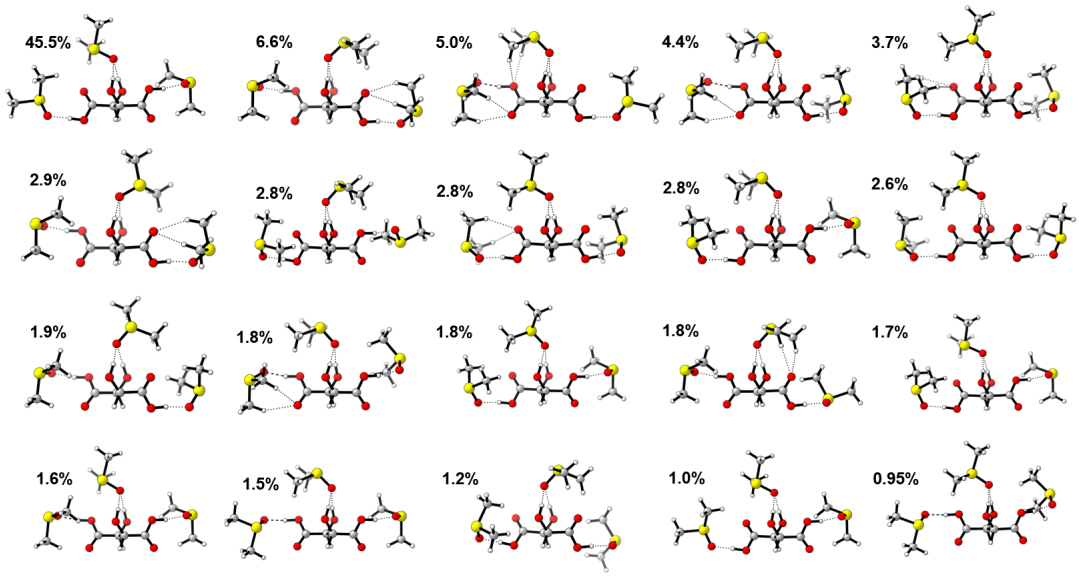

Figure 6.5: Lowest-energy geometries of (*S,S*)-Tartaric Acid with 0–4 explicit DMSO molecules.

est energy TA:2DMSO clusters have one uncoordinated COOH group, that is one DMSO is coordinated to the OH groups and one DMSO is coordinated to one of the COOH groups. 3DMSO clusters have both COOH groups hydrogen bonded to one DMSO molecule each, and the third DMSO molecule coordinates to both –OH groups at chiral centers (see Fig. 6.5). Given that the experimental symmetric O–C–C–O band appears halfway between the predicted band in the 2DMSO and 3DMSO clusters, it is possible that the true behavior lies somewhere in the middle and cannot be purely represented by static geometries. This hypothesis relies on the predicted vibrations being relatively free of other sources of error, such as frequency dependencies at the ωB97XD/6–311++G(2d,2p) level or issues arising from the harmonic approximation, which is more likely. There are no previous calculations on TA:DMSO complexes to compare with the current outcome of QCG generated TA:DMSO clusters.

6.3.3 Dimethyl tartrate

To further investigate the effects of microsolvation with multiple DMSO molecules, I also simulated DMT, separately with one and two DMSO molecules. The lack of –COOH

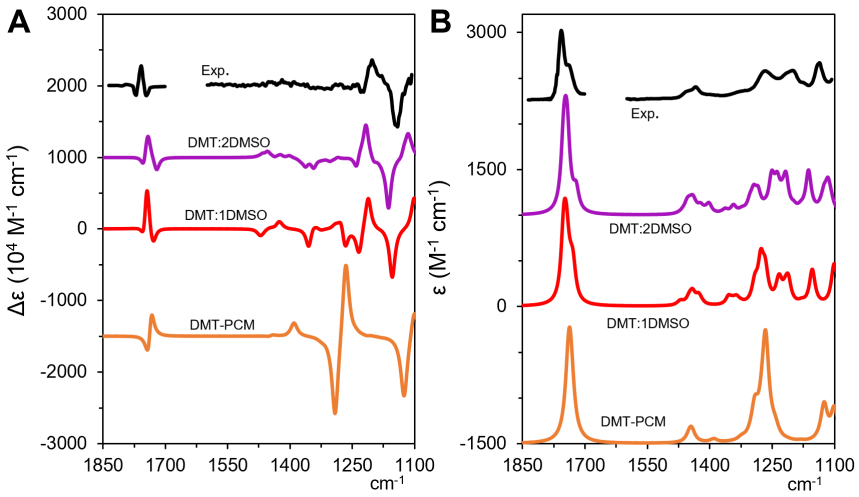

Figure 6.6: VCD and VA spectra of (*S*,*S*)-dimethyl tartrate with 0–2 explicit DMSO molecules.

	Max*Sim*VA	Max*Sim*VCD	Max*Sim*VDF
DMT+PCM	0.68	0.53	0.28
DMT:1DMSO	0.80	0.58	0.28
DMT:2DMSO	0.85	0.73	0.39

Table 6.1: Quantitative similarities for DMT experimental and simulated spectra

groups simplifies our analysis, as solvent coordination is more likely to take place at the chiral –OH groups instead and I can assume that solute–solvent clusters are limited to two DMSO molecules. For our calculations, I filtered for complexes that had hydrogen bonding to either or both –OH groups (DMT:1DMSO) or where each –OH group had one coordinated DMSO molecule (DMT:2DMSO). Low-energy clusters for DMT:1DMSO had both chiral alcohols coordinated to one DMSO with some bifurcation to nearby carbonyl or methoxy groups.

The simulated VCD and VA spectra are presented in Fig. 6.6, compared against our experimental data.[171] The lowest energy solute–solvent clusters with one and two DMSO molecules at the ωB97XD/6–311++G(2d,2p)/PCM(DMSO) level are presented in Figs.

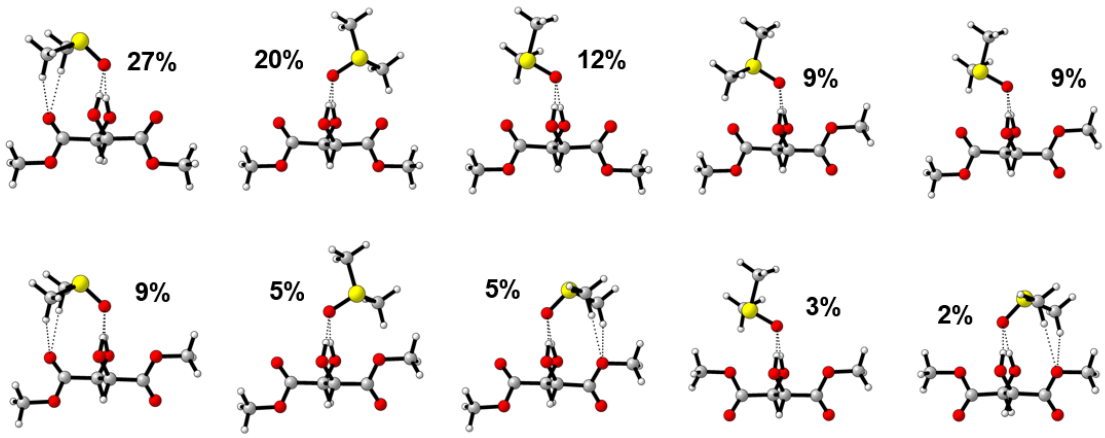

Figure 6.7: Lowest energy structures of (*S,S*)-dimethyl tartrate with 1 explicit DMSO molecule

6.7 and 6.8. Microsolvation with just one DMSO molecule, I see good improvement in the prediction of VCD intensities related to the symmetric and antisymmetric O–C–C–O vibrations as compared to calculations with only an implicit solvent model (DMT+PCM). The overall quantitative agreement with experimental spectra improves (see Table 6.1) with the addition of DMSO molecules.

Turning our attention to the carbonyl stretching region, for DMT in CCl_4 solvent, C=O stretching region shows only a bisignate VCD feature,[171,190] no VCD bands in D_2O solvent,[171] and a (–,+,–) triplet in DMSO-d_6 solvent.[171,190] A triplet was also observed for DMT in lecithin reverse micelles.[190] These differences underscore the influence of the solvent environment on VCD spectra, so it is important to analyze the origin of the (–,+,–) triplet in DMSO-d_6. For the DMT+PCM spectra, the bands are composed of symmetric and antisymmetric carbonyl vibrations. The two geometries with the largest Boltzmann-weighted populations have the carbonyl groups either cis or trans (84% and 15% pop.), which have also been collectively referred to as trans-$COOCH_3$ in the literature (vide infra),[171] and each predicts opposite signs for the symmetric and antisymmetric vibrations, with the higher energy trans carbonyl geometry predicting a (+,–) band and the lower energy cis carbonyl geometry predicting a (–,+) band. The lowest energy DMT+PCM ge-

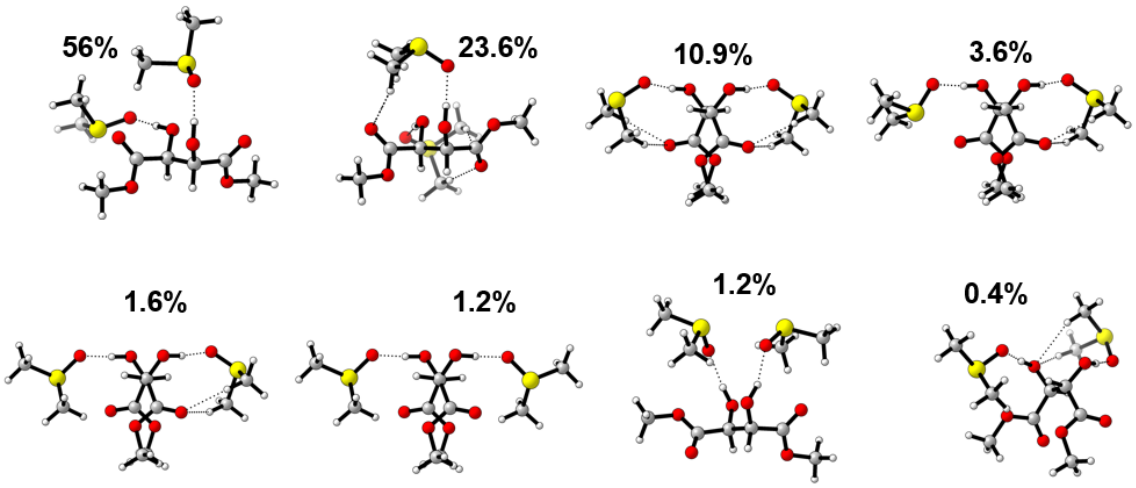

Figure 6.8: Lowest energy structures of (*S,S*)-dimethyl tartrate with 2 explicit DMSO molecules

ometry has overall C_2-symmetry. The carbonyl stretches have equal displacements of both carbonyls and additional contributions from nearby C–O–H bending motions.

In the microsolvated geometries, the C=O stretching vibrations are more localized instead, with minimal contributions from other motions. DMT:DMSO conformations predominantly fall into three categories: cis and trans with respect to the relative orientations of the carbonyl groups, (which have been collectively referred to as trans-$COOCH_3$),[171] and C_2-symmetric trans-H conformations. From the higher frequency side, cis carbonyl conformations have a (–,+) bisignate, and trans carbonyl conformations have a (+,–) bisignate; the higher wavenumber band corresponds to symmetric C=O vibration and the lower wavenumber band corresponds to anti-symmetric C=O vibration. Successively microsolvated geometries have increasingly unequal displacements of C=O groups as well as decreased contributions from other motions, and the symmetric and asymmetric C=O vibrations become increasingly localized. The C_2-symmetric clusters are found only in the DMT:2DMSO ensemble, where the entire cluster of DMT possesses C_2-symmetry.

For microsolvated DMT geometries, the symmetric vibration consistently falls at 1805 cm^{-1} for cis carbonyl geometry and $\sim$1800 cm^{-1} for trans carbonyl geometry whilst the

anti-symmetric vibrations have a bit more variance. The anti-symmetric vibration falls at $\sim$1780 cm^{-1} for trans carbonyl geometry conformations, whilst it falls at $\sim$1796 to 1800 cm^{-1} for cis carbonyl geometry conformations. This may explain the (–,+,–)-triplet. In order from left to right, labeled a, b, and c, I would have contributions to the triplet from a: (–) from symmetric vibration of cis carbonyl geometries, (+) from symmetric vibration of trans carbonyl geometries, (+) from anti-symmetric vibration of cis carbonyl geometry and (+) from symmetric vibration of trans-H conformers, and c: (–) from anti-symmetric vibration of trans carbonyl geometries.

The VCD of DMT in DMSO-d_6 has been studied previously by Zhang and Polavarapu, whereby DMT:2DMSO clusters were manually generated using low-energy rotamers of DMT.[171] A total of three groups of clusters were generated: trans-$COOCH_3$, trans-OH, and trans-OH, which are named based on Newman projections about the C2–C3 bond axis. Poor agreement was obtained using population weighting by computed Gibbs energies, so the ensemble was reweighted based on agreement with VCD and optical rotatory dispersion (ORD) experimental data. The Gibbs energy-weighted spectrum predicted a (–,+)-bisignate in the carbonyl stretching region and poor agreement for VA spectrum in that same region, with no significant VCD bands reported in the remainder of the spectrum. Satisfactory agreement was obtained using only the trans-$COOCH_3$ and trans-H clusters with 62.5% and 37.5% populations, respectively. I also find similar populations of about 82% and 18% for the trans-$COOCH_3$ and trans-H clusters, respectively, using only the Gibbs energies that give rise to the spectrum depicted in Fig. 6.6.

6.3.4 1-Indanol

The simulated VCD and VA spectra for (*S*)-IND are presented in Fig. 6.9 using several popular functionals. A summary of the similarity overlap values for each density functional using the experimental 1100 to 1700 cm^{-1} region is presented in Table 6.2. The geometries optimized with the B3PW91 and ωB97XD functionals are presented in Fig. 6.10.

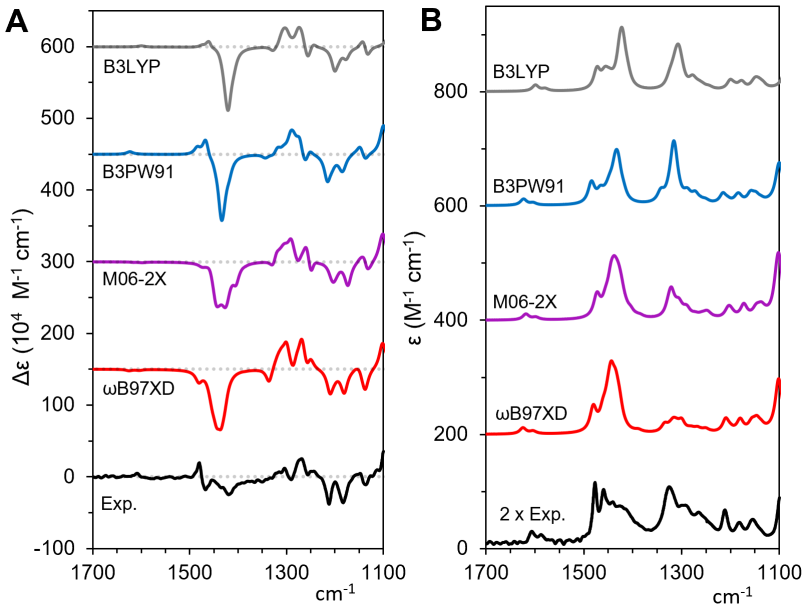

Figure 6.9: VA and VCD spectra of (*S*)-IND at multiple levels of theory

	*Sim*VA	*Sim*VCD	*Sim*VDF
B3LYP	0.79	0.49	0.62
B3PW91	0.79	0.54	0.64
M06-2X	0.71	0.52	0.57
ωB97-XD	0.67	0.51	0.50
ωB97-XD+LT	0.83	0.57	0.50

Table 6.2: Quantitative similarities for (*S*)-1-indanol experimental and simulated spectra

In a previous study[173] the VCD spectrum of an IND:DMSO complex was predicted at the B3LYP/6–311++G(2d,p) level, whereby the structures were generated by manual addition and reorientation of the DMSO molecule about the –OH group, which after DFT geometry optimizations resulted in ∼30 IND:1DMSO clusters. Those calculations yielded SimVCD and SimVDF of +0.61 and +0.66, respectively, with good reproduction of the subtle 1479–1466 cm^{-1} (+,–)-bisignate and many of the bands throughout the spectrum. With our present approach, many of the functionals predict intense VCD activities in the

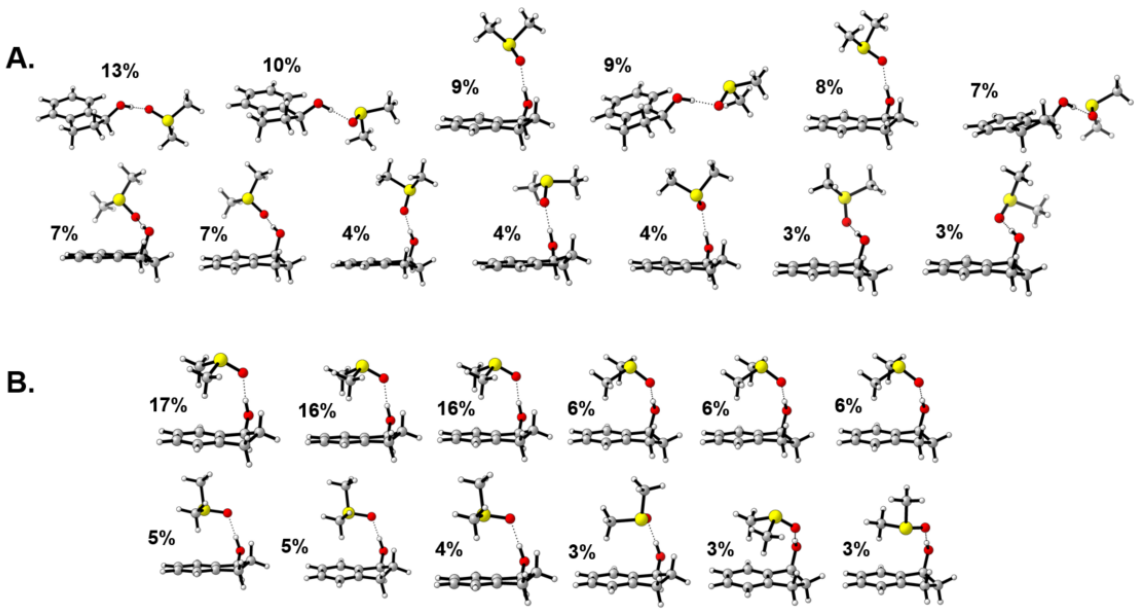

Figure 6.10: Lowest energy structures of (*S*)-IND using the (a) ωB97XD and (b) B3PW91 functionals

1500 to 1400 cm^{-1} region which is not consistent with that region in the experimental spectra. This misprediction results in overall lower SimVCD values for the same region than for the previous manual approach.[173] However, many of the VCD features in the 1100 to 1350 cm^{-1} region from the experimental VCD spectrum are reproduced well by the simulated spectra. Even the weaker features at 1153 and 1131 cm^{-1} appear in the simulated spectra at all levels of theory. Notably, the functionals appear to have difficulty reproducing the 1479–1466 cm^{-1} (+,–)-bisignate very well, with the B3LYP and B3PW91 functionals being the only methods to show both a (+)- and (–)-feature in that region, although the negative band's rotational strength is overpredicted in both levels of theory.

The ωB97XD functional, despite the overpredicted negative band at $\sim$1430 cm^{-1}, performs very well for the reproduction of the VCD bands in lower-wavenumber regions when compared to the other levels of theory. The SimVCD is +0.52 at a scale factor of 0.970, despite being hampered by the poor prediction of C–O–H bending modes in the 1500 to 1400 cm^{-1} region. B3PW91 slightly outperforms the other functionals with a SimVCD of +0.54. In the previous study on IND in DMSO with manually generated geometries,[37] the oppo-

site behavior was obtained; the predictions for higher wavenumber regions were in better agreement and lower wavenumber regions only showed moderate agreement. It is possible that manually generated geometries reproduced the VCD spectra of IND:DMSO-d_6 with a different set of geometries.

In the current calculations, the inclusion of Grimme's empirical dispersion D3(BJ) corrections[19] with the B3LYP functional did not improve overall VA or VCD agreement.

If I am to trust the QCG results, it is important to verify that sampling and identification of low-energy IND:DMSO clusters are accurate. To explain the discrepancy between the current and previous[173] approaches I considered two possibilities: (1) IND:DMSO static approaches may require the consideration of dynamic motions to fully describe VCD spectra in DMSO solvent and (2) identification of sources for differing quantitative agreement in the lower and higher wavenumber regions.

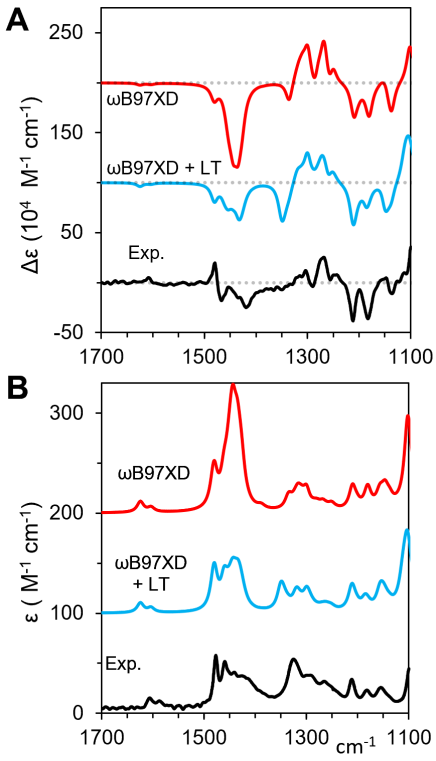

Figure 6.11: VA and VCD spectra of (*S*)-IND using LT scans along the C–O–H bond angle

Nicu and coworkers have previously reported the susceptibility of VCD calculations of

–OH bending regions to dynamic motion—which they investigated through linear transit (LT) scans along the –OH degrees of freedom[174]—and I suspected this might be a factor for the C–O–H bending region for (*S*)-1-indanol. To investigate this possibility, I focused on the lowest energy-optimized geometries at the ωB97XD/6-311++G(2d,2p)/PCM(DMSO) level and performed LT scans to examine the regional susceptibility of the VCD spectrum to –OH motion. The scans were conducted along two coordinates: C–O–H bending motion and O–H rotatory motion about the C–O axis.

The simulated spectra for the ωB97XD+LT approach are shown in Fig. 6.11, just above the experimental in DMSO-d_6, along with the original ωB97XD spectra without the LT scans from Fig. 6.9 for comparison. The band at $\sim$1430 cm^{-1} is not as intense as it was in the original simulated spectrum, which suggests that it may be an artifact from using static geometries, but the experimental bisignate remains unreproduced. Instead, the new VCD spectrum contains two (–)-bands at 1480 and 1460 cm^{-1}. Qualitatively, the VA spectra look remarkedly similar between the experimental and the ωB97XD+LT level, and this is reflected in the quantitative analysis. Inclusion of just C–O–H bending or O–H rotatory motion LT scans does not improve the spectra. Only including both scans improves VCD and VA agreement (see Table 6.2), suggesting that VCD of O–H bending region is very susceptible to dynamic motions.

In comparing our current versus the previous approach, I see distinct differences in the conformer geometries and populations with respect to DMSO binding positions for B3LYP and B3PW91 versus ωB97XD. DMSO appears to bind in two different ways: (a). DMSO and IND are approximately linearly bound and (b). DMSO is "stacked" above the plane of the indanol ring. In our present ωB97XD calculations, stacked geometries are more energetically favorable and contributions from linear geometries are low (see Fig. 6.10), whereas the opposite is true for B3PW91 geometries. In the previous approach,[173] linear geometries were more favorable than stacked geometries. I went through the IND:DMSO ensemble, separated the geometries into either linear or stacked and simulated their VCD

separately using the B3LYP optimized geometries (see Fig. 6.12). The linear geometries better reproduce the VA spectrum in the higher wavenumber region and mostly reproduce the VCD bands in that region as well; the (+,–)-bisignate is predicted to be a (+)-band with a shoulder instead. The stacked geometries better reproduce the 1000 to 1350 cm^{-1} region but suffer from the same mispredictions in the C–O–H bending region as the Boltzmann-weighted VCD spectrum with all conformers. The IND:DMSO geometries with LT scans were able to reproduce the (–) portion of the (+,–)-bisignate, suggesting that this (+,–)-bisignate is a result of two separate distinct ways of DMSO binding whilst the remainder of the spectrum is better predicted with a "stacked" model. However, the favorability of stacked geometries over linear may be due, in part, to the included empirical dispersion correction included in the ωB97XD functional. This has also been observed by the Merten group for chiral carboxylic acid MPAA at the B3LYP-D3(BJ) level,[7] as well as by Eikås et al. for cyclic oligopeptides at the B3LYP-D3 level.[22]

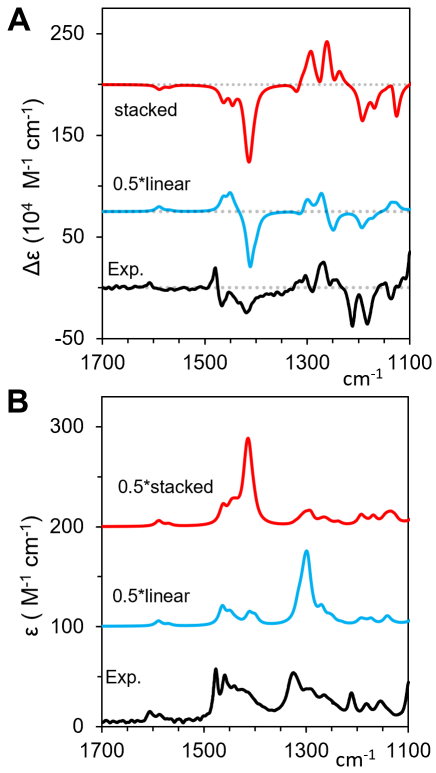

Figure 6.12: VA and VCD spectra of (*S*)-IND based on stacked vs linear geometries

6.4 Conclusion

I systematically investigated the effects of DMSO microsolvation via the QCG protocol within CREST on the hydrogen bonding signatures of several compounds. Investigations for pantolactone and 1-indanol suggest that the ωB97XD functional along with a sizeable basis set are capable of reproducing key VCD signatures. I note some issues in the reproduction of VCD and VA vibrations containing contribution from C–O–H bending modes for chiral alcohols, which appear as either widening of VCD signal or spurious VCD signal, which may be due to local dynamicity not captured in the static geometries. Additionally, the effects of incremental DMSO solvation were explored for tartaric acid and dimethyl tartrate, two small molecules with two chiral centers and multiple hydrogen bonding groups. Reproduction of the VCD signatures for TA was found to be particularly sensitive to microsolvation of the carboxylic acid groups near the chiral centers. The best agreement for DMT was found when two DMSO molecules were coordinated to the two chiral alcohol groups, with a good reproduction of the carbonyl stretching VCD bands. However, I did not attempt microsolvation runs for DMT with additional DMSO molecules.

While QCG itself is very convenient for generating possible cluster ensembles, subsequent optimizations and selected geometries pose challenges. The final populations of conformers in the IND:1DMSO ensembles are sensitive to the choice of functional, which raises doubts about whether all true low-energy conformers were included in our calculations. As seen for 1-indanol in Table 6.2 and Fig. 6.10, all investigated functionals yielded satisfactory quantitative comparisons (Sim values greater than 0.4), but the final set of conformers used for VCD calculations are functional dependent. Further experimental validation is necessary to determine the true low-energy conformers. Also, I have limited our current study to only VCD so it is not clear which set of geometries perform well for reproducing other chiroptical spectra. Regarding the TA:1DMSO clusters, solvation of the OH groups at chiral centers versus the COOH groups both satisfactorily reproduced the characteristic experimental bands, which raises the question of whether VCD alone can re-

liably conclude on the solvated geometries. As mentioned earlier, microsolvation with four DMSO molecules became very expensive and did not improve VCD predictions beyond those with three DMSO molecules.

Overall, the generation of microsolvated geometries via the QCG method in CREST appears to generate reliable DMSO clusters for the quantum mechanical interpretation of VCD spectra, at the computational cost of a semi-empirical method. It is necessary to perform filtering of weakly bound complexes before DFT calculations, which can be accomplished by comparison of the distances between the S=O and hydrogen bonding groups in the solute. Many of the original clusters generated by QCG contained non-interacting solvent molecules, which may be due to the large amount of sampling performed for each molecule and the metadynamics biasing potentials. Additionally, even though our QCG generated geometries for TA satisfactorily reproduced the experimental VCD spectra in the limited vibrational region, the same conclusion could not be obtained for three other carboxylic acids, α-methoxyphenylacetic acid (MPAA), α-phenylpropionic acid (PPA), and 2-phenylbutyric acid (PBA), all of which have been studied previously by the Merten group.[7,8] The formation of dimers of these acids at the concentrations used for VCD studies is an aspect that I have not explored.

CHAPTER 7

VOA of Ladderanoic Acid Dimers

This work relies on previous experimental studies by Dr. Jordan Johnson of our lab who performed VROA measurements on ladderanoic acids in Poland as wella s other coworkers who isolated these natural products.[191] Inspired by Johnson's paradoxical computational results with monomers, I decided to investigate the utility of modeling dimers in the interpretation of VCD and VROA spectra for these compounds.

7.1 Introduction

Chiroptical studies on carboxylic acid dimers are relatively few, and the majority of these focus on VCD spectroscopy rather than on VROA. Water is the preferred solvent for VROA, because this allows biologically-relevant molecules to be studied in their natural environment and water is weakly Raman-active, but this solvent causes competition between the formation of solute–solvent complexes and dimers due to its strong preference for hydrogen-bonding. Non-polar solvents such as chloroform allow for dimers to be the predominant species in solution,[7,8] but these solvents are not ideal for VROA measurements due to their corresponding Raman activity. He and Polavarapu studied the formation of dimers of α-arylpropanoic acids in chloroform solvent.[192] Góbi and coworkers studied (*S*)-(–)- and (*R*)-(+)-2-chloropropionic acid dimers in chloroform solvent.[193] Kuppens et al. studied the dimerization of (*R*)-(+)-tetrahydro-2-furoic acid in $CDCl_3$ and CS_2.[194] The dimerization of (–)-(1*S*,3*R*)-camphanic acid has been studied as a function of its concentration in $CDCl_3$, demonstrating that the absolute configuration of the monomeric species could only be identified in a dilute solution.[195] Xu and coworkers also investigated the formation of dimers and higher-order aggregates of lactic acid in $CDCl_3$, H_2O, and CH_3OH solvents as well as the intermolecular bonding with their respective solvents.[196] Rodríguez Ortega et al. studied the competing prevalence of monomeric and dimeric species of (*S*)-

(+)-ketoponic acid in $CDCl_3$ and CD_3CN.[197] The Merten group has performed extensive analysis of solvation effects and aggregation of chiral carboxylic acids in a variety of solvents, demonstrating the utility of VCD in understanding solute–solvent complexes and dimers.[7,8] More recently, De Waele et al. studied highly fluorinated carboxylic acid dimer contributions to VCD spectra.[198] Each of these studies demonstrated the sensitivity of VCD to the formation of these hydrogen bonding complexes, sometimes requiring the modeling of both monomer and dimer contributions to the VCD spectrum in order to obtain good agreement with experiment. Additionally, this sensitivity was leveraged to investigate the solution conformations of carboxylic acids across a range of solvents with differing polarities. Even more impressively, Urbanová et al. were able to apply VCD spectroscopy to investigate the supramolecular tetramer of (*S*)-2,2'-dimethyl-biphenyl-6,6'-dicarboxylic acid in $CDCl_3$ at a high concentration, obtaining good agreement between the experimental spectra and that of the modeled tetramer.

Matrix isolation-VCD (MI-VCD) measurements can be utilized to eliminate solute–solvent interactions from the liquid-phase and study monomeric species or even higher-order aggregates.[199] Xu and coworkers used MI-VCD to study two carboxylic acid containing compounds in rare gas matrices: tetrahydro-2-furoic acid[200] and lactic acid.[201] The distinction between monomeric and dimeric species was accomplished via varying the deposition temperature—low temperatures ($\sim$10 K) facilitate monomer deposition and higher temperatures ($\sim$24–30 K) facilitate the deposition of higher-order aggregates. In the case of lactic acid deposition at higher temperatures of a 0.2 M solution, the trimeric and tetrameric species were identified as the key contributors to the VCD spectra.[201]

Kaminský and coworkers studied the dimerization of lactic and malic acid using VROA in water and VCD in D_2O.[202] In this work, they demonstrated that increasing the concentration of the hydroxy acid had little to no effect on the experimental VROA.[202] It was also demonstrated that the double hydrogen-bonded dimers were not the most prevalent species in water, and that the VROA was best simulated from a mixture of contributions

from monomer and dimer spectra, which is likely due to the competing hydrogen-bonding propensity of water.[202] To the best of our knowledge, no VROA studies of carboxylic acid dimers has been performed in other solvents whereby molecular modeling was utilized to interpret the VROA spectra.

In 2018, the Polavarapu lab studied the VOA of naturally-occurring [5]- and [3]-ladderanoic acids in chloroform.[191] These molecules possess a rigid ladderane structure with a long alkyl side-chain terminating with a carboxylic acid (see Figure 7.1). Polavarapu and coworkers performed extensive calculations on monomers to model the VCD and VROA spectra of these two molecules. From this study, the following observations were made:

1. Correlation between experimental and calculated VCD of monomers did not give insight in the AC of the flexible side-chain. Some agreement was obtained for a few VCD bands, but the correlation between experimental and calculated VA was very poor which made this agreement untrustworthy.

2. Correlation between experimental and calculated VROA of monomers gave satisfactory evidence of the AC of the flexible side-chain. Agreement between the Raman spectra was very good, suggesting that correlations in the VROA spectra were trustworthy.

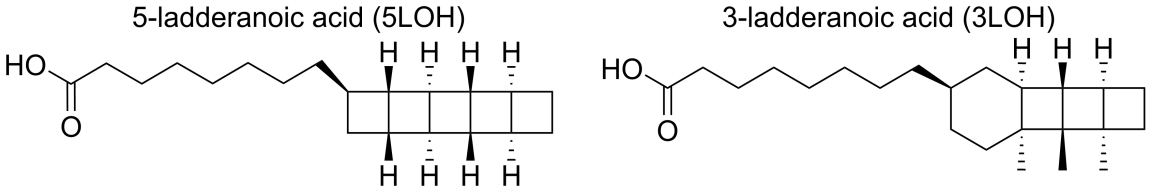

Figure 7.1: Structures of ladderanoic acids previously studied by VCD and VROA

Given that simulations of the VCD and VROA of these two molecules rely on the same underlying frequency calculation, it is puzzling why such good agreement was obtained for one chiroptical method and not the other. Since the treatment of dimers was neglected, the leading hypothesis behind the discrepancy is that VROA is less sensitive to the formation

of dimers than VCD. Taking into account the formation of dimers is computationally expensive due to both the inclusion of an additional molecule in the QM simulations and the extensive conformational flexibility of the side-chains. This leads to challenges in sampling conformational space and locating the low-energy conformers of these dimers. If VROA is truly less sensitive to dimerization, then this would highlight the utility of VROA in the study and AC determination of dimer-forming compounds.

In an effort to better understand the sensitivity of VROA and VCD to the formation of dimers, I undertook extensive simulations of the dimers of the [5]-ladderanoic acid compound. The [3]-ladderanoic acid has additional ring flexibility adjacent to the alkyl chain, further increasing the conformational complexity, and so was not chosen for this work despite the richer VCD spectrum.[191] However, it is unclear how the modeling of these dimers would help improve agreement between experimental and simulated VA and VCD given the distance from the carboxylic acid group to the closest stereocenter.

7.2 Methods

Conformational searches on (*R*)-5LOH (5-ladderanoic acid) were performed using the *Quantum Cluster Growth* (QCG) protocol[175] in the CREST program,[176] based on a modified procedure I have used previously to study DMSO–solute complexes.[157] By specifying (*R*)-5LOH as both the solute and the solvent, I hope to take advantage of the robust metadynamics and fast semi-empirical methods available in CREST to sample dimers of 5LOH (here referred to as d5LOH or "dimers of 5LOH"). This process located 1695 d5LOH geometries.

The geometries in the ensemble were then ranked based on single-point DFT energies at the B3LYP/6-31+G(2d,p)/PCM($CHCl_3$) with and without D3(BJ) dispersion corrections.[19] The geometries within the lowest 2.5 kcal/mol were then optimized at the same level. VCD and VROA calculations were performed on geometries within the lowest 2.0 kcal/mol. Due to the uncertainty in the entropic contribution to the Gibbs Energies for these large dimers,

all spectra were simulated based on zero-point energies (ZPEs).

For similarity measurements between experimental and simulated VROA and Raman spectra, the 1300 to 1200 cm^{-1} region was excluded from similarity calculations due to interfering solvent absorbance.

7.3 Results and Discussion

Despite the high conformational flexibility of the 5LOH monomers, which lead to considering nearly 8,000 conformers in the initial study,[191] the number of d5LOH dimers I must initially consider is manageable. However, the large molecular size of these dimers made optimizations of the entire ensemble prohibitive. To help located low-energy conformers, I elected to perform single-point optimizations and only optimize those with the lowest energies—an approach recommended by Ruud and coworkers for large, flexible molecules.[22,154]

The inclusion of empirical dispersion corrections, such as Grimme's D3[18] and D3(BJ)[19] models, typically leads to an overall lower agreement between experimental and simulated VCD spectra with several examples noted in the literature.[7,21–23] However, their inclusion may have an impact for d5LOH geometries due to the size of the dimer systems. Additionally, the effect of dispersion corrections for ROA is not well-understood. For these reasons I explored the VCD and ROA with and without dispersion corrections.

7.3.1 Vibrational Circular Dichroism

The comparison between the experimental and predicted VCD spectra of 5-ladderanoic acid and its dimers are presented in Figure 7.2. The experimental VCD spectra is quite noisy and has very few bands present. The spectra predicted at the B3LYP/6-31+G(2d,p) level has the highest quantitative similarity with the experimental spectra (*Sim*VCD of +0.45 at the scale factor used in Figure 7.2) however the spectra simulated at the B3LYP-D3(BJ)/6-31+G(2d,p) level reproduces the intense experimental band at $\sim$1230 cm^{-1} despite the lower overall *Sim*VCD of +0.24. Irregardless, the quantitative *Sim*VA for both sim-

ulated spectra are quite high, 0.83 for the B3LYP spectra and 0.78 for the B3LYP-D3(BJ) spectra, which are indicative of the better correspondence between the experimental and simulated VA spectra of dimers than for that of monomers predicted previously.[191]

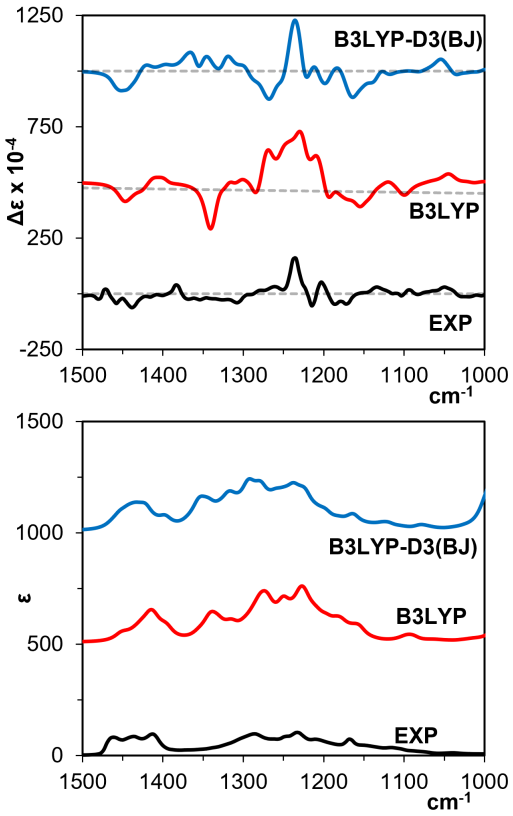

Figure 7.2: VCD of dimers of 5-ladderanoic acid

7.3.2 Vibrational Raman Optical Activity

The comparison between the experimental and predicted VROA spectra of 5-ladderanoic acid and its dimers are presented in Figure 7.3. The quantitative *Sim*Raman for both levels of theory are quite low, about 0.6, despite good correspondence between experimental and simulated Raman bands. This is likely because of differing optimal scale factors for the low wavenumber bands ($<$1200 cm^{-1}) and higher wavenumber bands ($>$1200 cm^{-1}) leading to only a mediocre *Sim*Raman. This issue is also reflected in the *Sim*ROA, which are +0.20 or less for both levels of theory. Despite this low quantitative similarity, there is good

correspondence between the experimental and calculated bands at the B3LYP-D3(BJ) level of theory until $\sim$1000 cm^{-1}.

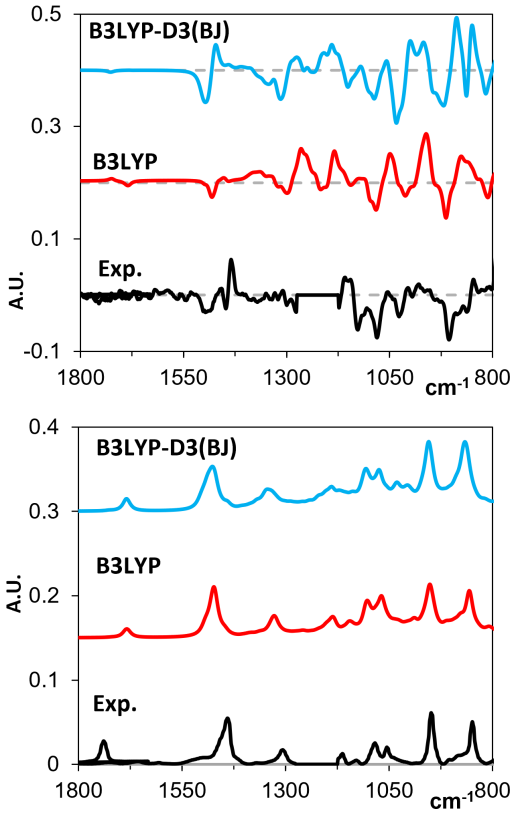

Figure 7.3: VROA of dimers of 5-ladderanoic acid

7.4 Conclusion

In this study, I have studied the dimerization of a flexible molecule using VCD and VROA spectroscopy. By modeling the dimers and exploring their conformational landscape, I gained insight into the comparative sensitivities of VCD and VROA to the formation of these dimers. I see good improvement in the VCD spectra of dimers as compared to monomers. This effect is not as noticeable in the VROA spectra, as good agreement is obtained with either monomer or dimer spectra. This highlights the potential utility of VROA to investigate dimer-forming compounds, without the added computational cost of modeling dimers. However, more VROA studies need to be performed of aggregating sys-

tems in non-polar solvents, such as chloroform, in order for these differing sensitivities to be confirmed.

CHAPTER 8

Rayleigh Optical Activity: AC Determination and the Influence of Conformational Distribution of Low-energy Conformers

Comparisons with experimental results presented herein are only possible due to recent, monumental efforts to overcome obstacles in the measurement of Rayleigh Optical Activity by our collaborators at the University of Strathclyde: Emmanouil Alexakis, Dr. Lewis MacKenzie, Dr. Aidan Arnold, and Dr. Robert Cameron. I thank them for allowing me to use their preliminary experimental RayOA data in this chapter.

8.1 Introduction

Up to this point, I have mainly discussed chiroptical methods that are very sensitive to conformational changes and intermolecular interactions. This allows chiroptical techniques to study these very effects, but require extensive conformational analysis to ensure that these effects are properly accounted for in the molecular model, otherwise correlations with experimental data will not be sufficient. As I have shown in Chapters 4 and 6, conformational flexibility and solute-solvent interactions can quickly become expensive and even inhibit a proper AC assignment. Herein, I expand on previous calculations related to Rayleigh Optical Activity[203] by exploring its sensitivity to conformational flexibility and intermolecular interactions as compared to other chiroptical spectroscopies.

The optical rotation (OR) of a molecule is directly proportional to the trace of the electric-dipole–magnetic-dipole polarizability tensor $\omega^{-1}G'_{\alpha\beta}$. The trace contains two elements of the same sign and a third, larger element of the opposite sign, leading to a near cancellation of the terms used to predict the OR. As a result, any effects that slightly change the diagonal elements of $\omega^{-1}G'_{\alpha\beta}$ can lead to an inversion of the OR. This leads to difficulties in correctly predicting the sign of OR through computation, as the near cancellation of terms is further complicated by the near cancellation of OR contributions from different

conformations in the molecular ensemble. Additional issues arise when attempting to compute small OR values, as predictions can often be off by an order of magnitude or worse. Remedying this often requires calculations at a much higher level of theory, so as to compute the $\omega^{-1}G'_{\alpha\beta}$ tensor elements with greater accuracy. Another possibility is to extract other stereochemical information from the $\omega^{-1}G'_{\alpha\beta}$ tensor. The theoretical formulation of Rayleigh Optical Activity (RayOA) was originally proposed in 1971 by Barron and Buckingham but has not been experimentally reported to-date. For both OR and RayOA, the elements of the electric-dipole–magnetic-dipole polarizability tensor $\omega^{-1}G'_{\alpha\beta}$ tensor are utilized, however, RayOA relies on contributions from *all* of the elements of $\omega^{-1}G'_{\alpha\beta}$ instead of just the trace. Zuber et al. showed that the computed RayOA of some model molecules was insensitive to the level of theory used, even using low-level Hartree–Fock calculations, while the OR was inconsistently predicted across several levels of theory.[203]

The magnitude of RayOA arises from the isotropic and anisotropic RayOA invariants in conjunction with the electric-dipole–electric-dipole polarizability tensor $\alpha_{\alpha\beta}$, the electric-dipole–magnetic-dipole polarizability tensor $\omega^{-1}G'_{\alpha\beta}$, and the rank-3 electric-dipole–electric-quadrupole polarizability tensor $A_{\alpha\beta\gamma}$. RayOA is defined as the intensity difference of Rayleigh scattered light from either the incident left- and right-circularly polarized (ICP), or in the scattered right- and left-circularly polarized light (SCP), or both (dual circular polarization or DCP). Each of these polarization schemes measure different linear combinations of the RayOA tensor invariants.

The frequency dependent electric-dipole–electric-dipole polarizability tensor $\alpha_{\alpha\beta}(\omega)$ is given as

$$\alpha_{\alpha\beta}(\omega) = \sum_{m\neq n} \frac{2\omega_{mn}\mu_{\alpha,nm}\mu_{\beta,mn}}{\hbar(\omega_{mn}^2 - \omega^2)} \tag{8.1}$$

where $\hat{\mu}_\alpha$ is the electric-dipole moment operator, $\mu_{\alpha,nm} = \langle\psi_m^0|\hat{\mu}_\alpha|\psi_n^0\rangle$, ω_{mn} is the transition frequency between states m and n; ω is the frequency of incident light; $\hbar = h/2\pi$; with h representing Planck's constant. In the approximation of $\omega_{mn} >> \omega$, the dynamic

electric-dipole–electric-dipole polarizability, $\alpha_{\alpha\beta}(\omega)$, can be reduced,

$$\alpha_{\alpha\beta}(\omega) \approx \sum_{m\neq n} \frac{2\mu_{\alpha,nm}\mu_{\beta,mn}}{\hbar\omega_{mn}} = \sum_{m\neq n} \frac{2\mu_{\alpha,nm}\mu_{\beta,mn}}{E_m^0 - E_n^0} = \alpha_{\alpha\beta} \tag{8.2}$$

where $\hbar\omega_{mn} = E_m^0 - E_n^0$.

The induced electric-dipole moment, μ_α, magnetic dipole moment, m_α, and the quadrupole moment $\Theta_{\alpha\beta}$, arising from the electric field $\boldsymbol{F}$, magnetic field $\boldsymbol{B}$ and their time derivatives are given as[52,204]

$$\mu_\alpha = \mu_\alpha^0 + G_{\alpha\beta}F_\beta + \omega^{-1}G'_{\alpha\beta}\dot{B}_\beta + \ldots \tag{8.3}$$

$$m_\alpha = m_\alpha^0 + G_{\alpha\beta}F_\beta - \omega^{-1}G'_{\alpha\beta}\dot{F}_\beta + \ldots \tag{8.4}$$

$$\Theta_{\alpha\beta} = \Theta_{\alpha\beta}^0 + A_{\alpha\beta\gamma}F_\gamma \tag{8.5}$$

where $G_{\alpha\beta}$ and $\omega^{-1}G'_{\alpha\beta}$ are, respectively, the real and imaginary parts of the electric-dipole–magnetic-dipole polarizability tensor, and $A_{\alpha\beta\gamma}$ is the electric-dipole–electric-quadrupole polarizability tensor.

The dynamic electric-dipole–magnetic-dipole polarizability, $\omega^{-1}G'_{\alpha\beta}$, is given as

$$\omega^{-1}G'_{\alpha\beta} = -\sum_{m\neq n} \frac{2\mathrm{Im}\{\mu_{\alpha,nm}m_{\beta,mn}\}}{\hbar(\omega_{mn}^2 - \omega^2)} \tag{8.6}$$

and the electric-dipole–electric-quadrupole polarizability tensor, $A_{\alpha\beta\gamma}$, is given as

$$A_{\alpha\beta\gamma} = \frac{4\pi}{h}\sum_{n\neq m} \frac{\omega_{mn}}{\omega_{mn}^2 - \omega^2}\mathrm{Re}\{\langle\psi_n^0|\hat{\mu}_\alpha|\psi_m^0\rangle\langle\psi_m^0|\hat{\Theta}_{\beta\gamma}|\psi_n^0\rangle\} \tag{8.7}$$

where $\hat{\mu}_\alpha$ and $\hat{\Theta}_{\beta\gamma}$ represent the electric-dipole and electric-quadrupole moment operators, respectively. The tensor elements of $\alpha_{\alpha\beta}$, $\omega^{-1}G'_{\alpha\beta}$, and $A_{\alpha\beta\gamma}$ are calculated using Gaussian 16.[83]

Rayleigh optical activity (RayOA) is determined by several tensor invariants of the $\alpha_{\alpha\beta}$,

$\omega^{-1}G'_{\alpha\beta}$, and $A_{\alpha\beta\gamma}$ tensors. The mean, $\bar{\alpha}^2$, and the anisotropy, β^2, of the electric-dipole–electric-dipole polarizability tensor $\alpha_{\alpha\beta}$ are

$$\bar{\alpha}^2 = \frac{1}{9}\Big(\alpha_{xx} + \alpha_{yy} + \alpha_{zz}\Big) \tag{8.8}$$

$$\beta^2 = \frac{1}{2}\Bigg\{\Big(\alpha_{xx} - \alpha_{yy}\Big)^2 + \Big(\alpha_{xx} - \alpha_{zz}\Big)^2 + \Big(\alpha_{yy} - \alpha_{zz}\Big)^2 + 6\Big[\alpha_{xy}^2 + \alpha_{xz}^2 + \alpha_{yz}^2\Big]\Bigg\} \tag{8.9}$$

The three RayOA invariants are

$$\alpha G' = \frac{1}{2}\Big(\alpha_{xx} + \alpha_{yy} + \alpha_{zz}\Big)\Big(G'_{xx} + G'_{yy} + G'_{zz}\Big) \tag{8.10}$$

$$\begin{aligned}\gamma^2 = \frac{1}{2}\Bigg\{&\Big(\alpha_{xx} - \alpha_{yy}\Big)\Big(G'_{xx} - G'_{yy}\Big) + \Big(\alpha_{xx} - \alpha_{zz}\Big)\Big(G'_{xx} - G'_{zz}\Big) \\ &+ \Big(\alpha_{yy} - \alpha_{zz}\Big)\Big(G'_{yy} - G'_{zz}\Big) \\ &+ 3\Big[\alpha_{xy}\Big(G'_{xy} + G'_{yx}\Big) + \alpha_{xz}\Big(G'_{zx} + G'_{xz}\Big)\alpha_{yz}\Big(G'_{yz} + G'_{zy}\Big)\Big]\Bigg\}\end{aligned} \tag{8.11}$$

$$\begin{aligned}\delta^2 = \frac{1}{2}\Big[&\Big(\alpha_{yy} - \alpha_{xx}\Big)A_{xyz} + \Big(\alpha_{xx} - \alpha_{zz}\Big)A_{yxz} + \Big(\alpha_{yy} - \alpha_{zz}\Big)A_{xyz} \\ &+ \alpha_{xy}\Big(A_{yyz} - A_{zyy} + A_{zxx} - A_{xxz}\Big) \\ &+ \alpha_{xz}\Big(A_{yzz} - A_{zyz} + A_{xxy} - A_{yxx}\Big) \\ &+ \alpha_{yz}\Big(A_{zxz} - A_{xzz} + A_{xyy} - A_{yxy}\Big)\Big]\end{aligned} \tag{8.12}$$

To eliminate the dependence on the incident laser intensity, associated constants and instrumental parameters, it is customary to report dimensionless circular intensity differentials (CID), Δ, as the ratio of the circular intensity difference, $I_\alpha^\gamma - I_\beta^\delta$, to the circular intensity sum, $I_\alpha^\gamma + I_\beta^\delta$, where superscripts indicate the polarization of the incident laser light and subscripts indicate that of the scattered light.

$$\Delta = \frac{I_\alpha^\gamma - I_\beta^\delta}{I_\alpha^\gamma + I_\beta^\delta} \tag{8.13}$$

The appropriate expressions for CIDs depend entirely upon on the instrumental polarization scheme.[6,52,205] In this work, I focus on the 90° scattered circular polarization (SCP) geometry. For input laser light propagating in the z-direction and right-angle scattered light propagating in the y-direction, the relevant expression for the CID is

$$\Delta = \frac{I_R^y - I_L^y}{I_R^y + I_L^y} = \frac{\frac{16}{3}\left(\frac{2\pi}{\lambda}\right)(3\omega^{-1}\gamma^2 - \omega^{-1}\delta^2)}{8\beta^2}. \tag{8.14}$$

In Eq. 8.14, superscript y represents input linear polarization in the right-angle scattering plane and subscripts R and L represent, respectively, the right- and left-circularly polarized scattered light components.

Note that the depolarized 90° incident circular polarization (ICP) geometry monitoring the z-polarized scattered light has the same expression for Δ as Eq. 8.14. That is,

$$\Delta = \frac{I_z^R - I_z^L}{I_z^R + I_z^L} = \frac{I_R^y - I_L^y}{I_R^y + I_L^y}.$$

In the expression provided for Δ, the numerator is proportional to Rayleigh optical activity, while the denominator is proportional to the corresponding Rayleigh activity.

The expressions I have provided for the Rayleigh activity and RayOA are analogous to those for Raman and VROA, where Raman and VROA expressions have corresponding normal coordinate derivatives of the electric-dipole polarizability tensors ($\frac{\partial \alpha_{\alpha\beta}}{\partial Q_k}$, $\omega^{-1}\frac{\partial G'_{\alpha\beta}}{\partial Q_k}$, and $\frac{\partial A_{\alpha\beta\gamma}}{\partial Q_k}$). Accurate computations of these tensor elements remains a practical challenge in the application of VROA due to the basis set sensitivity introduced by these derivatives. This sometimes requires that the basis set used for the estimation of the Raman and VROA tensors contains additional diffuse functions relative to the basis set used for the geometry optimization and subsequent frequency calculation.[206]

In this chapter, I will investigate the robustness of RayOA as a chiroptical technique through the comparison of experimental and theoretical results for three compounds: α-pinene, α-longipinene, and fluoxetine. I will also explore several other compounds for

which experimental data is not available in order to better understand the sensitivity of RayOA to chirality, conformational flexibility, and intermolecular interactions. These compounds are presented in Figure 8.1.

8.2 Methods

Hydrogen peroxide was chosen as a test molecule to examine the relationship between the axial chirality of the H–O–O–H dihedral angle and RayOA. A relaxed scan was performed from –180° to +180° of the H–O–O–H dihedral angle in steps of 10° at the B3PW91/6-311++G(2d,p) level in the gas-phase. The RayOA and OR of hydrogen peroxide at 532 nm was computed at the same level. Additional relaxed scans were performed on biphenyl and binaphthalene (BINAP) and corresponding RayOA and OR were computed the B3PW91/6-31+G(2d,p) DFT level.

The RayOA of $(1S,2R,7R,8R)$-$(+)$-α-longipinene and the enantiomers of α-pinene was measured as neat liquids. The enantiomers of fluoxetine was measured in methanol. Because the OR of fluoxetine enantiomers depends upon on the solvent used in the measurement,[207] and the AC of the samples is known, I herein instead refer to the AC for experimental measurements in methanol.

For $(1S,2R,7R,8R)$-α-longipinene and (R)-fluoxetine, a systematic conformational search was performed in Conflex[80] using the MMFF94s force field and a search limit of 20 kcal/-mol. This process located four conformations for $(1S,2R,7R,8R)$-α-longipinene and 351 conformations for (R)-fluoxetine. Due to difficulties Conflex had in maintaining the stereochemistry of L-chiro-inositol during the conformational search, I performed a search with Pcmodel 10.0 (GMMX search algorithm)[150] at the molecular mechanics (MM) level with 20 kcal/mol search limits. This process located 30 conformers of L-chiro-inositol. No such conformational analysis was undertaken for α-pinene or β-pinene, as these are small, rigid molecules with only one conformation each. Instead, the B3LYP/6-311G(d,p) optimized geometry for α-pinene, β-pinene, and [5]helicene were taken from the OR45

benchmark.[208] These molecules and their stereochemistries are presented in Figure 8.1. Experimental data is not provided for all molecules.

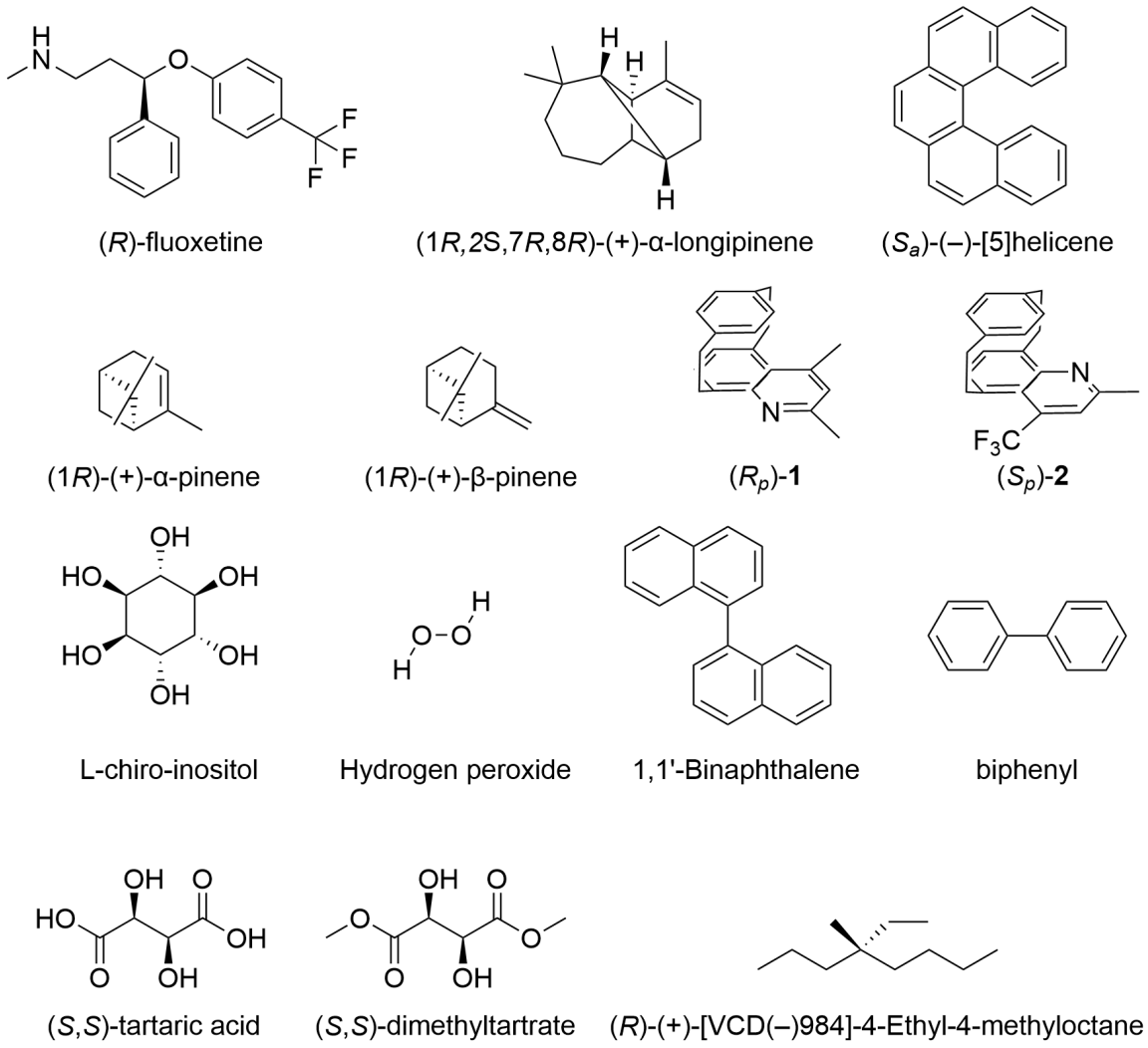

Figure 8.1: Structures of the molecules used in this RayOA study.

For α-pinene and β-pinene, the RayOA and OR at 532 nm were computed at the B3PW91, B3LYP, CAM-B3LYP, LC-wHPBE, and M06-2X levels of theory using the previously optimized geometry[208] with the aug-cc-pVTZ basis set. The conformers for α-longipinene could be divided into two sets based on the orientation of the seven-membered ring: two low-energy chair conformations (**C1** and **C2**) and two higher-energy ($\sim$8.5 kcal/-mol) boat conformations (**C3** and **C4**). All four conformations were initially optimized at the B3PW91/6-31+G(2d,p) and then at the B3PW91/6-311++G(2d,p) levels in the gas-

phase. Relevant quantities for OR and RayOA were then computed at the final level using an input wavelength of 532 nm.

The conformational ensemble of fluoxetine was optimized using the B3PW91 and M06-2X functionals with the 6-31+G(2d,p) basis set. A Polarizable Continuum Model (PCM) represented the methanol solvent used in the experimental measurements. The ensembles were then filtered for unique conformations and re-optimized at the same level of theory with Grimme's empirical D3(BJ) dispersion corrections for B3PW91 and the D3 dispersion corrections for M06-2X. This resulted in 234 and 212 unique conformations at the B3PW91 and B3PW91-D3(BJ) levels, respectively, and 208 and 201 conformers at the M06-2X and M06-2X-D3 levels of theory. The relevant quantities for OR and RayOA were computed for all conformers in the four ensembles. The lowest energy conformers within 2 kcal/mol in all four ensembles were then re-optimized using the 6-311++G(2d,p) basis set and the tensors were computed at the same level using an input wavelength at 532 nm. OR and RayOA values are reported based on Boltzmann averaging using electronic energies.

A conformational search of (*R*)-(+)-[VCD(–)984]-4-ethyl-4-methyloctane was performed with Pcmodel 10.0 (GMMX search algorithm)[150] with a 20 kcal/mol search limit. This located 505 conformers. The ensemble was optimized at the B3PW91/6-31+G(2d,p) level without PCM. Polarizability tensors were computed for conformers in the lowest 4.0 kcal/mol based on electronic energies (141 conformers) using an incident wavelength of 532 nm. OR and RayOA values are reported based on Boltzmann averaging using electronic energies.

Conformational searches for tartaric acid and dimethyl-tartrate solute–solvent clusters were reported previously.[157] Tartaric acid ensembles ranged from 0–4 explicit solvent molecules and dimethyl tartrate ensembles ranged from 0–2 solvent molecules. Polarizability tensors were computed for all reported geometries using an incident wavelength of 532 nm at the ωB97X-D/6-311++G(2d,2p) level with PCM representing the bulk DMSO solvent, which is the same level that geometry optimizations and frequency calculations

were originally performed. OR and RayOA values are reported based on Boltzmann averaging using zero-point energies.

8.3 Results and Discussion

Hydrogen peroxide does not posses a chiral center, but can have R_a or S_a axial chirality due to atropisomerism, or hindered rotation, about on the H–O–O–H dihedral angle. While the rotational energy barrier is too low for these atropisomers to be isolable, we can get an estimation of the expected RayOA for achiral molecules in a chiral orientation. A plot comparing the OR and RayOA along a relaxed scan of the H–O–O–H dihedral angle is presented in Figure 8.2. Here, hydrogen peroxide has S_a chirality when the dihedral angle is between –180 and 0°, and has R_a chirality when the dihedral angles is between 0 and +180°. Notably, the calculated OR flips signs three times for the S_a atropisomer while the RayOA retains a consistent sign, only switching sign when the chirality is reversed. The computed magnitudes of the OR are also quite high, reaching +/–200 deg cm^3/(g dm) close to the dihedral angles where the electronic energies are at a minimum. Meanwhile, the computed magnitude of RayOA almost reaches 3×10^{-4}. Overall, this suggests that RayOA is uniquely descriptive of the axial chirality of hydrogen peroxide.

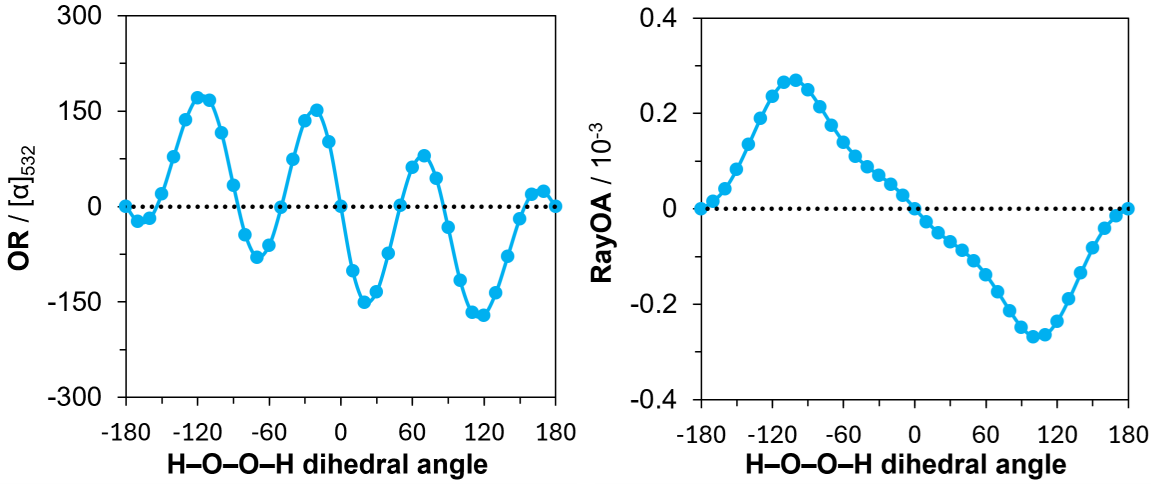

Figure 8.2: Comparison of OR and RayOA based on the H–O–O–H dihedral angle of hydrogen peroxide at the B3PW91/6-311++G(2d,p) level in the gas-phase. Geometries were obtained from a relaxed scan of the peroxide dihedral angle.

In 1974, Barron and Buckingham proposed a simple two-group model for Rayleigh and Raman Optical Activity CIDs assuming two neutral, optically inactive groups possessing at least three-fold or higher principal rotation axis separated by a bond or some distance, R.[209] This model has the advantage of not relying on molecular polarizabilities or other quantum mechanical information for the 90-degree SCP scattering geometry. The RayOA and ROA CID generalized two-group (G2G) model was also presented in 1977,[210] and the ROA model was reformulated in 1979 by Polavarapu under the atom-dipole interaction (ADI) model.[211] The ADI model is a classical model that builds the polarizability tensors using spherical atomic polarizabilities and the dipolar interactions between atoms. These models were originally formulated for VROA spectroscopy, which suffers from computational issues associating with obtaining normal coordinate derivatives of the relevant polarizability tensors. These models have garnered limited attention since their formulation. However, if these simpler models are capable of serving as a computationally efficient means for computing RayOA CIDs, which does not require normal coordinate derivatives, then that would be advantageous for AC determination by RayOA.

For the 90-degree depolarized ICP scattering geometry, the formula for the RayOA CID in Barron's two-group model is of the form

$$\Delta_z = \frac{2\pi R \sin(2\theta)}{\lambda(5+3\cos(2\theta))}$$

where θ is the dihedral angle between the two groups and λ is the wavelength of the incident light. This same equation also applies for 90-degree SCP geometry with input linear polarization in the scattering plane. The validity of this simple model as compared to quantum chemical approaches has yet to be reported on, and so I chose to investigate this in detail using biphenyl, where the phenyl rings have C_6 principal rotation axes, as a test molecule for this model. Overall, results obtained from the two-group model and DFT calculations agree well with 2θ dependence (see Figure 8.3). However, when this same

equation was applied to H_2O_2, the RayOA varied as a function of θ and not 2θ (see Figure 8.4).

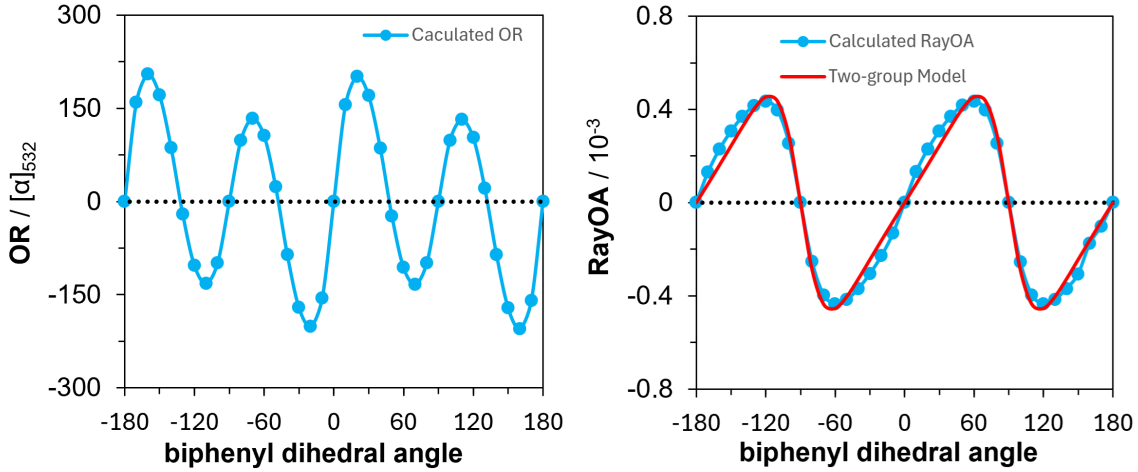

Figure 8.3: Comparison of OR and RayOA based on the biphenyl dihedral angle in a relaxed scan at the B3PW91/6-31+G(2d,p) level. In red is the RayOA obtained from Barron's two-group model. Geometries were obtained from a relaxed scan of the biphenyl dihedral angle.

I was able to implement the ADI model as described by Polavarapu[211] to compute the polarizability tensors necessary for RayOA. This implementation relied on spherical atomic polarizabilities reported by Applequist which are fitted to available experimental data,[212] but atomic polarizabilities have been reported more recently by Litman et al. which are fitted to computed molecular polarizabilities at the CCSD level.[213] These data are presented in Figure 8.4. Only the ADI model captures the dependence of the sign of RayOA CIDs as a function of the H–O–O–H dihedral but the ADI model also overpredicts the magnitude of the RayOA CIDs. The O–H groups in H_2O_2 do not satisfy the minimum three-fold symmetry requirements for Barron's simple two-group model, which may explain the lack of agreement between the two-group model predictions and DFT calculations. It is also important to note that the atomic polarizabilities reported by Applequist and Litman et al. vary significantly for the same atom types, with the presented data utilizing Applequist's atomic polarizabilities. If the atomic polarizabilities reported by Litman et al. are used instead,[213] the dependency on the H–O–O–H dihedral angle resembles that of Barron's

two-group model, indicating the sensitivity of the ADI model to the chosen atomic spherical polarizabilities.

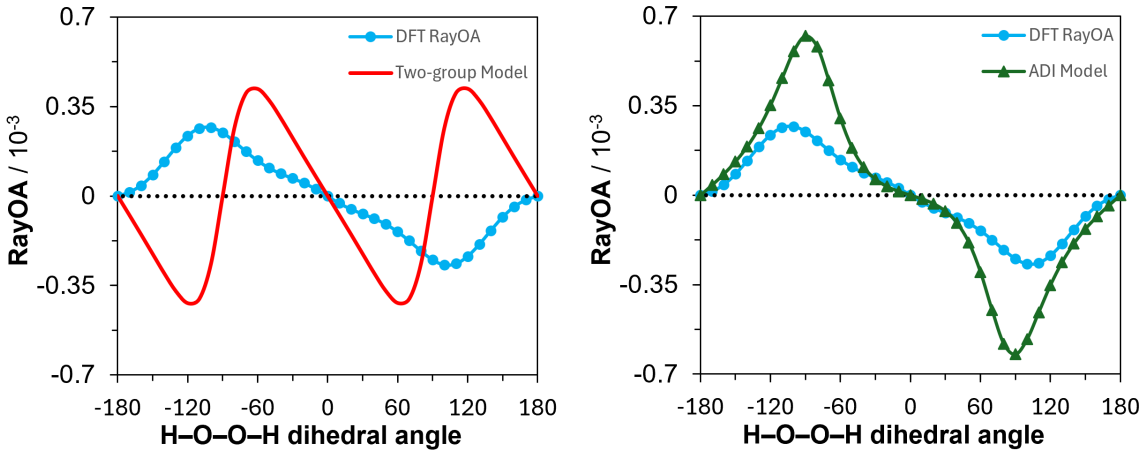

Figure 8.4: Comparison of RayOA computed by DFT methods and by classical two-group model (left) and ADI models for H_2O_2 (right).

The OR and RayOA of BINAP geometries along a relaxed scan of the naphthalene dihedral angles are presented in Figure 8.5. The data points between –60° and +60° are unreliable as one of the naphthalene subunits bent out-of-plane to avoid unfavorable steric interactions between the C2 and C2' hydrogen atoms, which results in an asymmetric RayOA curve. However, Barron's two-group model captures the dependency of RayOA on the naphthalene dihedral angle. It is important to note that the naphthalene subunits have C_2 principal rotation axes and do not meet the three-fold axis requirement of Barron's two-group model, despite the good agreement with the computed DFT CIDs. In summary, predictions from Barron's two-group model appear to match DFT predictions for groups satisfying minimum three-fold rotational axis symmetry (in the case of biphenyl) and also for groups not satisfying minimum three-fold rotational axis symmetry (in the case of BINAP). However, Barron's two-group model does not agree with DFT predictions for H_2O_2 , where O–H groups do not satisfy the minimum three-fold rotational axis symmetry.

α-longipinene displays the largest magnitude of RayOA among the three molecules for which experimental data is available, which is on the upper-end of what is typically

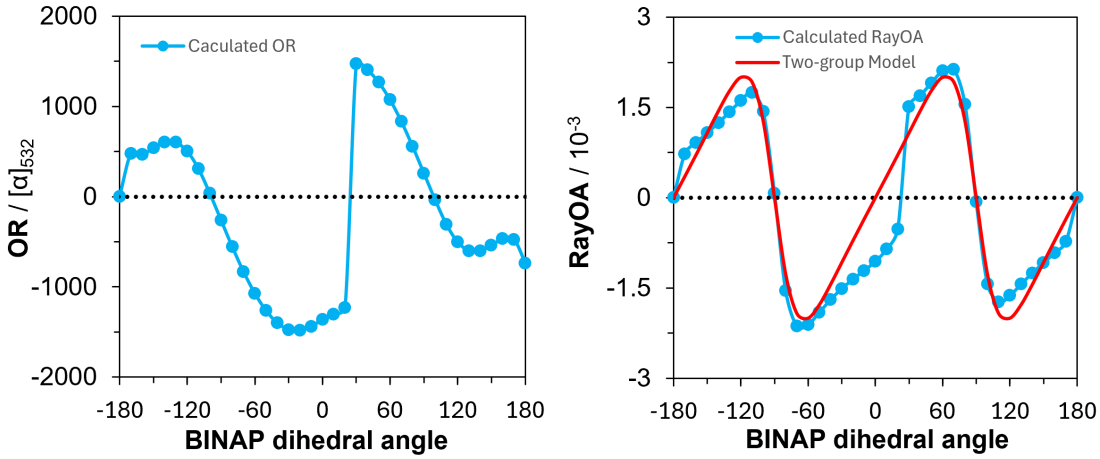

Figure 8.5: Comparison of OR and RayOA at the B3PW91/6-31+G(2d,p) level based on the BINAP dihedral angle. In red is the RayOA obtained from Barron's two-group model. Geometries were obtained from a relaxed scan of the dihedral angle.

Table 8.1: Experimental RayOA of several enantiopure samples

	Experimental RayOA ($\times 10^{-4}$)
(+)-α-pinene	–4.5 ±0.3
(–)-α-pinene	+4.5 ±0.5
(+)-α-longipinene	+22 ±3
(*S*)-fluoxetine	–9.1 ±2.5
(*R*)-fluoxetine	+6.0 ±1.8

expected from molecules ($\sim 10^{-4} - 10^{-3}$). Fluoxetine enantiomers also display a large magnitude of RayOA, with low enough error that there is good confidence in the sign of each enantiomer. These two molecules were measured with an early version of an RayOA spectrometer and so the data are noisy and there is not good confidence in the experimental magnitudes of the presented CIDs. For α-pinene, the experimental error is quite small relative to the experimental values owing to an update version of the RayOA instrumentation, and mirror-image RayOA values are obtained for enantiomers.

α-pinene only has one conformer, making it a good example by which to explore the effect of different levels of theory on RayOA and agreement with experimental spectra. I chose several popular functionals for studying the relationship between OR and RayOA and

the computed values are presented in Table 8.2. Here I am predicting the OR and RayOA at multiple levels of theory using the same geometry, allowing us to examine the influence of the chosen DFT functional without a dependency on differences between structures optimized at different levels of theory. There is remarkable consistency in the predicted RayOA of α-pinene, in regards to both the sign and magnitude of RayOA, but only the sign of OR is consistent.

Similarly to α-pinene, β-pinene serves as another example to investigate the robustness of RayOA at multiple levels of theory. β-pinene is a problematic case for OR calculations as the sign, and sometimes magnitude, of calculated OR fail to correlate well with experimental OR at 589 nm.[208] Indeed, there is significant variance in the computed OR of β-pinene across the levels of theory I have chosen, with the LC-wHPBE level predicting an opposite sign to the other levels of theory.

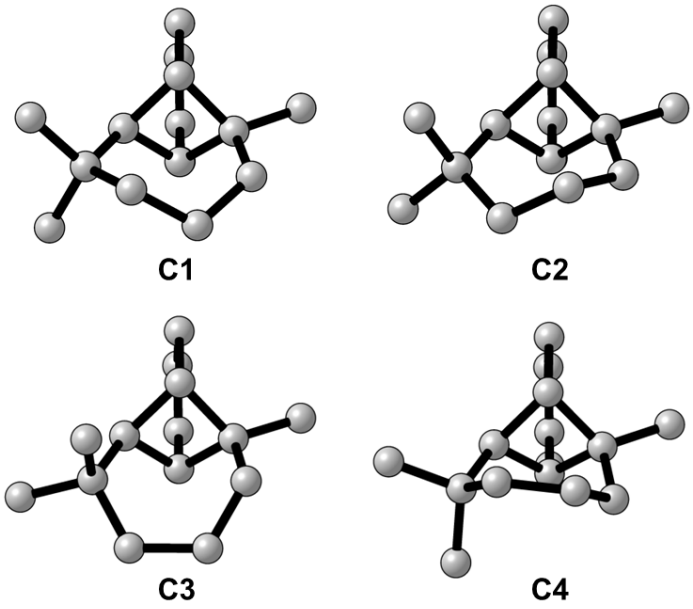

Figure 8.6: The four conformations of α-longipinene. Hydrogens are omitted for clarity

The four conformations of α-longipinene all display the same sign of RayOA, varying in magnitude between $\sim$2–8$\times10^{-4}$ (Table 8.2). The OR flips sign between each conformer, with **C1** and **C3** being negative and **C2** and **C4** being positive (see Figure 8.6 for depictions of the conformations). Conformers **C3** and **C4** are significantly higher in energy

Table 8.2: RayOA and OR of α-pinene and conformers of α-longipinene at several levels of theory

	RayOA ($\times 10^{-4}$)				
	B3PW91	B3LYP	CAM-B3LYP	LC-wHPBE	M06-2X
α-pinene	–3.56	–3.68	–3.84	–3.76	–3.66
β-pinene	–2.11	–2.11	–2.02	–2.15	–2.36
α-longipinene: **C1**	–1.89		–2.07		
α-longipinene: **C2**	–7.87		–8.54		
α-longipinene: **C3**	–3.86		–3.99		
α-longipinene: **C4**	–5.86		–6.46		

	OR				
	B3PW91	B3LYP	CAM-B3LYP	LC-wHPBE	M06-2X
α-pinene	+67.39	+56.06	+73.98	+85.79	+74.73
β-pinene	+27.53	+36.35	+12.46	–10.73	11.08
α-longipinene: **C1**	–33.59		–51.93		
α-longipinene: **C2**	+33.48		+27.42		
α-longipinene: **C3**	–49.11		–56.21		
α-longipinene: **C4**	+22.55		+5.64		

($\sim$8.5 kcal/mol) which means that the Boltzmann-averaged OR relies on the both the energy difference between **C1** and **C2**, which is quite small ($\sim$0.16 kcal/mol), and accurate predictions of OR for each conformer. For **C1**, the OR at the CAM-B3LYP level is $\sim$50% greater than that at the B3PW91 level.

Fluoxetine serves as a good case study for further exploring the influence of conformation on RayOA. As I have seen for α-longipinene, which had limited conformational flexibility, RayOA between conformers appears to change in magnitude but not in sign while OR varies drastically. With an initial 351 conformations to consider, I can properly explore the variance of RayOA in terms of conformational flexibility.

The Boltzmann-averaged RayOA for fluoxetine, which are presented in Table 8.3, are consistent across all four levels of theory. Notably, the inclusion of empirical dispersion

Table 8.3: Boltzmann-averaged RayOA and OR for (*R*)-fluoxetine

	6-31+G(2d,p)		6-311++G(2d,p)	
functional	OR	RayOA ($\times 10^{-4}$)	OR	RayOA ($\times 10^{-4}$)
B3PW91	+16.3	+16.3	+4.8	+17.3
B3PW91-D3B(J)	–66.6	+16.6	–80.5	+17.9
M06-2X	–74.2	+18.4	–79.3	+18.1
M06-2X-D3	–76.2	+17.5	–81.2	+18.1

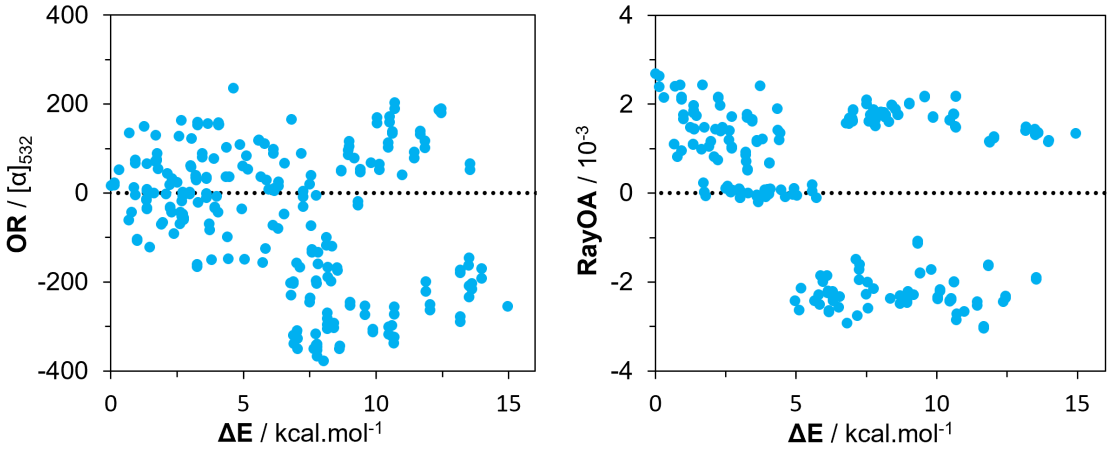

Figure 8.7: Comparison of OR and RayOA of conformers of fluoxetine based on electronic energies at the B3PW91/6-31+G(2d,p) level.

corrections considerably changes the distribution of low-energy conformers using either the B3PW91 or M06-2X functionals. The Boltzmann-averaged OR are consistent across the M06-2X and M06-2X-D3 levels but are not consistent between the B3PW91 and B3PW91-D3 levels of theory.

While I did not measure the OR of (*R*)-fluoxetine at 532 nm, the specific rotation of (*S*)-fluoxetine at 589 nm is reported to be +1.60 ° in methanol solvent.[207] With the exception of B3PW91 without dispersion corrections, the sign of OR agrees with experiment but the magnitude is over-predicted.

A closer examination of the OR and RayOA values for all conformers at the B3PW91/6-31+G(2d,p) level (Figure 8.7) shows that the sign of RayOA remains consistent until ∼5

kcal/mol, after which the RayOA begins to flip between positive and negative values of approximately the same magnitude.

It is important to note that the calculation to obtain the quantities necessary for RayOA is relatively simple, and that the optimization of the entire conformational ensemble remains the largest obstacle in obtaining a Boltzmann-averaged CID. If RayOA is truly less sensitive to conformational flexibility or subtle changes in geometry, as reported by Zuber et al.,[203] then it is worth asking if the geometry optimizations I performed were necessary to obtain an accurate RayOA CID. To test this, I performed single-point calculations on the unoptimized 351 conformers of fluoxetine located from a systematic conformational search at the B3PW91/6-31+G(2d,p) level with PCM representing the methanol solvent. This process also computed the quantities necessary to compute the RayOA invariants and obtain CIDs for all unoptimized geometries in the ensemble. The single-point energies and final electronic energies after optimization are generally considered to correlate well, and ranking geometries by single-point energies is a viable strategy to locate low-energy conformers.[22,154] Boltzmann-averaging based on the single-point electronic energies gives a CID of $+6.7 \times 10^{-4}$, which falls within the experimental CID but is approximately half of the CID obtained after geometry optimizations. Additionally the RayOA CIDs of individual conformers follows the same trend as in Figure 8.7, where the RayOA does not flip sign until $\sim$ 3kcal/mol. This agreement using the unoptimized geometries demonstrates the robustness RayOA as a computed property.

As an additional test case for the effect of conformational flexibility on RayOA, I also modeled a common, optically active saccharide L-chiro-inositol in implicit solvation of water. The conformational mobility of the saccharide ring, coupled with the hydrogen bonding groups present at each carbon stereocenter makes L-chiro-inositol difficult to study with chiroptical methods such as VCD and VROA. A similar saccharide, β-D-glucopyranose, required the inclusion of eight explicit water molecules for optimal agreement with experimental VCD spectra.[179] Explicit solvation's influence on chiroptical properties is two-fold:

Table 8.4: Boltzmann-averaged RayOA and OR for L-chiro-inositol with PCM representing water

	Electronic Energies		Gibbs Energies	
functional	OR	RayOA ($\times 10^{-4}$)	OR	RayOA ($\times 10^{-4}$)
B3PW91	+6.14	–1.14	–31.0	–1.39
B3PW91-D3B(J)	+58.62	–0.30	–22.4	–1.10
M06-2X	+22.48	–1.43	–31.7	–2.27
M06-2X-D3	+71.39	+0.51	–8.4	–1.16

solvent molecules can (1) alter the computed chiroptical properties through the formation of solute–solvent complexes via favorable intermolecular interactions and (2) bias or stabilize the energies of certain conformers, thus altering the relative energies of conformers which affects the Boltzmann averaging of chiroptical properties. As an additional investigation, I also performed polarizability tensor calculations on tartaric acid and dimethyl-tartrate with implicit and explicit DMSO, which I presented in Chapter 6, in order to examine how sensitive the Boltzmann-averaged RayOA is to solvation effects.

Table 8.4 presents the Boltzmann-averaged OR and RayOA values for L-chiro-inositol. Here, I use both electronic and Gibbs free energies to explore influences of conformational energy distributions on the Boltzmann-averaged RayOA. With only 30 conformations in the initial ensemble, the frequency calculations required for computing Gibbs energies are more tractable than with (*R*)-fluoxetine's larger ensemble. The choice of energies has a significant effect on the Boltzmann-averaged OR, with positive values being predicted with electronic energies and negative values being predicted with Gibbs energies. Variance in the predicted OR magnitudes are also quite high. Unlike with the RayOA CIDs for fluoxetine, we see for the first time a change in sign of the Boltzmann-averaged RayOA when electronic energies are used at the M06-2X-D3 level.

To further explore the sensitivity of RayOA to the formation of intermolecular interactions, we will investigate the predicted RayOA of tartaric acid (TA) and dimethyltartrate

(DMT) in DMSO solvent. As discussed in Chapter 6, the modeling of these intermolecular interaction via the inclusion of explicit solvent molecules is crucial for reproducing the VCD spectra in DMSO. The Boltzmann-averaged OR and RayOA of DMT and TA are presented in Table 8.5. Due to potential issues with accurate entropic contributions of low-frequency vibrational modes of solute–solvent complexes, I chose to use ZPEs instead of Gibbs thermal energies.

For DMT, there is little variation in the predicted OR if either electronic or Gibbs energies are used. The sign of RayOA is also consistent across both choices, with the DMT-PCM and DMT-2DMSO ensembles agreeing well in magnitude. If the CID is computed for individual solute–solvent clusters, I note that the sign is very consistent across the DMT-1DMSO and DMT-2DMSO ensembles, with each having three and two clusters that are in opposite sign to that of the final Boltzmann-averaged RayOA CID.

For TA, choosing to Boltzmann-average based on electronic or Gibbs energies has a drastic effect on the predicted OR. The shift in populations causes a sign change in both the TA-1DMSO and the TA-2DMSO ensembles, and choosing to use either electronic or Gibbs energies does not give a conclusive result of the sign of OR. There is a change in sign for RayOA in the TA-1DMSO ensemble depending on if electronic or Gibbs energies are used. It is worth noting that the majority of solute–solvent clusters with 2–4 DMSO molecules are the same sign as the final predicted RayOA CID, with the TA-2DMSO ensemble all having positive CID values. The TA-3DMSO and TA-4DMSO ensembles only have two and five clusters with negative RayOA CID, respectively, while half of the solute–solvent clusters in the TA-1DMSO ensemble have negative CIDs. These data suggest that RayOA is partially sensitive to the formation of strong intermolecular interactions across the solute–solvent ensemble. However, using ZPEs instead of raw electronic energies gives both consistent sign and magnitude of RayOA.

As a final test, I was curious what the magnitude of RayOA would be for molecules with large magnitudes of OR or chiralities more complicated than point chiralities. Chiroptical

Table 8.5: Boltzmann-averaged RayOA and OR for dimethyl tartrate and tartaric acid with implicit and explicit DMSO molecules

	Electronic Energies		Zero-Point Energies	
functional	OR	RayOA ($\times 10^{-4}$)	OR	RayOA ($\times 10^{-4}$)
DMT-PCM	+20.07	+2.72	+29.71	+2.69
DMT-1DMSO	+53.40	+5.93	+63.71	+6.03
DMT-2DMSO	+70.19	+3.67	+54.05	+2.15
TA-PCM	+30.97	+1.38	+28.13	+3.68
TA-1DMSO	+16.25	–6.81	–10.53	+1.31
TA-2DMSO	–17.20	+5.52	+0.26	+5.43
TA-3DMSO	–58.76	+4.52	–55.23	+4.61
TA-4DMSO	+62.96	+4.64	+57.56	+4.85

spectroscopies such as OR and ECD can be dominated by higher-order chiralities which can complicate AC determination. I have partially investigated this in my examinations of H_2O_2 and biphenyl, which had axial chirality depending on the dihedral angle, but a more detailed investigation is worthwhile.

Helicenes are polyconjugated rings that possess helical chirality, which is considered a one-dimensional chirality. The experimental OR for these compounds can easily be several thousand degrees. For this case, I obtained coordinates of a previously optimized (S_a)-[5]helicene from the OR45 study.[208] This molecule was chosen because the modeling of longer helicenes usually requires dispersion corrections for more accurate computations of OR due to overlapping of the benzene rings, which can complicate my analysis. With the CAM-B3LYP functional, the computed OR at 532 nm is of large magnitude –3263 deg cm^3/(g dm) but the computed RayOA is only -1.12×10^{-3}. This indicates that [5]helicene has only moderate RayOA despite the considerable OR. To further test this, I chose two examples of planar chirality, a two-dimensional chirality, from a study published in *Eur-JOC* which are labeled as **1** and **2** in Figure 8.1.[214] Their RayOA CIDs are $+0.79\times10^{-4}$ and -0.033×10^{-4}, respectively. These values are in the lower-range of what is typically

expected of RayOA magnitudes. The incident wavelength I chose for [5]helicene is 532 nm, where [5]helicene absorbs light.

Lastly, I investigated the OR and RayOA of (*R*)-(+)-[VCD(–)984]-4-ethyl-4-methyloctane. This molecule is technically chiral but has an extremely small OR owing to its specific stereoelectronic properties. The experimental OR is reported to be $[\alpha]_{365} = +0.70$ and $[\alpha]_D = +0.19$.[47] Since this molecule is crypto-optically active and very flexible, I was interested in how effective RayOA is as a possible chiroptical technique to probe the chirality of this molecule. The final Boltzmann-averaged OR is +5.36 and the RayOA CID is $+1.20\times10^{-5}$. The computed RayOA CIDs for this compounds is very small.

8.4 Conclusion

I have investigated the RayOA of several model molecules, comparing calculated versus experimental RayOA for some. For α-longipinene and α-pinene, which have very few conformers, I obtain good correspondence between the signs of calculated and experimental RayOA using several levels of theory. I note strong variance in the predicted OR but not for the predicted RayOA.

For fluoxetine, which has a considerably sized ensemble, I am able to reproduce both the sign and magnitude of RayOA. For low-energy fluoxetine conformations, the sign of RayOA remains consistent while the OR varies significantly which suggests that RayOA is insensitive to the distribution of low-energy conformers. In the case of L-chiro-inositol, which I only investigated computationally, we see that the choice of electronic versus Gibbs thermal energies plays a role in consistent predictions of RayOA. However, we only see the Boltzmann-averaged RayOA for L-chiro-inositol only flips sign once across multiple levels of theory which still suggests that RayOA is much less sensitive to conformational flexibility than OR. For TA, there is also a change in the predicted sign of RayOA if either electronic or ZPEs are used for the TA-1DMSO ensemble, with the electronic Boltzmann-averaged RayOA CID having an opposite sign to all other levels of theory. Overall, I would

recommend that predictions of RayOA are made with Gibbs or zero-point energies (ZPEs) wherever possible.

It is unclear how sensitive RayOA truly is to intermolecular interactions. I have investigated this aspect in two ways, (1) the inclusion of dispersion corrections which help to accurately model London dispersion interactions, and (2) by investigating the consistency of RayOA across two molecules with varying amounts of incremental explicit solvation. For fluoxetine and L-chiro-inositol, dispersion interactions do not appear to play a significant role in predictions of RayOA, although magnitudes do vary somewhat for L-chiro-inositol CIDs. Incremental microsolvation of chiral molecules appears to cause the sign of RayOA CIDs to be more consistent across the ensemble, as we see with DMT and TA, however the sign of RayOA can still be consistently predicted. Further experimental evidence, especially across multiple solvents, is necessary in order to elucidate the true sensitivity of RayOA to the formation of intermolecular interactions. Dimerization is also an aspect that must be considered in future studies, especially in the case of homochiral dimer formation.

In particular, the overall low predicted CIDs seen for molecules possessing planar chirality might indicate that RayOA is less sensitive to this specific chirality, however, I have only studied two such molecules. Additionally, it is possible that crypto-optically active compounds may also have low RayOA, although I have only studied the RayOA CIDs of one such molecule.

I hope that these results demonstrate the robustness of RayOA as a chiroptical technique that is capable of assigning the AC of chiral molecules. This is especially illustrated here due to its remarkable insensitivity to the conformational flexibility of fluoxetine, which is an effect that plagues other chiroptical techniques and can interfere with a confident assignment.

CHAPTER 9

Conclusions

During my time at Vanderbilt, I have had the pleasure of studying the chirality of several complex and flexible molecules. The majority of the work performed during my Ph.D. were computational investigations, but I was able to perform experiment OR, ECD, and VCD of octahydrocurcumin and hexahydrocurcumin which were (unfortunately) very difficult to measure due to their significant conformational flexibility. I am also grateful to have presented some of this research in Hiroshima, Japan at the 19th International Conference on Chiroptical Spectroscopy.

In the case of crypto-optically active compounds (see Chapter 2), specifically isotopically chiral compounds, vibrational chiroptical spectroscopies are the only means by which the chirality of the compound can be assigned. A significant amount of synthetic work was done to make this isotopically chiral compound, pushing the boundaries of organic chemistry, and characterization of the chirality of this compound was only possible via VCD spectroscopy. This crypto-optically active probe possess a great potential to decipher alkyl transferase enzyme reaction mechanisms, without the drawback of being radioactive.

My work on modeling a mechanically chiral [1]rotaxane (see Chapter 3) helps pave the way for the design of new mechanically chiral scaffolds. The relative orientation of the axle and macrocycle was difficult to preserve in my conformational analysis, resulting in many conformations that lacked the interlocked stereogenic unit. Additionally, DFT calculations show that the majority of the relevant ECD and VCD bands were the result of complicated vibrational modes along both the macrocycle and the axle. Combined with the limited information in the VCD spectrum, this results in a difficult AC assignment. Understanding the final mechanical chirality is essential to understand how this chirality originated, so that these reactions can be understood and new reactions can be developed. Additionally, DFT

calculations suggest that the diastereoselectivity might have arisen from the relative energy difference between the diastereomers, which may correlate with the transition state of the AT-CuAAC reaction.

I hope that this work, especially on microsolvation and dimerization, can serve as a guide for those doing chiroptical spectroscopy for AC determination of stubborn compounds. As computational resources continue to grow, I hope that these investigations can become more routine and highlight the utility of chiroptical spectroscopy in studying intermolecular interactions. Implicit solvation, while computationally inexpensive, can be unable to effectively model the solution-state behavior of chiral molecules. My bottom-up approach with *Quantum Cluster Growth* (see Chapter 6) strikes a delicate balance between exploring solute–solvent conformational space and control over the number of solvent molecules, which allows one to capture the conformational changes caused by solvent coordination. This approach has also been applied to homochiral dimers of [5]ladderanoic acid (see Chapter 7), which have demonstrated the importance of dimers for interpreting VCD spectra. However, further study is necessary in order to truly unravel the importance of modeling dimers for VROA spectroscopy.

I am also hopeful in the utility of RayOA as a chiroptical spectroscopic technique for AC determination (see Chapter 8). Despite being theoretically understood for decades, modern instrumentation has allowed RayOA to be fully realized. As I have shown with several examples in Chapter 8, RayOA is relatively insensitive to conformational flexibility and the level of theory used. This means that the sign of RayOA is easy to obtain, even with low-cost calculations and crude representations of the molecular ensemble. Additionally, it should be mentioned that the tensors required for the RayOA invariants are easy to compute. This is in contrast to VROA spectroscopy, which requires normal coordinate derivatives of the polarizability tensors, and OR which requires high-level calculations in order to obtain good agreement with experimental data. All of this makes RayOA a promising AC determination technique.

I am especially hopeful in the development of new methods for advancing VCD and VROA spectroscopy. The Raghavachari lab at IU Bloomington has developed novel fragmentation approaches that allow frequency calculations to extended to large systems.[215,216] This work represents a fundamentally rigorous approach over that of Bour and Kiederling, whose Cartesian tensor transfer (CTT) method allows the optimization of mid-frequency normal modes.[217] This has significant potential applications in VROA spectroscopy, which has become a state-of-the-art method for studying molecules in water. Applications of these novel methods have the possibility to investigate the native conformations of large proteins with chiroptical spectroscopy. Even now, impressive results have been obtained for full optimizations of α-helical peptides up to 25 residues with VCD spectroscopy.[218] This paves the way to understand the chiroptical properties of whole proteins and large glycomaterials, which are prohibitively computationally expensive.

Another area of research that has the potential to have the biggest impact on the application of chiroptical spectroscopic methods is machine learning. Locating the low-energy conformations and untangling the intermolecular interactions in solution are some of the largest barriers in the routine application of chiroptical spectroscopy. Quantum chemistry calculations, even with a small basis set, can be prohibitively expensive when the conformational ensemble is in the realms of tens of thousands of conformations. This issue is prevalent in my studies of hexa- and octahydrocurcumin (see Chapter 4) as well as Peyssonnoside A (see Chapter 5), where optimizations of the entire ensemble were not possible. Already, non-transferable approaches have been applied to understand the influence of conformation and intramolecular interactions on the simulated VCD spectrum of flexible molecules.[219]

References

1. Bolchi, C.; Roda, G.; Pallavicini, M. 1H NMR spectroscopy in the presence of Mosher acid to rapidly determine the enantiomeric composition of amino acid benzyl esters, chirons susceptible to easy racemization. *Amino Acids* **2018**, *50*, 1759–1767.

2. Brzezicki, A.; Garbacz, P. Differentiation and identification of enantiomers by nuclear magnetic resonance spectroscopy with support of quantum mechanical computations. *Chirality* **2023**,

3. Dcunha, R.; Crawford, T. D. Modeling Complex Solvent Effects on the Optical Rotation of Chiral Molecules: A Combined Molecular Dynamics and Density Functional Theory Study. *Journal of Physical Chemistry A* **2021**, *125*, 3095–3108.

4. Polavarapu, P. L.; Jeirath, N.; Kurtán, T.; Pescitelli, G.; Krohn, K. Determination of the absolute configurations at stereogenic centers in the presence of axial chirality. *Chirality* **2009**, *21*.

5. Keiderling, T. A. Instrumentation for Vibrational Circular Dichroism Spectroscopy: Method Comparison and Newer Developments. *Molecules* **2018**, *23*, 2404–2426.

6. Polavarapu, P. L. *Chiroptical Spectroscopy: Fundamentals and Applications*; Taylor & Francis, 2017.

7. Bünnemann, K.; Merten, C. Solvation of a Chiral Carboxylic Acid: Effects of Hydrogen Bonding on the IR and VCD Spectra of α-Methoxyphenylacetic Acid. *Physical Chemistry Chemical Physics* **2017**, *19*, 18948–18956.

8. Bünnemann, K.; Pollok, C. H.; Merten, C. Explicit Solvation of Carboxylic Acids for Vibrational Circular Dichroism Studies: Limiting the Computational Efforts without Losing Accuracy. *The Journal of Physical Chemistry B* **2018**, *122*, 8056–8064.

9. Weirich, L.; Merten, C. Solvation and self-aggregation of chiral alcohols: how hydrogen bonding affects their VCD spectral signatures. *Physical Chemistry Chemical Physics* **2019**, *21*, 13503.

10. Lightner, C. R.; Desmet, F.; Gisler, D.; Meyer, S. A.; Francis, A.; Mellor, P.; Niese, H.; Rosspeintner, A.; Keitel, R. C.; Bu, T.; Herrebout, W. A.; Johannessen, C.; Norris, D. J. Understanding Artifacts in Chiroptical Spectroscopy. *ACS Photonics* **2023**, *10*, 475–483.

11. Palivec, V.; Kopecký, V.; Jungwirth, P.; Bouř, P.; Kaminský, J.; Martinez-Seara, H. Simulation of Raman and Raman optical activity of saccharides in solution. *Physical Chemistry Chemical Physics* **2020**, *22*, 1983–1993.

12. Palivec, V.; Johannessen, C.; Kaminský, J.; Martinez-Seara, H. Use of Raman and Raman optical activity to extract atomistic details of saccharides in aqueous solution. *PLoS Computational Biology* **2022**, *18*.

13. Bose, P. K.; Polavarapu, P. L. Vibrational circular dichroism is a sensitive probe of the glycosidic linkage: Oligosaccharides of glucose. *Journal of the American Chemical Society* **1999**, *121*, 6094–6095.

14. Barron, L. D.; Gargaro, A. R.; Wen, Z. Q. Vibrational Raman optical activity of carbohydrates. *Carbohydrate Research* **1991**, *210*, 39–49.

15. Taniguchi, T.; Monde, K. Vibrational circular dichroism (VCD) studies on disaccharides in the CH region: Toward discrimination of the glycosidic linkage position. *Organic and Biomolecular Chemistry* **2007**, *5*, 1104–1110.

16. Kreienborg, N. M.; Merten, C. How to treat C-F stretching vibrations? A vibrational CD study on chiral fluorinated molecules. *Physical Chemistry Chemical Physics* **2019**, *21*, 3506–3511.

17. Koby, R. F.; Hanusa, T. P. Dispersion and distortion in heavy group 2 and lanthanide decamethylmetallocenes: The $(C_5Me_5)_2$(Sr,Sm) connection. *Journal of Organometallic Chemistry* **2018**, *857*, 145–151.

18. Grimme, S.; Antony, J.; Ehrlich, S.; Krieg, H. A consistent and accurate ab initio parametrization of density functional dispersion correction (DFT-D) for the 94 elements H-Pu. *Journal of Chemical Physics* **2010**, *132*.

19. Grimme, S.; Ehrlich, S.; Goerigk, L. Effect of the damping function in dispersion corrected density functional theory. *Journal of Computational Chemistry* **2011**, *32*, 1456–1465.

20. Pescitelli, G.; Bruhn, T. Good Computational Practice in the Assignment of Absolute Configurations by TDDFT Calculations of ECD Spectra. *Chirality* **2016**, *28*, 466–474.

21. Merten, C.; Li, F.; Bravo-Rodriguez, K.; Sanchez-Garcia, E.; Xu, Y.; Sander, W. Solvent-induced conformational changes in cyclic peptides: a vibrational circular dichroism study. *Physical Chemistry Chemical Physics* **2014**, *16*, 5627–5633.

22. Eikås, K. D. R.; Beerepoot, M. T. P.; Ruud, K. A Computational Protocol for Vibrational Circular Dichroism Spectra of Cyclic Oligopeptides. *Journal of Physical Chemistry A* **2022**, *2022*, 5471.

23. Scholten, K.; Merten, C. Solvation of the Boc-Val-Phe-*n*Pr peptide characterized by VCD spectroscopy and DFT calculations. *Physical Chemistry Chemical Physics* **2022**, *24*, 3611–3617.

24. Perera, A. S.; Thomas, J.; Poopari, M. R.; Xu, Y. The clusters-in-a-liquid approach for solvation: New insights from the conformer specific gas phase spectroscopy and vibrational optical activity spectroscopy. 2016.

25. Naret, T.; Lesot, P.; Puente, A. R.; Polavarapu, P. L.; Buisson, D. A.; Crassous, J.; Pieters, G.; Feuillastre, S. Chemical synthesis of [2H]-ethyl tosylate and exploration of its crypto-optically active character combining complementary spectroscopic tools. *Organic Letters* **2020**, *22*, 8846–8849.

26. Brunner, A.; Hintermann, L. Configurational Assignment of 'Cryptochiral' 10-Hydroxystearic Acid Through an Asymmetric Catalytic Synthesis. *Helvetica Chimica Acta* **2016**, *99*, 928–943.

27. Huang, H.; Chang, W. C.; Lin, G. M.; Romo, A.; Pai, P. J.; Russell, W. K.; Russell, D. H.; Liu, H. W. Mechanistic consequences of chiral radical clock probes: Analysis of the mononuclear non-heme iron enzyme HppE with 2-hydroxy-3-methylenecyclopropyl radical clock substrates. *Journal of the American Chemical Society* **2014**, *136*, 2944–2947.

28. Xu, S.; Oda, A.; Negishi, E. I. Enantioselective synthesis of chiral isotopomers of 1-alkanols by a ZACA-Cu-catalyzed cross-coupling protocol. *Chemistry - A European Journal* **2014**, *20*, 16060–16064.

29. Floss, H. G.; Lee, S. Chiral Methyl Groups: Small Is Beautiful. *Accounts of Chemical Research* **1993**, *26*, 116–122.

30. Schweifer, A.; Hammerschmidt, F. Stereochemical Course of Methyl Transfer by Cobalamin-Dependent Radical SAM Methyltransferase in Fosfomycin Biosynthesis. *Biochemistry* **2018**, *57*, 2069–2073.

31. Faucher, N.; Cintrat, J. C.; Berthault, P.; Rousseau, B. The shortest route to chiral ditosylmethylamine. *Angewandte Chemie - International Edition* **2002**, *41*, 497–498.

32. Lafon, O.; Lesot, P.; Merlet, D.; Courtieu, J. Modified z-gradient filtering as a mean to obtain phased deuterium autocorrelation 2D NMR spectra in oriented solvents. *Journal of Magnetic Resonance* **2004**, *171*, 135–142.

33. Lesot, P.; Aroulanda, C.; Zimmermann, H.; Luz, Z. Enantiotopic discrimination in the NMR spectrum of prochiral solutes in chiral liquid crystals. *2330 — Chem. Soc. Rev* **2015**, *44*, 2330.

34. Parenty, A.; Campagne, J. M.; Aroulanda, C.; Lesot, P. Routine use of natural abundance deuterium NMR in a polypeptidic chiral oriented solvent for the determination of the enantiomeric composition of chiral building blocks. *Organic Letters* **2002**, *4*, 1663–1666.

35. Sarfati, M.; Lesot, P.; Merlet, D.; Courtieu, J. Theoretical and experimental aspects of enantiomeric differentiation using natural abundance multinuclear nmr spectroscopy in chiral polypeptide liquid crystals. **2000**,

36. Streitwieser, A.; Granger, M. R. Stereochemistry of the Primary Carbon. XV. Preparation of Optically Active Ethanol-1-d by Asymmetric Induction and its Absolute Configuration. *Journal of Organic Chemistry* **1967**, *32*, 1528–1529.

37. Huber, T. D.; Johnson, B. R.; Zhang, J.; Thorson, J. S. AdoMet analog synthesis and utilization: current state of the art. 2016.

38. Stecher, H.; Tengg, M.; Ueberbacher, B. J.; Remler, P.; Schwab, H.; Griengl, H.; Gruber-Khadjawi, M. Biocatalytic Friedel-Crafts alkylation using non-natural cofactors. *Angewandte Chemie - International Edition* **2009**, *48*, 9546–9548.

39. Ahn, Y.; Krzycki, J. A.; Floss, H. G. Steric Course of the Reduction of Ethyl Coenzyme M to Ethane Catalyzed by Methyl Coenzyme M Reductase from Methanosarcina Barkeri. *Journal of the American Chemical Society* **1991**, *113*, 4700–4701.

40. Ahn, Y.; Floss, H. G.; Qizhuang, Y.; Cho, H.; Walsh, C. T. Stereochemistry of Carbon-Phosphorus Cleavage in Ethylphosphonate Catalyzed by C-P Lyase from Escherichia coli. *Journal of the American Chemical Society* **1992**, *114*, 7953–7954.

41. Priestley, N. D.; Floss, H. G.; Froland, W. A.; Lipscomb, J. D.; Williams, P. G.; Morimoto, H. Cryptic Stereospecificity of Methane Monooxygenase. *Journal of the American Chemical Society* **1992**, *114*, 7561–7562.

42. Valentine, A. M.; Wilkinson, B.; Liu, K. E.; Komar-Panicucci, S.; Priestley, N. D.; Williams, P. G.; Morimoto, H.; Floss, H. G.; Lippard, S. J. Tritiated chiral alkanes as substrates for soluble methane monooxygenase from Methylococcus capsulatus (Bath): Probes for the mechanism of hydroxylation. *Journal of the American Chemical Society* **1997**, *119*, 1818–1827.

43. Simov, B. P.; Wuggenig, F.; Mereiter, K.; Andres, H.; France, J.; Schnelli, P.; Hammerschmidt, F. Direct chemical synthesis of chiral methanol of 98its conversion to [2H1,3H]methyl tosylate and [2H1,3H-methyl]methionine. *Journal of the American Chemical Society* **2005**, *127*, 13934–13940.

44. Jacques, V.; Czarnik, A. W.; Judge, T. M.; Ploeg, L. H. V. D.; DeWitt, S. H. Differentiation of antiinflammatory and antitumorigenic properties of stabilized enantiomers of thalidomide analogs. *Proceedings of the National Academy of Sciences of the United States of America* **2015**, *112*, E1471–E1479.

45. Barabás, B.; Caglioti, L.; Micskei, K.; Zucchi, C.; Pályi, G. Isotope chirality and asymmetric autocatalysis: A possible entry to biological chirality. *Origins of Life and Evolution of Biospheres* **2008**, *38*, 317–327.

46. Fujita, T.; Obata, K.; Kuwahara, S.; Miura, N.; Nakahashi, A.; Monde, K.; Decatur, J.; Harada, N. (R)-(+)-[VCD(+)945]-4-Ethyl-4-methyloctane, the simplest chiral saturated hydrocarbon with a quaternary stereogenic center. *Tetrahedron Letters* **2007**, *48*, 4219–4222.

47. Kuwahara, S.; Obata, K.; Fujita, T.; Miura, N.; Nakahashi, A.; Monde, K.; Harada, N. (R)-(+)-[VCD(–)984]-4-Ethyl-4-methyloctane: A Cryptochiral Hydrocarbon with a

Quaternary Chiral Center. (2) Vibrational CD Spectra of Both Enantiomers and Absolute Configurational Assignment. *European Journal of Organic Chemistry* **2010**, *2010*, 6385–6392.

48. Haesler, J.; Schindelholz, I.; Riguet, E.; Bochet, C. G.; Hug, W. Absolute configuration of chirally deuterated neopentane. *Nature* **2007**, *446*, 526–529.

49. Masarwa, A.; Gerbig, D.; Oskar, L.; Loewenstein, A.; Reisenauer, H. P.; Lesot, P.; Schreiner, P. R.; Marek, I. Synthese und stereochemische Bestimmung von kryptooptisch-aktivem 2 H 6 -Neopentan. *Angewandte Chemie* **2015**, *127*, 13298–13302.

50. Miura, T.; Nakamuro, T.; Stewart, S. G.; Nagata, Y.; Murakami, M. Synthesis of Enantiopure C3-Symmetric Triangular Molecules. *Angewandte Chemie - International Edition* **2017**, *56*, 3334–3338.

51. Miura, T.; Nakamuro, T.; Nagata, Y.; Moriyama, D.; Stewart, S. G.; Murakami, M. Asymmetric Synthesis and Stereochemical Assignment of 12C/13C Isotopomers. *Journal of the American Chemical Society* **2019**, *141*, 13341–13345.

52. Barron, L. D. *Molecular Light Scattering and Optical Activity*; Cambridge University Press, 2004.

53. He, Y.; Wang, B.; Dukor, R. K.; Nafie, L. A. Determination of absolute configuration of chiral molecules using vibrational optical activity: A review. *Applied Spectroscopy* **2011**, *65*, 699–723.

54. Merten, C.; Golub, T. P.; Kreienborg, N. M. Absolute Configurations of Synthetic Molecular Scaffolds from Vibrational CD Spectroscopy. *Journal of Organic Chemistry* **2019**, *84*, 8797–8814.

55. Nafie, L. A. *Vibrational Optical Activity: Principles and Applications*; John Wiley and Sons Inc., 2011.

56. Saito, F.; Schreiner, P. R. Determination of the Absolute Configurations of Chiral Alkanes – An Analysis of the Available Tools. *European Journal of Organic Chemistry* **2020**, *2020*, 6328–6339.

57. Stephens, P. J.; Devlin, F. J.; Pan, J. J. The determination of the absolute configurations of chiral molecules using vibrational circular dichroism (VCD) spectroscopy. *Chirality* **2008**, *20*, 643–663.

58. Levy, H. R.; Loewus, F. A.; Vennesland, B. The Optical Rotation and Configuration of a Pure Enantiomorph of Ethanol-1-d. *Journal of the American Chemical Society* **1957**, *79*, 2949–2953.

59. Lemieux, R. U.; LastNameHoivard, J. The Absolute Configuration of dextro-I-deuterioethanol. *Can. J. Chem. Downloaded from cdnsciencepub.com by Vanderbuilt University Library on* **1963**, *41*.

60. Shaw, R. A.; Wieser, H.; Duller, R.; Rauk, A. Vibrational Optical Activity of (S)-I-d-Ethanol. *Journal of the American Chemical Society* **1990**, *112*, 5401–5410.

61. Lesot, P.; Aroulanda, C.; Berdagué, P.; Meddour, A.; Merlet, D.; Farjon, J.; Giraud, N.; Lafon, O. Multinuclear NMR in polypeptide liquid crystals: Three fertile decades of methodological developments and analytical challenges. 2020.

62. Puente, A. R.; Bessaguet, A.; Pairault, N.; Pieters, G.; Crassous, J.; Polavarapu, P. L.; Opalinski, I.; Papot, S. Absolute configuration of a [1]rotaxane determined from vibrational and electronic circular dichroism spectra. *Chirality* **2021**, *33*, 773–782.

63. Bruns, C. J.; Stoddart, J. F. *The Nature of the Mechanical Bond: From Molecules to Machines*, 1st ed.; Wiley, 2016; pp 1–761.

64. Waelès, P.; Gauthier, M.; Coutrot, F. Challenges and Opportunities in the Post-Synthetic Modification of Interlocked Molecules. *Angewandte Chemie - International Edition* **2021**, *60*, 16778–16799.

65. Denis, M.; Goldup, S. M. The active template approach to interlocked molecules. *Nature Reviews Chemistry* **2017**, *1*.

66. Fielden, S. D.; Leigh, D. A.; Woltering, S. L. Molecular Knots. *Angewandte Chemie - International Edition* **2017**, *56*, 11166–11194.

67. Lewis, J. E.; Beer, P. D.; Loeb, S. J.; Goldup, S. M. Metal ions in the synthesis of interlocked molecules and materials. *Chemical Society Reviews* **2017**, *46*, 2577–2591.

68. Gil-Ramírez, G.; Leigh, D. A.; Stephens, A. J. Catenanes: Fifty years of molecular links. *Angewandte Chemie - International Edition* **2015**, *54*, 6110–6150.

69. Beves, J. E.; Blight, B. A.; Campbell, C. J.; Leigh, D. A.; McBurney, R. T. Strategies and tactics for the metal-directed synthesis of rotaxanes, knots, catenanes, and higher order links. *Angewandte Chemie - International Edition* **2011**, *50*, 9260–9327.

70. Crowley, J. D.; Goldup, S. M.; Lee, A. L.; Leigh, D. A.; Burney, R. T. M. Active metal template synthesis of rotaxanes, catenanes and molecular shuttles. *Chemical Society Reviews* **2009**, *38*, 1530–1541.

71. Maynard, J. R.; Goldup, S. M. Strategies for the Synthesis of Enantiopure Mechanically Chiral Molecules. *Chem* **2020**, *6*, 1914–1932.

72. Jamieson, E. M.; Modicom, F.; Goldup, S. M. Chirality in rotaxanes and catenanes. *Chemical Society Reviews* **2018**, *47*, 5266–5311.

73. Bordoli, R. J.; Goldup, S. M. An efficient approach to mechanically planar chiral rotaxanes. *Journal of the American Chemical Society* **2014**, *136*, 4817–4820.

74. Aucagne, V.; Berná, J.; Crowley, J. D.; Goldup, S. M.; Hänni, K. D.; Leigh, D. A.; Lusby, P. J.; Ronaldson, V. E.; Slawin, A. M.; Viterisi, A.; Walker, D. B. Catalytic "active-metal" template synthesis of [2]rotaxanes, [3]rotaxanes, and molecular shuttles, and some observations on the mechanism of the Cu(I)-catalyzed azide-alkyne 1,3-cycloaddition. *Journal of the American Chemical Society* **2007**, *129*, 11950–11963.

75. Aucagne, V.; Hänni, K. D.; Leigh, D. A.; Lusby, P. J.; Walker, D. B. Catalytic "click" rotaxanes: A substoichiometric metal-template pathway to mechanically interlocked architectures. *Journal of the American Chemical Society* **2006**, *128*, 2186–2187.

76. Jinks, M. A.; de Juan, A.; Denis, M.; Fletcher, C. J.; Galli, M.; Jamieson, E. M. G.; Modicom, F.; Zhang, Z.; Goldup, S. M. Stereoselective Synthesis of Mechanically Planar Chiral Rotaxanes. *Angewandte Chemie* **2018**, *130*, 15022–15026.

77. Tian, C.; Fielden, S. D.; Pérez-Saavedra, B.; Vitorica-Yrezabal, I. J.; Leigh, D. A. Single-Step Enantioselective Synthesis of Mechanically Planar Chiral [2]Rotaxanes Using a Chiral Leaving Group Strategy. *Journal of the American Chemical Society* **2020**, *142*, 9803–9808.

78. Koenis, M. A.; Chibueze, C. S.; Jinks, M. A.; Nicu, V. P.; Visscher, L.; Goldup, S. M.; Buma, W. J. Vibrational circular dichroism spectroscopy for probing the expression of chirality in mechanically planar chiral rotaxanes. *Chemical Science* **2020**, *11*, 8469–8475.

79. Pairault, N.; Bessaguet, A.; Barat, R.; Frédéric, L.; Pieters, G.; Crassous, J.; Opalinski, I.; Papot, S. Diastereoselective synthesis of [1]rotaxanes via an active metal template strategy. *Chemical Science* **2021**, *12*, 2521–2526.

80. CONFLEX High Performance Conformation Analysis. 2000.

81. Gaus, M.; Goez, A.; Elstner, M. Parametrization and benchmark of DFTB3 for organic molecules. *Journal of Chemical Theory and Computation* **2013**, *9*, 338–354.

82. Hehre, W. J.; Ditchfield, K.; Pople, J. A. Self-consistent molecular orbital methods. XII. Further extensions of gaussian-type basis sets for use in molecular orbital studies of organic molecules. *The Journal of Chemical Physics* **1972**, *56*, 2257–2261.

83. Frisch, M. J. et al. Gaussian 16 Rev. C.01. 2016.

84. Covington, C. L.; Polavarapu, P. L. CDSpecTech: A single software suite for multiple chiroptical spectroscopic analyses. *Chirality* **2017**, *29*, 178–192.

85. Debie, E.; Gussem, E. D.; Dukor, R. K.; Herrebout, W.; Nafie, L. A.; Bultinck, P. A confidence level algorithm for the determination of absolute configuration using vibrational circular dichroism or raman optical activity. *ChemPhysChem* **2011**, *12*, 1542–1549.

86. Becke, A. D. Density-functional thermochemistry. III. The role of exact exchange. *The Journal of Chemical Physics* **1993**, *98*, 5648–5652.

87. Schäfer, A.; Huber, C.; Ahlrichs, R. Fully optimized contracted Gaussian basis sets of triple zeta valence quality for atoms Li to Kr. *The Journal of Chemical Physics* **1994**, *100*, 5829–5835.

88. Martin, R. L. Natural transition orbitals. *Journal of Chemical Physics* **2003**, *118*, 4775–4777.

89. Peach, M. J.; Benfield, P.; Helgaker, T.; Tozer, D. J. Excitation energies in density functional theory: An evaluation and a diagnostic test. *Journal of Chemical Physics* **2008**, *128*, 4775.

90. Raeber, A. E.; Wong, B. M. The importance of short- and long-range exchange on various excited state properties of DNA monomers, stacked complexes, and Watson-Crick pairs. 2015; http://www.bmwong-group.com.

91. Mahato, B.; Panda, A. N. Assessing the Performance of DFT Functionals for Excited-State Properties of Pyridine-Thiophene Oligomers. *Journal of Physical Chemistry A* **2021**, *125*, 115–125.

92. Yanai, T.; Tew, D. P.; Handy, N. C. A new hybrid exchange-correlation functional using the Coulomb-attenuating method (CAM-B3LYP). *Chemical Physics Letters* **2004**, *393*, 51–57.

93. Puente, A. R.; Nagabhushanam, K.; Ganjihal, S.; Muhammed, M.; Polavarapu, P. L. Chiroptical spectroscopic studies for the absolute configuration determination of hexahydrocurcumin and octahydrocurcumin. *Chirality* **2022**, *34*, 1515–1525.

94. Ahsan, A. R.; Arshad, M.; Khushtar, M.; Ahmad, M. A.; Muazzam, M.; Akhter, M. S.; Gupta, G.; Muzahid, M.; Khushtar, C. M. A Comprehensive Review on Physiological Effects of Curcumin. *Drug Res (Stuttg)* **2020**, *70*, 441–447.

95. Kotha, R. R.; Luthria, D. L. Curcumin: Biological, pharmaceutical, nutraceutical, and analytical aspects. *Molecules* **2019**, *24*.

96. Prasad, S.; Dubourdieu, D.; Srivastava, A.; Kumar, P.; Lall, R. Metal–curcumin complexes in therapeutics: An approach to enhance pharmacological effects of curcumin. *International Journal of Molecular Sciences* **2021**, *22*.

97. Huang, Y.; Cao, S.; Zhang, Q.; Zhang, H.; Fan, Y.; Qiu, F.; Kang, N. Biological and pharmacological effects of hexahydrocurcumin, a metabolite of curcumin. *Archives of Biochemistry and Biophysics* **2018**, *646*, 31–37.

98. Zhao, F.; Gong, Y.; Hu, Y.; Lu, M.; Wang, J.; Dong, J.; Chen, D.; Chen, L.; Fu, F.; Qiu, F. Curcumin and its major metabolites inhibit the inflammatory response induced by lipopolysaccharide: Translocation of nuclear factor-κB as potential target. *Molecular Medicine Reports* **2015**, *11*, 3087–3093.

99. Ireson, C. R.; Jones, D. J.; Boocock, D. J.; Farmer, P. B.; Gescher, A. J.; Orr, S.; Coughtrie, M. W.; Williams, M. L.; Steward, W. P. Metabolism of the cancer chemopreventive agent curcumin in human and rat intestine. *Cancer Epidemiology Biomarkers and Prevention* **2002**, *11*, 105–111.

100. Zhang, P.; Xue, S.; Tang, P.; Cui, Z.; Wang, Z.; Luo, J.; Kong, L. Aphamines A-C, dimeric acyclic diterpene enantiomers from Aphanamixis polystachya. *Chinese Chemical Letters* **2021**, *32*, 1480–1484.

101. Giordano, A.; Tommonaro, G. Curcumin and cancer. *Nutrients* **2019**, *11*.

102. Sharifi, S.; Vahed, S. Z.; Ahmadian, E.; Dizaj, S. M.; Abedi, A.; Khatibi, S. M. H.; Samiei, M. Stem Cell Therapy: Curcumin Does the Trick. *Phytotherapy Research* **2019**, *33*, 2927–2937.

103. Shen, L.; Liu, C. C.; An, C. Y.; Ji, H. F. How does curcumin work with poor bioavailability? Clues from experimental and theoretical studies. *Scientific Reports* **2016**, *6*.

104. Pandey, A.; Chaturvedi, M.; Mishra, S.; Kumar, P.; Somvanshi, P.; Chaturvedi, R. Reductive metabolites of curcumin and their therapeutic effects. *Heliyon* **2020**, *6*.

105. Niwa, T.; Yokoyama, S. I.; Mochizuki, M.; Osawa, T. Production of optically active hexahydrocurcumin by human intestinal bacterium in vitro. *Biological and Pharmaceutical Bulletin* **2021**, *44*, 136–139.

106. Niwa, T.; Yokoyama, S. I.; Mochizuki, M.; Osawa, T. In Vitro Production of Optically Active Octahydrocurcumin by Human Intestinal Bacterium. *Biological and Pharmaceutical Bulletin* **2022**, *45*, 378–381.

107. Rowland, I.; Gibson, G.; Heinken, A.; Scott, K.; Swann, J.; Thiele, I.; Tuohy, K. Gut microbiota functions: metabolism of nutrients and other food components. *European Journal of Nutrition* **2018**, *57*, 1–24.

108. Scazzocchio, B.; Minghetti, L.; D'archivio, M. Interaction between gut microbiota and curcumin: A new key of understanding for the health effects of curcumin. *Nutrients* **2020**, *12*, 1–18.

109. Anand, P.; Kunnumakkara, A. B.; Newman, R. A.; Aggarwal, B. B. Bioavailability of curcumin: Problems and promises. *Molecular Pharmaceutics* **2007**, *4*, 807–818.

110. Zhang, Z.; Luo, D.; Xie, J.; Lin, G.; Zhou, J.; Liu, W.; Li, H.; Yi, T.; Su, Z.; Chen, J. Octahydrocurcumin, a final hydrogenated metabolite of curcumin, possesses superior anti-tumor activity through induction of cellular apoptosis. *Food and Function* **2018**, *9*, 2005–2014.

111. Luo, D. D.; Chen, J. F.; Liu, J. J.; Xie, J. H.; Zhang, Z. B.; Gu, J. Y.; Zhuo, J. Y.; Huang, S.; Su, Z. R.; Sun, Z. H. Tetrahydrocurcumin and octahydrocurcumin, the primary and final hydrogenated metabolites of curcumin, possess superior hepatic-protective effect against acetaminophen-induced liver injury: Role of CYP2E1 and Keap1-Nrf2 pathway. *Food and Chemical Toxicology* **2019**, *123*, 349–362.

112. Kikuzaki, H.; Usuguchi, J.; Nakatani, N. Constituents of Zingiberaceae: I: Diarylheptanoids from the Rhizomes of Ginger (Zingiber officinale roscoe). *Chemical and Pharmaceutical Bulletin* **1991**, *39*, 120–122.

113. Itokawa, H.; Morita, H.; Midorikawa, I.; Aiyama, R.; Morita, M. Diarylheptanoids from the Rhizome of Alpinia officinarum Hance. *Chemical and Pharmaceutical Bulletin* **1985**, *33*, 4889–4893.

114. Uehara, S. I.; Yasuda, I.; Akiyama, K.; Morita, H.; Takeya, K.; Itokawa, H. Diarylheptanoids from the Rhizomes of Curcuma Xanthorrhiza and Alpinia Officinarum. *Chemical and Pharmaceutical Bulletin* **1987**, *35*, 3298–3304.

115. Murata, T.; Shinohara, M.; Miyamoto, M. Isolation of Hexahydrocurcumin, Dihydrogingerol and Two Additional Pungent Principles from Ginger. *Chemical and Pharmaceutical Bulletin* **1972**, *20*, 2291–2292.

116. Harada, N. The Exciton Chirality Method and its Application to Configurational and Conformational Studies of Natural Products. *Accounts of Chemical Research* **1972**, *5*, 257–263.

117. Covington, C. L.; Nicu, V. P.; Polavarapu, P. L. Determination of the Absolute Configurations Using Exciton Chirality Method for Vibrational Circular Dichroism: Right Answers for the Wrong Reasons? *Journal of Physical Chemistry A* **2015**, *119*, 10589–10601.

118. Yokosuka, A.; Mimaki, Y.; Sakagami, H.; Sashida, Y. New diarylheptanoids and diarylheptanoid glucosides from the rhizomes of Tacca chantrieri and their cytotoxic activity. *Journal of Natural Products* **2002**, *65*, 283–289.

119. Somparn, P.; Phisalaphong, C.; Nakornchai, S.; Unchern, S.; Morales, N. P. Comparative antioxidant activities of curcumin and its demethoxy and hydrogenated derivatives. *Biological and Pharmaceutical Bulletin* **2007**, *30*, 74–78.

120. Dolomanov, O. V.; Bourhis, L. J.; Gildea, R. J.; Howard, J. A.; Puschmann, H. OLEX2: A complete structure solution, refinement and analysis program. *Journal of Applied Crystallography* **2009**, *42*, 339–341.

121. Sheldrick, G. M. SHELXT - Integrated space-group and crystal-structure determination. *Acta Crystallographica Section A: Foundations of Crystallography* **2015**, *71*, 3–8.

122. Sheldrick, G. M. Crystal structure refinement with SHELXL. *Acta Crystallographica Section C: Structural Chemistry* **2015**, *71*, 3–8.

123. Frisch, M. J.; Pople, J. A.; Binkley, J. S. Self-consistent molecular orbital methods 25. Supplementary functions for Gaussian basis sets. *Journal of Chemical Physics* **1984**, *80*, 3265.

124. Lee, C.; Yang, W.; Parr, R. G. Development of the Colle-Salvetti correlation-energy formula into a functional of the electron density. *Physical Review B* **1988**, *37*, 785–789.

125. Hariharan, P. C.; Pople, J. A. Accuracy of AHn equilibrium geometries by single determinant molecular orbital theory. *Molecular Physics* **1974**, *27*, 209–214.

126. Mclean, A. D.; Chandler, G. S. Contracted Gaussian basis sets for molecular calculations. I. Second row atoms, Z=11–18. *Journal of Chemical Physics* **1980**, *72*, 5639.

127. Krishnan, R.; Binkley, J. S.; Seeger, R.; Pople, J. A. Self-consistent molecular orbital methods. XX. A basis set for correlated wave functions. *The Journal of Chemical Physics* **1980**, *72*, 650–654.

128. Tomasi, J.; Mennucci, B.; Cammi, R. Quantum mechanical continuum solvation models. 2005.

129. Scalmani, G.; Frisch, M. J. Continuous surface charge polarizable continuum models of solvation. I. General formalism. *The Journal of Chemical Physics* **2010**, *132*, 6158.

130. Chai, J. D.; Head-Gordon, M. Long-range corrected hybrid density functionals with damped atom-atom dispersion corrections. *Physical Chemistry Chemical Physics* **2008**, *10*, 6615–6620.

131. Weigend, F.; Ahlrichs, R. Balanced basis sets of split valence, triple zeta valence and quadruple zeta valence quality for H to Rn: Design and assessment of accuracy. *Physical Chemistry Chemical Physics* **2005**, *7*, 3297–3305.

132. Polavarapu, P. L.; Santoro, E.; Covington, C. L.; Johnson, J. L.; Puente, A. R.; Schley, N. D.; Kallingathodi, Z.; Prakasan, P. C.; Haleema, S.; Thomas, A. A.; Ibnusaud, I. How important are the intermolecular hydrogen bonding interactions in methanol solvent for interpreting the chiroptical properties? *Spectrochimica Acta - Part A: Molecular and Biomolecular Spectroscopy* **2021**, *247*, 119094.

133. Johnson, J. L.; Polavarapu, P. L. Chiral Molecular Structure Determination for a Desired Compound Just from Its Molecular Formula and Vibrational Optical Activity Spectra. *Journal of Physical Chemistry A* **2021**, *125*, 8013.

134. Santoro, E.; Mazzeo, G.; Petrovic, A. G.; Cimmino, A.; Koshoubu, J.; Evidente, A.; Berova, N.; Superchi, S. Absolute configurations of phytotoxins seiricardine a and inuloxin a obtained by chiroptical studies. *Phytochemistry* **2015**, *116*, 359–366.

135. Evidente, M.; Santoro, E.; Petrovic, A. G.; Cimmino, A.; Koshoubu, J.; Evidente, A.; Berova, N.; Superchi, S. Absolute configurations of phytotoxic inuloxins B and C based on experimental and computational analysis of chiroptical properties. *Phytochemistry* **2016**, *130*, 328–334.

136. Johnson, J. L.; Santoro, E.; Zatout, R.; Petrovic, A. G.; Cimmino, A.; Superchi, S.; Evidente, A.; Berova, N. D.; Polavarapu, P. L. Absolute configuration of seco-eudesmanolide inuloxin D from experimental and predicted chiroptical studies of its 4-O-acetyl derivative. *Chirality* **2021**, *33*, 233–241.

137. Hooft, R. W.; Straver, L. H.; Spek, A. L. Determination of absolute structure using Bayesian statistics on Bijvoet differences. *Journal of Applied Crystallography* **2008**, *41*, 96–103.

138. Puente, A. R.; Chhetri, B. K.; Kubanek, J.; Polavarapu, P. L. Revisiting the Absolute Configuration of Peyssonnoside A Using Vibrational Circular Dichroism Spectroscopy. *Symmetry* **2024**, *16*, 133.

139. Chhetri, B. K.; Lavoie, S.; Sweeney-Jones, A. M.; Mojib, N.; Raghavan, V.; Gagaring, K.; Dale, B.; McNamara, C. W.; Soapi, K.; Quave, C. L.; Polavarapu, P. L.; Kubanek, J. Peyssonnosides A–B, Unusual Diterpene Glycosides with a Sterically Encumbered Cyclopropane Motif: Structure Elucidation Using an Integrated Spectroscopic and Computational Workflow. *Journal of Organic Chemistry* **2019**, *84*, 8431–8541.

140. Chini, M. G.; Jones, C. R.; Zampella, A.; D'Auria, M. V.; Renga, B.; Fiorucci, S.; Butts, C. P.; Bifulco, G. Quantitative NMR-derived interproton distances combined with quantum mechanical calculations of 13C chemical shifts in the stereochemical determination of conicasterol F, a nuclear receptor ligand from Theonella swinhoei. *Journal of Organic Chemistry* **2012**, *77*, 1489–1496.

141. Laskowski, T.; Szwarc, K.; Szczeblewski, P.; Sowiński, P.; Borowski, E.; Pawlak, J. Monosaccharides as Potential Chiral Probes for the Determination of the Absolute Configuration of Secondary Alcohols. *Journal of Natural Products* **2016**, *79*, 2797–2804.

142. Grimblat, N.; Zanardi, M. M.; Sarotti, A. M. Beyond DP4: An Improved Probability for the Stereochemical Assignment of Isomeric Compounds using Quantum Chemical Calculations of NMR Shifts. *Journal of Organic Chemistry* **2015**, *80*, 12526–12534.

143. Chesnokov, G. A.; Gademann, K. Concise Total Synthesis of Peyssonnoside A. *Journal of the American Chemical Society* **2021**, *143*, 14083–14088.

144. Xu, B.; Liu, C.; Dai, M. Catalysis-Enabled 13-Step Total Synthesis of (–)-Peyssonnoside A. *Journal of the American Chemical Society* **2022**, *144*, 19700–19703.

145. Batista, A. N. L.; Angrisani, B. R.; Lima, M. E. D.; da Silva, S. M.; Schettini, V. H.; Chagas, H. A.; dos Santos, F. M.; Batista, J. M.; Valverde, A. L. Absolute configuration reassignment of natural products: An overview of the last decade. 2021.

146. Batista, A. N. L.; Santos, C. H. T.; de Albuquerque, A. C. F.; Jr., F. M. S.; Garcez, F. R.; Jr., J. M. B. Absolute configuration reassignment of nectamazin A: implications to related neolignans. *Spectrochimica Acta Part A: Molecular and Biomolecular Spectroscopy* **2023**, 123283.

147. Barrera, E. D. C.; Suarez, L. E. C. Three New 7.3,8.5-Connected Bicyclo[3.2.1]octanoids and Other Neolignans from Leaves of Nectandra amazonum NEES. (Lauraceae). *Chem. Pharm. Bull.* **2009**, *57*, 639–642.

148. Scholten, K.; Engelage, E.; Merten, C. Basis set dependence of S=O stretching frequencies and its consequences for IR and VCD spectra predictions. *Physical Chemistry Chemical Physics* **2020**, *22*, 27979.

149. Perdew, J. P.; Wang, Y. Accurate and simple analytic representation of the electron-gas correlation energy. *Physical Review B* **1992**, *45*, 13244–13249.

150. Gilbert, K. E. Pcmodel 10.0. 2013.

151. Hariharan, P. C.; Pople, J. A. The influence of polarization functions on molecular orbital hydrogenation energies. *Theoretica Chimica Acta* **1973**, *28*, 213–222.

152. Covington, C. L.; Polavarapu, P. L. Similarity in dissymmetry factor spectra: A quantitative measure of comparison between experimental and predicted vibrational circular dichroism. *Journal of Physical Chemistry A* **2013**, *117*, 3377–3386.

153. Legault, C. Y. CYLview20. 2020; www.cylview.org.

154. Eikås, K. D. R.; Krupová, M.; Kristoffersen, T.; Beerepoot, M. T. P.; Ruud, K. Can the absolute configuration of cyclic peptides be determined with vibrational circular dichroism? *Physical Chemistry Chemical Physics* **2023**, *25*, 14520.

155. Vermeyen, T.; Merten, C. Solvation and the secondary structure of a proline-containing dipeptide: insights from VCD spectroscopy. *Physical Chemistry Chemical Physics* **2020**, *22*, 15640–15648.

156. Stewart, J. J. Optimization of parameters for semiempirical methods V: Modification of NDDO approximations and application to 70 elements. *Journal of Molecular Modeling* **2007**, *13*, 1173–1213.

157. Puente, A. R.; Polavarapu, P. L. Influence of microsolvation on vibrational circular dichroism spectra in dimethyl sulfoxide solvent: A Bottom-Up approach using Quantum cluster growth. *Spectrochimica Acta - Part A: Molecular and Biomolecular Spectroscopy* **2023**, *303*.

158. Polavarapu, P. L.; Johnson, J. L.; Raghavan, V.; Zajac, G.; Baranska, M. Vibrational Raman optical activity of diacetyl L-tartaric acid and corresponding surfactants: Sodium salts and shorter analogs of surfactants simplify the interpretations. *J. Raman Spectrosc.* **2022**, *53*, 1102–1114.

159. Grassin, C.; Santoro, E.; Merten, C. 7-Azaindole breaks carboxylic acid dimers and simplifies VCD spectra analyses of natural products. *Chemical Communications* **2022**, *58*, 11527.

160. Klamt, A.; Schuurmann, G. COSMO: A New Approach to Dielectric Screening in Solvents with Explicit Expressions for the Screening Energy and its Gradient. *J. Chem. Soc. Perkin Trans.* **1993**, *2*, 799–805.

161. Marenich, A. V.; Cramer, C. J.; Truhlar, D. G. Universal Solvation Model Based on Solute Electron Density and on a Continuum Model of the Solvent Defined by the Bulk Dielectric Constant and Atomic Surface Tensions. *Journal of Physical Chemistry B* **2009**, *113*, 6378–6396.

162. Steiner, M.; Holzknecht, T.; Schauperl, M.; Podewitz, M. Quantum chemical microsolvation by automated water placement. *Molecules* **2021**, *26*, 1793.

163. Weirich, L.; Oliveira, J. M. D.; Merten, C. How many solvent molecules are required to solvate chiral 1,2-diols with hydrogen bonding solvents? A VCD spectroscopic study. *Physical Chemistry Chemical Physics* **2020**, *22*, 1525–1533.

164. Scherrer, A.; Vuilleumier, R.; Sebastiani, D. Vibrational circular dichroism from ab initio molecular dynamics and nuclear velocity perturbation theory in the liquid phase. *The Journal of Chemical Physics* **2016**, *145*, 84101.

165. Brehm, M.; Thomas, M. Computing Bulk Phase Raman Optical Activity Spectra from ab initio Molecular Dynamics Simulations. *Journal of Physical Chemistry Letters* **2017**, *8*, 3409–3414.

166. Vreven, T.; Byun, K. S.; Komáromi, I.; Dapprich, S.; Montgomery, J. A.; Morokuma, K.; Frisch, M. J. Combining quantum mechanics methods with molecular mechanics methods in ONIOM. *Journal of Chemical Theory and Computation* **2006**, *2*, 815–826.

167. Giovannini, T.; Cappelli, C. Continuum vs. atomistic approaches to computational spectroscopy of solvated systems. *Chemical Communications* **2023**, *59*, 5644–5660.

168. Luber, S.; Reiher, M. Calculated Raman Optical Activity Spectra of 1,6-Anhydro-D-glucopyranose. *Journal of Physical Chemistry A* **2009**, *113*, 8268–8277.

169. Barbu-Debus, K. L.; Scherrer, A.; Bouchet, A.; Sebastiani, D.; Vuilleumier, R.; Zehnacker, A. Effect of puckering motion and hydrogen bond formation on the vibrational circular dichroism spectrum of a flexible molecule: the case of (S)-1-indanol. *Physical Chemistry Chemical Physics* **2018**, *20*, 14635.

170. Ghidinelli, S.; Abbate, S.; Koshoubu, J.; Araki, Y.; Wada, T.; Longhi, G. Solvent Effects and Aggregation Phenomena Studied by Vibrational Optical Activity and Molecular Dynamics: The Case of Pantolactone. *Journal Physical Chemistry B* **2020**, *2020*, 4526.

171. Zhang, P.; Polavarapu, P. L. Spectroscopic Investigation of the Structures of Dialkyl Tartrates and Their Cyclodextrin Complexes. *Journal of Physical Chemistry A* **2007**, *111*, 858–871.

172. Heshmat, M.; Baerends, E. J.; Polavarapu, P. L.; Nicu, V. P. The Importance of Large-Amplitude Motions for the Interpretation of Mid-Infrared Vibrational Absorption and Circular Dichroism Spectra: 6,6'-Dibromo-[1,1'-binaphthalene]-2,2'-diol in Dimethyl Sulfoxide. *Journal of Physical Chemistry A* **2014**, *118*, 4766–4777.

173. Johnson, J. L.; Polavarapu, P. L. Chiral Molecular Structures of Substituted Indans: Ring Puckering, Rotatable Substituents, and Vibrational Circular Dichroism. *ACS Omega* **2019**, *4*, 4963–4976.

174. Xia, Y.; Koenis, M. A.; Collados, J. F.; Ortiz, P.; Harutyunyan, S. R.; Visscher, L.; Buma, W. J.; Nicu, V. P. Regional Susceptibility in VCD Spectra to Dynamic Molecular Motions: The Case of a Benzyl α-Hydroxysilane. *ChemPhysChem* **2018**, *19*, 561–565.

175. Spicher, S.; Plett, C.; Pracht, P.; Hansen, A.; Grimme, S. Automated Molecular Cluster Growing for Explicit Solvation by Efficient Force Field and Tight Binding Methods. *Journal of Chemical Theory and Computation* **2022**, *18*, 3174–3189.

176. Pracht, P.; Bohle, F.; Grimme, S. Automated exploration of the low-energy chemical space with fast quantum chemical methods. *Physical Chemistry Chemical Physics* **2020**, *22*, 7169–7192.

177. Bannwarth, C.; Caldeweyher, E.; Ehlert, S.; Hansen, A.; Pracht, P.; Seibert, J.; Spicher, S.; Grimme, S. Extended tight-binding quantum chemistry methods. 2021.

178. Yang, Y.; Krin, A.; Cai, X.; Poopari, M. R.; Zhang, Y.; Cheeseman, J. R.; Xu, Y. Conformations of Steroid Hormones: Infrared and Vibrational Circular Dichroism Spectroscopy. *Molecules* **2023**, *28*, 771.

179. Perera, A. S.; Carlson, C. D.; Cheramy, J.; Xu, Y. Infrared and vibrational circular dichroism spectra of methyl β-D-glucopyranose in water: The application of the quantum cluster growth and clusters-in-a-liquid solvation models. *Chirality* **2023**,

180. Grimme, S. Exploration of Chemical Compound, Conformer, and Reaction Space with Meta-Dynamics Simulations Based on Tight-Binding Quantum Chemical Calculations. *Journal of Chemical Theory and Computation* **2019**, *15*, 2847–2862.

181. Zhang, S. J.; Wang, Q.; Cheng, M.; Qian, X. H.; Yang, Y.; Jiang, J. L.; Wang, L. Y. A switchable bistable [2]rotaxane based on phosphine oxide functional group. *Chinese Chemical Letters* **2015**, *26*, 885–888.

182. Hruska, E.; Gale, A.; Huang, X. AutoSolvate: A toolkit for automating quantum chemistry design and discovery of solvated molecules. *Journal of Chemical Physics* **2022**, *156*, 124801.

183. Perera, A. S.; Cheramy, J.; Merten, C.; Thomas, J.; Xu, Y. IR, Raman, and Vibrational Optical Activity Spectra of Methyl Glycidate in Chloroform and Water: The Clusters-in-a-liquid Solvation Model. *ChemPhysChem* **2018**, *19*, 2234–2242.

184. Bannwarth, C.; Ehlert, S.; Grimme, S. GFN2-xTB: An Accurate and Broadly Parametrized Self-Consistent Tight-Binding Quantum Chemical Method with Multipole Electrostatics and Density-Dependent Dispersion Contributions. *Journal of Chemical Theory and Computation* **2019**, *15*, 1652–1671.

185. Ehlert, S.; Stahn, M.; Spicher, S.; Grimme, S. Robust and Efficient Implicit Solvation Model for Fast Semiempirical Methods. *Cite This: Journal of Chemical Theory and Computation* **2021**, *17*, 4261.

186. Rohatgi, A. WebPlotDigitizer. 2022.

187. Katsyuba, S. A.; Spicher, S.; Gerasimova, T. P.; Grimme, S. Revisiting conformations of methyl lactate in water and methanol. *Chinese Journal of Chemical Physics* **2021**, *155*, 24507.

188. Desiraju, G. R.; Steiner, T. *The weak hydrogen bond: in structural chemistry and biology*; Oxford University Press, 1999; pp 12–13.

189. Polavarapu, P. L.; Ewig, C. S.; Chandramouly, T. Conformations of Tartaric Acid and Its Esters. *J. Am. Chem. Soc* **1987**, *109*, 7382–7386.

190. Abbate, S.; Castiglione, F.; Lebon, F.; Longhi, G.; Longo, A.; Mele, A.; Panzeri, W.; Ruggirello, A.; Liveri, V. T. Spectroscopic and Structural Investigation of the Confinement of D and L Dimethyl Tartrate in Lecithin Reverse Micelles. *Journal of Physical Chemistry B* **2009**, *113*, 3024–3033.

191. Raghavan, V.; Johnson, J. L.; Stec, D. F.; Song, B.; Zajac, G.; Baranska, M.; Harris, C. M.; Schley, N. D.; Polavarapu, P. L.; Harris, T. M. Absolute Configurations of Naturally Occurring [5]-and [3]-Ladderanoic Acids: Isolation, Chiroptical Spectroscopy, and Crystallography. *J. Nat. Prod* **2018**, *81*, 35.

192. He, J.; Polavarapu, P. L. Determination of intermolecular hydrogen bonded conformers of α-aryloxypropanoic acids using density functional theory predictions of vibrational absorption and vibrational circular dichroism spectra. *Journal of Chemical Theory and Computation* **2005**, *1*, 506–514.

193. Góbi, S.; Vass, E.; Magyarfalvi, G.; Tarczay, G. Effects of strong and weak hydrogen bond formation on VCD spectra: A case study of 2-chloropropionic acid. *Physical Chemistry Chemical Physics* **2011**, *13*, 13972–13984.

194. Kuppens, T.; Herrebout, W.; Veken, B. V. D.; Bultinck, P. Intermolecular association of tetrahydrofuran-2-carboxylic acid in solution: A vibrational circular dichroism study. *Journal of Physical Chemistry A* **2006**, *110*, 10191–10200.

195. Buffeteau, T.; Cavagnat, D.; Bouchet, A.; Brotin, T. Vibrational absorption and circular dichroism studies of (–)-camphanic acid. *Journal of Physical Chemistry A* **2007**, *111*, 1045–1051.

196. Losada, M.; Tran, H.; Xu, Y. Lactic acid in solution: Investigations of lactic acid self-aggregation and hydrogen bonding interactions with water and methanol using vibrational absorption and vibrational circular dichroism spectroscopies. *Journal of Chemical Physics* **2008**, *128*.

197. Ortega, P. G. R.; Gámez, M. M.; López, F. M.; González, J. J. L. Solvent Effects on the Monomer/Hydrogen-Bonded Dimer Equilibrium in Carboxylic Acids: (+)-(S)-Ketopinic Acid as a Case Study. *Chemistry - An Asian Journal* **2016**, *11*, 1798–1803.

198. Waele, D. J. D.; Luyten, S.; Sonstrom, R. E.; Bogaerts, J.; Neill, J. L.; Viereck, P.; Goossens, K.; Baeten, M.; Vervoort, N.; Herrebout, W. Absolute configuration assignment of highly fluorinated carboxylic acids via VCD and MRR spectroscopy. *Spectrochimica Acta - Part A: Molecular and Biomolecular Spectroscopy* **2024**, *306*.

199. Schlosser, D. W.; Devlin, F.; Jalkanen, K.; Stephens, P. J. Vibrational Circular Dichroism of Matrix-isolated Molecules. *Chemical Physics Letters* **1982**, *88*, 286–291.

200. Yang, Y.; Cheramy, J.; Xu, Y. Matrix Isolation-Vibrational Circular Dichroism Spectroscopic Study of Conformations and Non-Covalent Interactions of Tetrahydro-2-Furoic Acid. *ChemPhysChem* **2021**, *22*, 1336–1343.

201. Perera, A. S.; Cheramy, J.; Poopari, M. R.; Xu, Y. Aggregation of lactic acid in cold rare-gas matrices and the link to solution: A matrix isolation-vibrational circular dichroism study. *Physical Chemistry Chemical Physics* **2019**, *21*, 3574–3584.

202. Jakub Kaminsky, K.; Ka, F.; Ková, H.; Biac, N.; Tereza Hubác Ková, O. E. S.; Kubelka, J. Double Hydrogen Bonding Dimerization Propensity of Aqueous Hydroxy Acids Investigated Using Vibrational Optical Activity. *Journal of Physical Chemistry B* **2021**, *125*, 11350–11363.

203. Zuber, G.; Wipf, P.; Beratan, D. N. Exploring the optical activity tensor by anisotropic Rayleigh optical activity scattering. *ChemPhysChem* **2008**, *9*, 265–271.

204. Barron, L. D.; Buckingham, A. D. Rayleigh and Raman scattering from optically active molecules. *Molecular Physics* **1971**, *20*, 1111–1119.

205. Polavarapu, P. L. *Vibrational Spectra: Principles and Applications with Emphasis on Optical Activity*; Elsevier, 1998.

206. Cheeseman, J. R.; Frisch, M. J. Basis Set Dependence of Vibrational Raman and Raman Optical Activity Intensities. *Journal of Chemical Theory and Computation* **2011**, *7*, 3323–3334.

207. Robertson, D. W.; Krushinski, J. H.; Fuller, R. W.; Leander, J. D. Absolute Configurations and Pharmacological Activities of the Optical Isomers of Fluoxetine, a Selective Serotonin-Uptake Inhibitor. *Journal of Medicinal Chemistry* **1988**, *31*, 1412–1417.

208. Srebro, M.; Govind, N.; Jong, W. A. D.; Autschbach, J. Optical rotation calculated with time-dependent density functional theory: The OR45 Benchmark. *Journal of Physical Chemistry A* **2011**, *115*, 10930–10949.

209. Barron, L. D.; Buckingham, A. D. A Simple Two-Group Model for Rayleigh and Raman Optical Activity. *Journal of the American Chemical Society* **1974**, *96*, 4769–4773.

210. Stone, A. J. Two-group model for the rayleigh and raman circular intensity differential—formulation for general geometries. *Molecular Physics* **1977**, *33*, 293–299.

211. Polavarapu, P. L.; Nafie, L. A. The atom dipole interaction model of Raman optical activity: Reformulation and comparison to the general two-group model. *The Journal of Chemical Physics* **1979**, *70*, 5582–5588.

212. Applequist, J. An atom dipole interaction model for molecular optical properties. *Accounts of Chemical Research* **1977**, *10*, 79–85.

213. Litman, J. M.; Liu, C.; Ren, P. Atomic Polarizabilities for Interactive Dipole Induction Models. *Journal of Chemical Information and Modeling* **2022**, *62*, 79–87.

214. Mazzeo, G.; Longhi, G.; Abbate, S.; Buonerba, F.; Ruzziconi, R. Chiroptical Signatures of Planar and Central Chirality in [2]Paracyclo[2](5,8)quinolinophane Derivatives. *European Journal of Organic Chemistry* **2014**, *2014*, 7353–7363.

215. Jose, K. V.; Beckett, D.; Raghavachari, K. Vibrational Circular Dichroism Spectra for Large Molecules through Molecules-in-Molecules Fragment-Based Approach. *Journal of Chemical Theory and Computation* **2015**, *11*, 4238–4247.

216. Gupta, A. K.; Raghavachari, K. Vibrational Analysis of Constrained Molecular Systems. *Journal of Physical Chemistry A* **2024**, *128*, 28–40.

217. Bour, P.; Sopkova, J.; Bednarova, L.; Malon, P.; Keiderling, T. A. Transfer of Molecular Property Tensors in Cartesian Coordinates: A New Algorithm for Simulation of Vibrational Spectra. *Journal of Computational Chemistry* **1997**, *18*.

218. Cheeseman, J. R.; Frisch, M. J.; Keiderling, T. A. Increased accuracy of vibrational circular dichroism calculations for isotopically labeled helical peptides. *Spectrochimica Acta - Part A: Molecular and Biomolecular Spectroscopy* **2024**, *313*.

219. Vermeyen, T.; Cunha, A.; Bultinck, P.; Herrebout, W. Impact of conformation and intramolecular interactions on vibrational circular dichroism spectra identified with machine learning. *Communications Chemistry* **2023**, *6*, 148.